RADIOGRAPHIC BONE QUALITY MARKERS AND IMPLANT MIGRATION: THE SEARCH FOR PATIENT-SPECIFIC MODELS OF KNEE ARTHROPLASTY LONGEVITY

by

Jennifer O'Neill Hurry

Submitted in partial fulfillment of the requirements
for the degree of Master of Applied Science

at

Dalhousie University
Halifax, Nova Scotia
July 2012

DALHOUSIE UNIVERSITY

SCHOOL OF BIOMEDICAL ENGINEERING

The undersigned hereby certify that they have read and recommend to the Faculty of Graduate Studies for acceptance a thesis entitled "RADIOGRAPHIC BONE QUALITY MARKERS AND IMPLANT MIGRATION: THE SEARCH FOR PATIENT-SPECIFIC MODELS OF KNEE ARTHROPLASTY LONGEVITY" by Jennifer O'Neill Hurry in partial fulfillment of the requirements for the degree of Master of Applied Science.

Dated: July 31, 2012

Co-Supervisor: _____

Co-Supervisor: _____

Readers: _____

_____

_____

DALHOUSIE UNIVERSITY

DATE: July 31, 2012

AUTHOR: Jennifer O'Neill Hurry

TITLE: RADIOGRAPHIC BONE QUALITY MARKERS AND IMPLANT MIGRATION: THE SEARCH FOR PATIENT-SPECIFIC MODELS OF KNEE ARTHROPLASTY LONGEVITY

DEPARTMENT OR SCHOOL: School of Biomedical Engineering

DEGREE: M.A.Sc. CONVOCATION: October YEAR: 2012

_____

Signature of Author

Table of Contents

List of Tables

List of Figures

Abstract

The objective of this study was to examine the link between radiographic measures of bone quality and total knee implant migration as measured by radiostereometric analysis (RSA). Two uncemented total knee arthroplasty studies (n=65) with RSA and bone mineral density (BMD) exams up to two years post surgery, and one study with cemented total knees with one year RSA data (n=18) were examined. Radiograph image texture analysis was used to characterize the bone microarchitecture, and a feasibility study was conducted to determine if a given x-ray machine could be used to obtain bone mineral density at the same time as the RSA exams.

Random Forest™ ensemble classification tree statistical models classified patients into groups based on implant migration with a range of cut-points. Models based on bone texture parameters measured from the two year radiographs had a sensitivity of 87.5% and specificity of 80% when classifying patients who had more than 0.3mm maximum total point motion (MTPM) at two years using the one year exam as reference. Other cut-points were examined, with models generally having a lower specificity if the acceptable migration was smaller, and lower sensitivity if higher migrations were tolerable. In a predictive model, post-operative bone texture could be used to create a model with a sensitivity of 75% and a specificity of 80% when predicting those subjects with cemented implants who went on to more than 0.4mm total migration by one year. Bone mineral density of the proximal tibia, as determined by clinical scanners, was not found to increase the accuracy of implant migration group classification.

An empirical fit to central regions of a purposed-built cross-wedge calibration phantom returned residuals of less than ±1.5% for the bone-equivalent thicknesses. The coefficient of variation of the region greyscale values in three images spread over three days is under 4%, showing the stability of the system to hold a calibration between phantom exams and patient scans. Scatter and dynamic range issues will need to be considered for an accurate calibration across the full range of areal bone mineral densities in the distal femur and proximal tibia.

List of Abbreviations Used

AP	anterior to posterior view.
BMD	areal bone mineral density.
CT	computed tomography.
DXA	dual-energy x-ray absorptiometry.
FMP	first moment of the power spectrum.
minFMP	minimum FMP over 15° increments.
MTPM	maximum total point motion.
OA	osteoarthritis.
OOB	out of bag (error estimate).
ROC	receiver operating characteristic.
ROI	region of interest.
RSA	radiostereometric analysis.
SR Suite	Stereoradiography Suite at the Halifax Infirmary allows for two multiplanar x-ray images to be taken at the same time.

Glossary

arthroplasty

joint replacement surgery

aseptic loosening

mechanical loosening of the implant, without infection

beam hardening

average energy of x-ray beam shifts higher as it moves through material, due to the preferential attenuation of lower energy photons

bone microarchitecture

how bone is laid out on mm to cm scales, as opposed to whole bone geometry or bone matrix composition

bone mineral density

amount of hydroxyapatite mineral per square cm (areal measurement)

bone quality

no universally accepted definition, most often used to describe a bone's ability to resist fracture under load

calcium hydroxyapatite

crystalline calcium phosphate ($Ca_{10}(PO_4)_6(OH)_2$), mineral component of bone matrix

calibration box

a box placed under the exam table which contains control and fiducial beads in three dimensions to allow for spatial alignment of the two RSA exam images

calibration phantom

see cross-wedge phantom

cone-beam

x-ray photons generated at a point source expand out in a cone to cover the detector area

continuous migration

implant does not stabilize after one year and has a change in position over the second year greater than a prescribed cut-off

control beads

tantalum beads embedded in the control box; circled by metal washers that show up in the images as halos around the bead

cross-wedge phantom

two step wedges placed perpendicular to each other to provide full spectrum of material thickness combinations; for *in vitro* testing of x-ray measurement

dual-energy x-ray absorptiometry

using the attenuation properties of bone and soft tissue under low and high energy x-ray to determine bone mineral density

first moment of the power spectrum

average spatial frequency weighted by the power of the spectra (Fourier transform magnitude of the frequency squared), see Equation 3.1

fluence

total number of photons per unit area

flux

flow of photons per second per unit area

Fourier transform

transformation of a signal or image into the sum of sine waves

fractal dimension

measures self-similarity of a pattern over a number of scales

Gini coefficient

summary statistic to describe distribution of light over the pixels; 0=evenly distributed, 1=all light in one pixel

histomorphology

study of microscopic anatomy

maximum total point motion

the point of the analyzed rigid body (either network of tantalum markers or the model of the implant) which deviated the most from the reference exam

metaphysis

wide end of a long bone

migration

displacement of the implant compared to its original location relative to the tibia bone

osteoblast

bone cell that produces unmineralized matrix

osteoclast

bone cell that resorbs bone matrix

osteolysis

dissolution of bone

osteoporosis

thinning of trabecular bone and low bone mineral density as measured by DXA

plastic deformation

with stresses above the elastic limit, the material permanently deforms

radiograph

two-dimensional x-ray image

radiopaque

opaque under x-ray radiation

radiostereometric analysis

method of precisely determining implant migration compared to the bone via small radiopaque markers

Random Forest™ models

ensemble classifier with built-in error checking

region of interest

rectangular selection on the image to encompass the section of bone to be analyzed

registration

process of aligning two images, e.g. the high and low energy image of the same anatomy

resorption

assimilation of a substance

revision

replacing an implant, as opposed to primary arthroplasty

ROC curve

plot of false positive rate against true positive rate, generally different cut-points of the model are plotted to show power of the model to predict outcome

sensitivity

true positive rate of a test

stress shielding

change in load pattern so the joint forces are channelled away from the peri-articular bone; causes bone resorption

Stryker Peri-Apatite

The Stryker® Triathlon® Knee System with Peri-Apatite™ (Stryker Orthopaedics, Mahwah, NJ); a total knee replacement implant system used in one of the uncemented studies

Stryker Triathlon

The Stryker® Triathlon® Knee System (Stryker Orthopaedics, Mahwah, NJ); a total knee replacement implant system used in the cemented study

subchondral

below the cartilage

survivorship

probability that the implant remains unrevised

texture analysis

assessing the contrast, complexity, or roughness of an image using various techniques

texture inpainting

method of removing artifacts in an image by replacing the artifact with the best predicted combination of background texture

trabecular bone

bone matrix laid out on in a sponge-like pattern, found at the ends of long bones

wavelet analysis

similar to the Fourier transform, but by using discrete wavelets instead of continuous waves, spatial information is kept

Wright Medical Biofoam

The Wright Medical ADVANCE® Knee System with Biofoam™ Cancellous Titanium Tibial Base (Wright Medical Technology, Inc., Arlington, TN); a total knee replacement implant system used in one of the uncemented studies

Acknowledgements

Research is always a collaboration, and in the end, I don't know that I can even count the number of people who assisted in this part of the puzzle.

To my supervisors Michael Dunbar and Daniel Boyd, you opened up a whole new world and constantly encouraged me to dig deeper and speak clearer than I knew I was capable of. To my supervisory and examining team, I couldn't have pieced together this multifaceted project without your dedication, even when already stretched to the limit.

Elise Laende and Allan Hennigar, you both took on way, way more than your job description, and there's no way I would have made it through without you.

I appreciate each and every study participant, who dedicated time and resources to potentially help others down the road. And the School of Biomedical Engineering, who continues to ask every year, how to be better than the year before.

Halifax Biomedical, thank you for a fruitful collaboration, you've got an exciting road ahead! And thank you to the Atlantic Opportunities Agency and NSERC: CREATE for recognizing the need for academic-clinic-industry partnerships, and funding this venture.

Life isn't only the quest for new insight, and there have been countless people who have stepped up to help in work and at home to make sure that I had the ability to continue with this research. Thank you for your understanding, and for your support!

Chapter 1

Introduction

1.1 Overview

In 2006, there were 37,943 hospitalizations for knee replacements performed across Canada, not including Quebec, an increase of 140% over the previous decade [1] (see Figure 1.1). While these procedures are highly successful within the first 10 years post-surgery [2], in younger patients, who in general place higher physical demands on their joints, implants are less likely to last [3]. Canadian knee arthroplasty rates in the 45-54 age group increased over 300% in females between 1998 and 2007, and more than doubled for males [1]. Revision surgery outcomes are less reliable, with lower satisfaction rates than for primary procedures [4, 5, 6, 7]. The lifespan for revision implants is shorter than primary [6, 8], further exacerbating the problem.

There are currently no patient-specific biometrics to assess risk of implant failure for individual patients. This work examines the role of bone quality on implant stability, as part of a greater effort to provide clinically relevant risk assessments pre-surgery.

This chapter provides an overview of the state of arthroplasty today, implicated causes of failure and measurement of implant stability, bone structure, and radiographic imaging techniques. At the end of this chapter, hypotheses and rationale for the work are outlined.

1.2 Osteoarthritis

Osteoarthritis (OA) is a complex disease of the synovial joints which may include abnormal changes to bone, cartilage, meniscus, synovium, ligaments and other soft

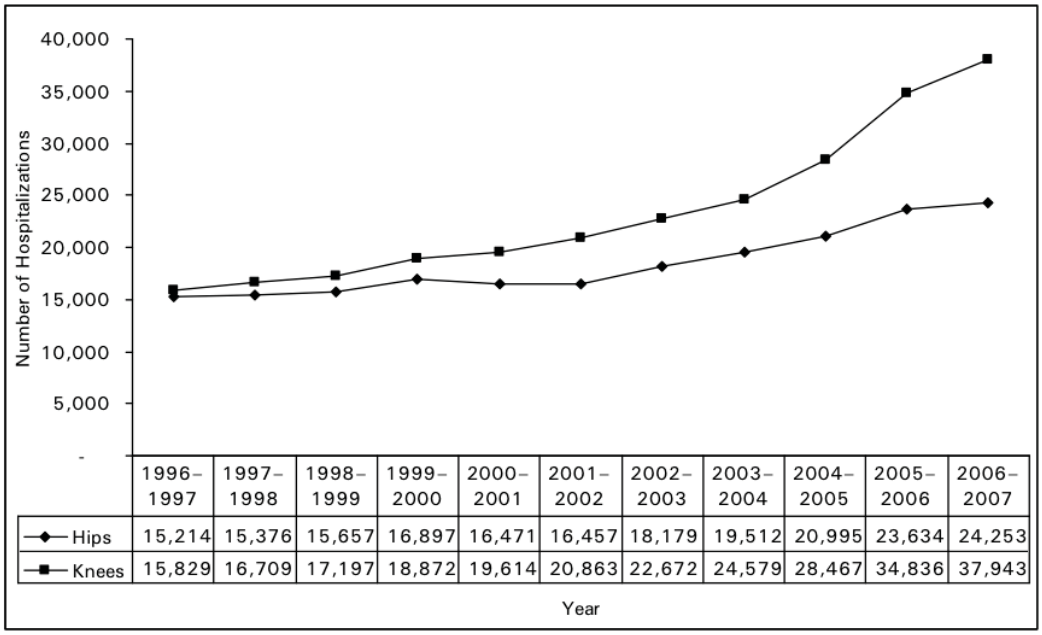

	1996–1997	1997–1998	1998–1999	1999–2000	2000–2001	2001–2002	2002–2003	2003–2004	2004–2005	2005–2006	2006–2007
Hips	15,214	15,376	15,657	16,897	16,471	16,457	18,179	19,512	20,995	23,634	24,253
Knees	15,829	16,709	17,197	18,872	19,614	20,863	22,672	24,579	28,467	34,836	37,943

Figure 1.1: Number of hospitalizations for hip and knee replacements in Canada (excluding Quebec) [1].

tissues; results in the breakdown of cartilage and bone [9]; and is the most common diagnosis for joint arthroplasty [4, 1]. Symptoms of OA include joint pain, stiffness, functional limitations, fatigue, mood changes, sleep disturbances and reduced quality of life [9]. Ten percent of Canadians are currently afflicted with osteoarthritis, and 21% to 26% of Canadians will be impacted by arthritis or rheumatic conditions by 2021 [10]. Arthritis and related conditions are the most commonly reported cause for physical disability in Canada [11], and carry an economic burden equivalent to 0.8% of the GDP, or $5.9 billion in 1994, including reduced productivity [12].

The cause of OA is varied and not completely understood (see Table 1.1). Joint stresses are a factor, but patient differences in soft tissue and joint structure and use characteristics means that determining initiating and progression factors is difficult [9].

Demographic trends of an ageing population, increased life expectancy, and growing obesity predict an increasing rate of arthroplasty procedures, and those combined with the extension of joint replacement into a younger population means a higher demand on the function of those new joints and an increased likelihood that revisions of these procedures will be required [5, 14]. Of the total knee replacement

Table 1.1: Factors influencing osteoarthritis incidence or progression (adapted from [13].

Systemic Factors Affecting Joint Vulnerability	Intrinsic Joint Vulnerabilities	Extrinsic Factors Acting on Joints
age	previous damage	obesity
gender	periarticular muscle weakness	physical activity
genetic susceptibility	malalignment	
nutritional factors	proprioceptive defect	

procedures reported to the Canadian Joint Replacement Registry in 2006-2007, 55% of patients were classified as obese (BMI $\geq$ 30) and a further 32% were overweight (BMI of 25 to 29.9)[1]. Future demand is difficult to predict accurately, as there are not only population demographics to take into account, but also shifts in lifestyle habits, immigrant population, prevailing medical opinion on treatment options, and new innovations [5]; in the US, forecasts range from three quarters of a million to four million hip and knee replacements performed each year by 2030 [2, 15].

1.3 Arthroplasty

In Nova Scotia, the general (primary care) practitioner (GP) refers a patient to an orthopaedic surgeon for diagnosis and treatment of knee OA. X-rays are ordered before the specialist consultation, but may or may not be viewed by the GP before referral. The surgeon discusses the patient's experiences of pain and disability, views the radiographs to look for joint space narrowing and other indicators of OA, tests range of motion of the joint and watches the patient walk. From these, mostly qualitative, analyses, the advisability of total joint replacement is weighed by both patient and physician.

In 2004, the Canadian federal government listed joint replacements as one of five procedures targeted for wait time reduction [1]. With a goal of surgery within 26 weeks from the time of the decision for surgery, currently 60-69% of knee patients obtain their joint replacements within that window, but in Nova Scotia, even though our wait times have been consistently decreasing, still less than 50% of patients receive surgery within the target time frame [16].

Along with high demand and health care resources, two other issues are impacting the wait list times. Firstly, the lack of evidence based rationale for follow-up post-arthroplasty has lead to a standard of care of yearly radiographic examinations and follow-up with the orthopaedic surgeon [17, 2]. If a diagnostic method were determined to predict those patients whose implants will likely remain stable for a number of years, the burden of follow-up on the surgical and radiological staff could be reduced, thus allowing for more replacement surgeries with current capacity, as well as easing the need for long distance travel of many patients in Nova Scotia. Secondly, the limited lifespan of the implants themselves, as eluded to earlier, increases the number of surgeries that must be performed.

1.3.1 Radiostereometric Analysis (RSA)

One of the difficulties in following patients post-arthroplasty, is determining if the joint replacement is stable, as loosening is often asymptomatic [18]. Radiostereometric analysis (RSA) uses small, radiopaque tantalum beads inserted into the bone and the polyethylene portion of an implant (or a model of the implant itself) to measure the migration of the implant compared to its original location relative to the bone to a high degree of accuracy [19]. Presently used for research and testing purposes, it provides important information as to the long term status of an implant: Ryd et al. [20] showed that the RSA measured migration at one and two years post surgery has a predictive power of 82% (n=131) for implants at risk of continued loosening. They further show that of 14 implants needing revision, 12 of them would have been identified at two years with a combination of RSA migration measures. Grewal et al. [21] also support the theory that early migration is connected to early failure: of three groups with different types of implants (n=192, 75, and 118) followed up to 13 years post-operative, the clinical group that had the highest survivorship numbers had the least migration at one year post-operative, and those with the most migration were in the group that also had the lowest survivorship rates (p¡0.05). While knee replacement studies remain limited, there have been a few more studies in hip arthroplasty, where there is some dispute about what constitutes “high migration”. Some agree with Ryd et al.’s knee study that the rate between years 1 and 2 is the important metric [22], but others point to an absolute migration value at 12 or 24 months[23, 24]. The type of implant fixation used in these trials may be part of the

explanation for the difference, where uncemented implants migrate more initially in comparison to cemented fixation, but stabilize[25, 26, 27].

The ability of RSA to identify implant designs with a higher risk of poor performance in a couple of years with relatively small study numbers [28], when this once took decades to uncover with survivorship studies, has been a real boon to research and shows potential for patient follow up post-surgery[19]. This method only provides a more precise tool to measure implant stability, however; it has no way of predicting which patients will develop an at risk migration pattern to begin with.

1.3.2 Implant Failure

Revising joint implants puts further strain on a health care system: in 2003, 7.5% of knee replacement surgeries were revisions in the US [15], and these procedures are more complex, with lower satisfaction rates than for primary procedures [29, 5, 7]. The lifespan for revision implants is shorter than primary [7], which perpetuates the cycle.

The most common cause of implant failure is aseptic loosening [3, 15, 1]. Aseptic loosening can have a complex etiology involving fixation (both initial fixation and later fatigue failure), implant design, joint alignment, mechanical environment (gait mechanics, activity level, and any inappropriate loading), hydrodynamic pressure, and wear particles from the replaced joint which can induce an inflammation response and bone resorption (osteolysis)[30, 31, 32, 33]. Micromotions from high strains at the bone-implant interface causing fatigue deformation or a failure of initial fixation are implicated in cell mediated bone resorption [34, 32, 35]. Osteolysis is the dissolution of bone, most often seen as a series of pockets or lesions as an immune response to wear particles triggers foreign-body inflammatory cells and a bone resorption cascade [33]. An increase in hydrodynamic pressure from joint fluid has also been suggested as a mechanical means of influencing the extent and distribution of peri-implant osteolysis by turning on osteoclast activity [32]. Osteolysis is generally asymptomatic [18], and any bone resorption can make revision surgery more challenging and increase the chance of fracture [36, 37]. Unfortunately 2D x-ray images are of limited value in diagnosing bone resorption: they can fail to show lesions and radiolucent lines entirely, or underestimate the amount of bone loss due

to the projection of the surrounding bone in the line of sight [18, 38].

In order to improve wait times and keep joint implants working well longer, and for more people, we need to be able to determine which patients may have trouble as early as possible, hopefully even before the first surgery.

1.4 Bone

Bone is a complex, living composite of organic molecules, inorganic mineral, and a web of cells. Built up in a hierarchical manner (see Figure 1.2), collagen and hydroxyapatite mesh together to form the bone matrix, and that bone matrix is laid out in complex patterns depending on physiological loads and anatomical location.

1.4.1 Bone Composition

Bone matrix is comprised of an organic phase, an inorganic phase, and a cellular population. The organic phase is largely type I collagen, which provides tensile strength and toughness. The inorganic phase is mostly calcium hydroxyapatite mineral, adding compressive strength and stiffness. The hydroxyapatite crystals are positioned at the ends of, and between, the collagen fibres creating a matrix that is both viscoelastic and rigid, and these bundles are used to build larger structures [39]. Osteoblast cells produce the unmineralized bone matrix (osteoid) which is later mineralized, and once they become trapped in the new bone they mature to osteocytes which maintain the bone. Osteoclasts resorb bone and are needed for bone turnover in cases of injury, remodelling initial woven bone into stress aligned lamaller bone, or due to a change in force loading patterns.

The elastic modulus (the amount of strain or deformation per unit of stress) of bone tissue is highly correlated with mineralization and porosity, and a small change in mineral density can have a disproportionately large effect on bone tissue strength [41]. The relative amounts of bone mineral and collagen affect the mechanical properties of the tissue, as does the configuration: lack of collagen cross-linking has been shown to influence fracture risk as it is the ductility of collagen that is able to absorb and store energy [42, 43, 44].

As Wolff's Law describes, healthy bone continuously evolves based on the mechanical environment, and adapts to the strains placed upon it through remodelling

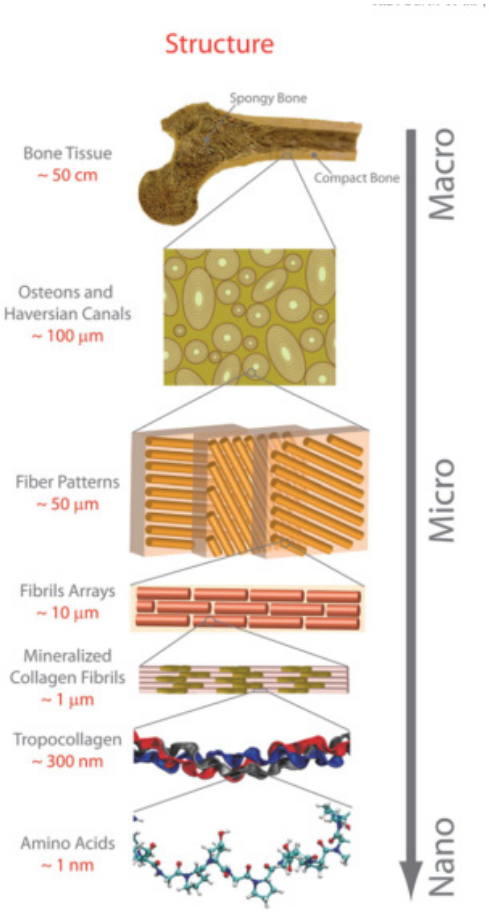

Figure 1.2: Hierarchical structure of bone [40].

[39, 45]. This cellular response is altered by age and disease, with changes in bone matrix composition and the ratio of bone formation to resorption [45].

The mechanical properties of the bone matrix are only part of the picture, however.

1.4.2 Bone Structure

Bone matrix is built up into a skeleton that is optimized to operate under physiological stresses without snapping yet remaining lightweight. The long bones of the femur and tibia have a shaft of thick, dense cortical bone distributed away from the central axis, with a higher elastic modulus and strength when loaded longitudinally, and which resists the tension which comes with bending moments [41]. At the ends of the shaft, the bone flares out into the metaphysis, which is mainly comprised of trabecular (spongy) bone with a honeycomb-like structure able to withstand compressive forces without fracturing, which is important at the joints. The mechanical properties of trabecular bone are derived from the number and separation of the struts, their thickness, and their interconnectedness.

1.4.3 Effects of Disease States on Bone Structure

With a much higher surface area, trabecular bone has a higher turnover rate, thus the locations with high trabecular bone content (femoral head, vertebrae) are where osteoporosis first appears [46]. On a microarchitectural level, it appears first as a thinning and removal of the interconnecting rods in trabecular bone, which decreases the amount of bone mineral per given area, even though the bone matrix that remains has the same amount of mineral as normal [39]. Osteoarthritic bone, on the other hand, often has raised areal bone mineral density with subchondral sclerosis as the horizontal trabeculae thicken. At the same time the bone matrix in this area contains more water and is less mineralized, thought to be indicative of immature bone due to high turnover as shown with elevated biomarkers of both bone formation and resorption [47, 48].

Teasing out the sources of mechanical properties of bone is difficult, as bone composition and architecture parameters can both be affected by the same biological processes [45]. In addition, bone failure is dependent both on the local mechanical properties of the bone and the external and internal forces that are applied; a

sufficient bone quality for every day activities might fail when loaded off-axis in a fall [41].

1.4.4 Bone Responses Impacting Implant Stability

Theoretically, bone quality is thought to impact implant stability in a number of ways. First, the implant may not become properly fixed to the bone from the beginning (in the case of a cemented implant, a proper interdigitation of cement with the pores of the trabecular bone must take place, and for uncemented implants, the trabecular bone must grow into the rough texture provided on the surface of the implant). Second, the bone may not be able to withstand the new loading pattern; implant materials are stiffer than bone, and thus joint stresses get channelled down the stem of the the implant into the interior distal portion of the metaphysis which did not originally experience such loads from that direction. And thirdly, bone resorption may occur at the implant or cement-bone interface. (See Bauer & Schils 1999 [32] for a more expanded description of implant failure mechanisms.)

Initial micromotion of the implant, which could be related to an initial lack of fixation or low bone modulus, can have consequences: there is a limit to how much an implant can move and still allow for bone ingrowth in uncemented designs (too much leads to a fibrous encapsulation which leads to a higher risk of failure) [34], micromotion aids the production of debris particles [30], and micromotion indirectly activates osteoclasts [35]. Motion also can cause an increase in hydrodynamic fluid pressure in the effective joint space, which also may lead to bone resorption [32].

Finite element analysis (FEA) of stresses in bone have shown the possibility of plastic deformation of the trabecular bone due to implant loading [49, 50, 51]. While these analyses are difficult to do rigorously, as every patient has a different bone geometry, bone matrix quality, and joint alignment, studies have shown the global stress distribution with three different types of implant fixation (cemented, proximally bonded hydroxyapatite coated, and press-fit) matched the clinical migration and survival rates of these types of implants (n=39, 57, and 24 respectively) at 2 and 5 years (FEA designs by Taylor et al. [50, 51] and compared to survivorship rates in Grewal et al. [21]). It is thought that an initial rapid subsidence is due to the turn-over of necrotic bone from surgical trauma, but that the slower, continuous migration in the medium term might be due to plastic deformation of the bone as

the strains overwhelm the body's ability to repair the damage [49]. Whether the medium term migration is due to plastic deformation of trabecular bone, or whether the bone is being resorbed and the implant migrating into the larger space is unclear. It does indicate, however, that the local bone environment is more important than global bone properties for implant stability [52].

Resorption occurs in response to many factors: altered stress patterns, ageing, inflammation induced osteolysis (from infection or particle debris), implant motion, high fluid pressure, and metabolic disturbances [32]. Early analysis of aseptic loosening pointed to osteolysis as the cause, and cement particles as the reason for the osteolysis (then termed "cement disease" [53]), which led to the design of cementless implants. We now know that wear particles from all components of the implant (e.g. polyethylene, metal, ceramic) and not just the cement do trigger some immune reaction, but a large number of particles does not necessarily mean osteolysis occurs [37]. It is thought that the particles follow the path of least resistance, and become a threat when the reaction is happening in periprosthetic bone: the effective joint space includes unbonded sections of the implant, places where the cement is fractured or is defective, screw holes and cannulated stems, each allowing particles to build up next to the implant and promote bone resorption where the bone is needed most [32, 35, 54].

A brief comment about stress shielding. Bone resorption due to lack of loading on periarticular bone after arthroplasty has been studied extensively. The stiffer metal causes the joint forces to travel through the implant to the base of the shaft instead of through the head of the bone, and the changed mechanical environment means the dense periarticular bone is no longer needed. There have been many new implant designs introduced attempting to minimize stress shielding, but while the there are direct links between inflammation based osteolysis and implant failure, the consequences of stress shielding are more in doubt. It has been a concern theoretically in terms of long term implant stability and chance of periprosthetic fracture [55, 56, 57], but this adaptive remodelling has been seen to be continuous for up to 14 years while the implants remain stable [4], few clinical problems have been related to this type of bone resorption, and it has rarely been found as an isolated cause of implant failure [32, 58, 49]. It becomes more of an issue when an

implant becomes loose through pathologic resorption, and needs replacement: in such case there may be less bone for the revision implant to use as a base, and this negatively impacts the success of revision surgery [59, 60, 55].

But even with these research results, the question still remains: which aspects of "bone quality" are necessary for implant longevity? And can some of them be measured using radiographic images?

1.5 Imaging Techniques

Most of the research into radiographic measures of bone quality centre on osteoporosis diagnosis. The gold standard radiographic measure of bone quality: bone mineral density (BMD) measures the mass of bone mineral per projected area (g/cm^2) on a two-dimensional x-ray image. More properly termed areal bone mineral density, it is the basis of the World Health Organization's definition of osteoporosis: "an areal bone mineral density value that is 2.5 standard deviations or more away from the young adult mean". Being a two-dimensional measurement, BMD encapsulates parameters of bone mineralization, porosity, and cross-sectional bone size and may not be a good measure of volumetric or bone tissue density [60, 61, 62]. BMD necessarily combines cortical and trabecular bone densities, thus will not be as sensitive to trabecular bone turnover rates as three dimensional modalities [63]. Even with all of these negative influences, BMD still explains 70% of the variance in stiffness for femur and tibia bones, 73% of the ultimate strength and 81% of the penetration strength of trabecular bone *in vitro* [60, 64, 65]. This does not completely translate into fracture risk *in vivo*: 60% of fracture risk is explained on a population scale, as proven in large epidemiological studies [66, 67, 68]. The correlation of bone mineral density to mechanical properties of the bone may prove useful, as bone response to the stresses transmitted through the implant have been implicated in implant migration.

1.5.1 Dual Energy X-ray Absorptiometry

Visual analysis of plain radiographs can only reliably detect a decrease in density once a minimum of 30% of the bone is lost [4, 69]. The current gold standard for

high accuracy measurement of areal bone mineral density is dual-energy x-ray absorptiometry (DXA) which takes advantage of the x-ray attenuation properties of the various body tissues. At energy levels used for diagnostic imaging, x-ray photons interact with atoms in the tissues in two ways: (1) photoelectric absorption, where the photon is absorbed and an inner shell electron is ejected from the atom, and (2) Compton scattering, where the photon interacts with an outer valence electron causing a change in direction of the photon. Photoelectric absorption is more effective in high atomic number atoms (for instance, calcium) vs. the hydrogen, carbon, and oxygen found in soft tissue, but scattering is dependent only on electron density, which is similar for all tissue types [70]. The total attenuation (scattering and absorption reduction of incident photons) at high and low energies provides a unique fingerprint for each tissue type. The photon fluence that reaches the detector is the number of photons emitted by the generator attenuated by the matter in the path of the beam, as shown in equation 1.1 for a monoenergetic beam and single type of matter [71], where I_f is the intensity at the detector, I_o is the incident intensity, t is the thickness of matter in the way of the beam, and μ is the linear attenuation coefficient of that matter.

$$I_f = I_o e^{-\mu t} \tag{1.1}$$

The attenuation coefficient is dependent on x-ray energy; for single energy beams the coefficient is constant, and a simple exponential multiplier based on the thickness t of the material relates incoming and transmitted intensity. It is worth noting that photoelectric absorption dominates at lower x-ray photon energies and scattering at high energies, thus two images are taken centred on the photoelectric and Compton domains respectively [72, 73]. The atomic composition of the soft tissues (lean muscle, adipose tissue) mean that their attenuation coefficients are similar, but different from that of bone at lower energies. In this way the body can be broken into two tissue types ("soft tissue" and "bone") and when imaged using two different x-ray energies, the attenuation equations allow for two equations with two unknowns (1.2 and 1.3), providing the ability to solve for the thickness of bone [74].

$$I_{f_1} = I_{o_1} e^{-(\mu_b t_b + \mu_{st} t_{st})} \tag{1.2}$$

$$I_{f_2} = I_{o_2} e^{-(\mu_b t_b + \mu_{st} t_{st})} \tag{1.3}$$

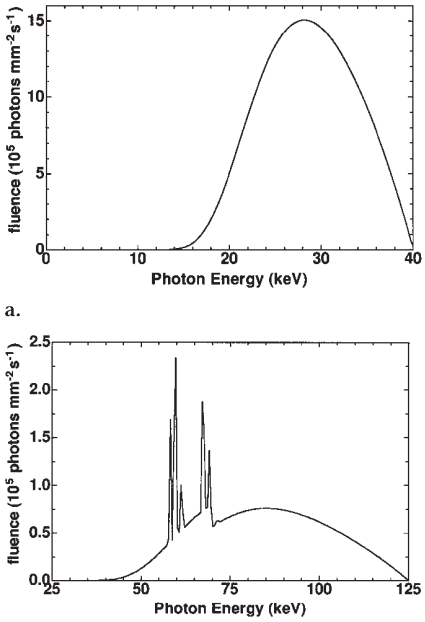

Figure 1.3: Example low and high energy x-ray spectra. Figure from Gulam et al. 2000 [75]. Copyright Radiological Society of North America, used with permission.

Dual-energy x-ray absorptiometry uses an electrical generator of photons, which provides consistent, high flux beams at the cost of having a broad energy spectrum (Figure 1.3). Assessment of bone mineral density for clinical diagnosis of osteoporosis is now exclusively the domain of dedicated scanning equipment. Pencil-beam machines (in which the transmission of a highly columnated photon beam is recorded by one pixel detector, which is scanned over the anatomy in question) have largely been replaced with fan-beam designs (beams expand through a slit columnator to record a row or few rows of pixels at a time). DMS-Lexxos (DMS Corporation; Montpellier Prols, France) is the only company making cone-beam (2D) machines that can image the hips and spine [76, 77].

Dedicated scanners are quite precise in the short-term (with a coefficient of variation of 1 - 1.5% for spine BMD, and 2 - 2.5% for femoral neck for fan beam detectors [67]), and a very stable calibration [62], although long-term effects of small drifts in calibration and patient positioning and tissue composition changes can add up to a minimum significant change of 6.5% [78]. While DXA scanning can be very precise, it is under stringent conditions. Position and rotation must be strictly controlled, as a change in the angle of the x-ray beam through the bone changes

the path length of the photons and the region of bone being imaged [67, 4, 79, 80]. Standard operating procedures include instructions on positioning, including the use of foam blocks and foot positioners to increase repeatability. Changing the outlined region of interest (ROI) can also affect the resulting BMD value: an optimal ROI is large enough for precise repositioning, but small enough to cover bone that has uniform mechanical and physiological conditions [67, 78].

1.5.2 BMD and Arthroplasty

BMD has been tracked post-arthroplasty, mostly in terms of following the progression of stress shielding. Pre-operative BMD is not usually measured [58]. It has been well documented that BMD in the area surrounding the implant decreases in the first 12 weeks to 6 months after surgery, likely due to postoperative increased bone resorption and decreased patient activity [58, 81, 82]. Longer term studies have shown that BMD continues to decrease in the proximal periprosthetic zones faster than normal ageing [4, 82, 83], but stabilizes and increases in other areas over the following two years [81, 82, 57]. Studies of pre- and post-arthroplasty bone mineral density and knee and hip implant stability have had conflicting results. Some research has shown that the percentage of mineral lost over time is related to initial BMD [84, 52, 57], low initial BMD is correlated with early migration [26, 85], loose implants have lower periarticular BMD [86, 87] or less change in BMD [26, 27], failure of cemented femoral hip implants are related to regional losses in BMD [86], and for some surgeons, lower bone mineral density or poorer bone quality pre-operatively has been the reason to choose a cemented implant over a press-fit design, as the cement is thought to compensate for variations in bone stock [85, 80, 58]. On the other hand, other studies found that initial BMD was *not* related to percentage lost post-arthroplasty [82, 83], nor was type of implant fixation implicated [52], no evidence has been found that low BMD is related to long term loosening, migration, or implant failure [27, 58, 54, 79, 88], and histomorphologic diagnosis of osteoporosis shows no relationship with RSA measured migration at one year [89] or loosening after 12.8 years [90]. It is difficult to compare study results, however, as loosening has a multifactorial origin (see Section 1.3.2), and differing inclusion and exclusion criteria, age and other demographics, activity levels, regions of interest, assessment methodology, surgical technique, and implant type can all impact the outcomes.

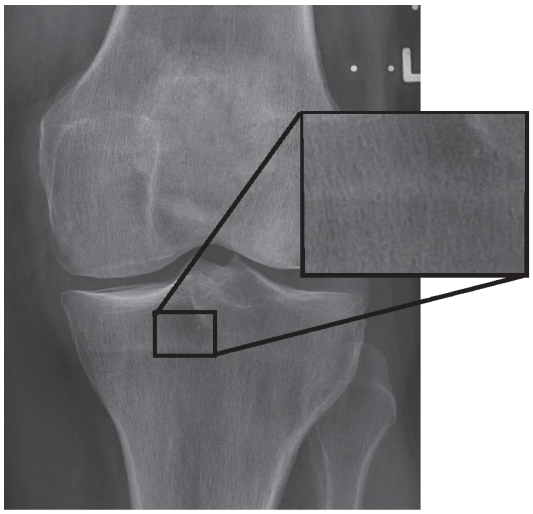

Figure 1.4: Trabecular bone structure seen in 2D projection radiographs

Which is to say that there's no clear relationship between bone mineral density and implant stability. Current research in the osteoporosis field is also attempting to improve prediction of bone failure by adding other markers of bone quality, including examining the microarchitecture of bone [91, 92].

1.5.3 Two Dimensional Bone Microarchitecture Assessment

As discussed in section 1.4, the layout of the trabecular bone at the ends of the long bones impacts their mechanical function. This is the bone which needs to supply some support for a total joint replacement implant, whether through the interdigitation of cement with the sponge-like texture of trabecular bone or through bone ingrowth into the rough exterior of an uncemented implant. While some of the information is lost in two-dimensional projection imaging, the dominant structures of the spongy bone can still be seen in radiographs (see figure 1.4). Image texture analysis is a large area of study, and has been used previously in the medical field (e.g. differentiating between normal and abnormal tissue and segmenting images based on anatomical structures). Since the pattern that trabecular bone makes on x-rays has already been used visually to determine pathology (e.g. the Singh Index for osteoporosis), it is unsurprising that automated texture techniques have been attempted on bone as well. Image texture analysis is generally split into three classifications: (1) statistical methods (comparing grey scale intensity levels of each pixel with their neighbours based on statistical techniques), (2) transform methods

(usually using the Fourier transform to obtain spatial frequency data), and (3) model methods (principally fractal based parameters, giving an indication of overall roughness or complexity) [93, 94]. Table 1.2 contains an overview of the texture analysis currently being applied to bone images (both *in vitro* and *in vivo*), almost exclusively to add to the portrayal of bone quality in predicting fracture risk.

In osteoporosis studies, texture analysis was found to be not as good at predicting fracture risk as BMD, although combining texture and BMD gives a more sensitive and specific predictor [112, 113, 108, 92]. Texture analysis has shown a significant change in trabecular bone structure over time in the tibias of osteoarthritis knee patients [98], and is potentially sensitive to hormone replacement therapy and teriparatide treatment of osteoporosis, which BMD is not [91]. Different techniques reflect different characteristics of the trabecular pattern, and vary in their relation to BMD and biomechanical properties [99, 102], although most have shown significant correlation with bone strength (including torque to breakaway of a wing blade probe in cadaver femoral bones [97], and a high correlation between power spectrum texture and elastic modulus [99]) and can give anisotropy measures important for biomechanical responses that are missing in density values [103, 114].

Some suggest that the older statistical methods such as grey level co-occurrence matrices are being superseded by multivariate image analysis such as the wavelet transforms [93], although these methods still appear in papers published in the last couple of years [95, 115]. The difficulty with the statistical methods are the shear number of parameter options: multiple statistical analyses are conducted on the matrices, which themselves are dependent on the number of pixels to compare, as well as the distance between the pixels, and the direction. While there are published results stating that this set or that have been found to correlate with medically important indicators, none have described an exhaustive search of which variables are best, and the optimal parameters are different for varying imaging techniques [116]. Statistical methods have no link to physical structure, so there is no theory to act as guide [116].

Fractal dimension is thought to reflect the complexity of the trabecular branching, and perhaps contain information about the 3D properties of the bone [105, 117].

Table 1.2: Texture analysis of bone in the literature

Statistical	Transformational	Fractal
grey level co-occurrence parameters [93] (theory, n=35 steel images), [94] (n=33 bone specimens), [95] (n=40 pairs of excised femurs), [96] (n=54 BMD matched patients, hips imaged) [97, 98, 99]	**root-mean-squared of the power spectrum** [100] (n=34 bone specimens), [101] (n=42 with vertebral fractures n=128 without, postmenopausal women, calcaneus images)	**Fourier based fractal** [99] (n=28 bone specimens) [102] (n=87 bone specimens), [94, 103]
	moments of power spectrum [38] (n=202 total hip arthroplasty patients), [99, 100, 101]	**Minkowski Dimension** [97] (n=14 pairs of cadaveric femurs), [48] (n=6 normal, n=5 osteoarthritic proximal tibia images), [101, 38]
	Laws masks [104] (n=114 osteoporotic and n=182 age-matched patients, calcaneus images) [98] (n=18 OA hip radiographs)	**surface-area fractal method** [103] (n=51 bone specimens), [105] (n=43 osteoporotic patients, spine images), [102, 48]
	wavelet analysis [106] (n=26 osteoporotic and n=23 controls, mandible images), [93]	**box-counting** [107] (n=25 femur bone specimens),[108] (n=30 radiographic and 16 CT images of lumbar vertebrae),[109] (n=26 vertebral specimens)
		fractal signature analysis [110] (n=90 OA knees, macroradiographs), [111] (n=40 OA knees, macroradiographs), [48]

The texture on projection images does exhibit fractal properties even though histological sections of trabecular bone do not [91].

In the context of arthroplasty, one study of 202 hip replacements has looked at bone texture in the context of aseptic loosening by means of correlation with osteolysis. Wilkie et al. [38] determined that both the minimum of the directional FMP (first moment of the Fourier power spectrum) and the Minkowski Fractal Dimension of regions around the acetabular cup separated osteolytic and non-osteolytic cases. This was a preliminary study however, and used radiographs that had confirmed osteolysis by visual inspection: the power in this technique will only come if it can determine loosening cases at a much earlier time frame, as conventional diagnosis requires quite a bit of bone to have already been resorbed. To find out if such parameters predict later loosening requires either large longitudinal studies, or a more sensitive measure of loosening than visual diagnosis of osteolysis.Another study by Wigderowitz et al. [46] looked at the short term texture response of the tibia medial and lateral compartments to a total knee replacement, and found a similar pattern to accepted BMD changes: a decrease in trabeculae in the first year, with the values of the fractal dimension returning to baseline by the third year, and a difference between two regions attributed to load distribution.

1.5.4 Why Not 3D?

Two dimensional projection radiographs have advantages over the more information-rich 3D modalities (CT and MRI) due to ease of use, low cost, short scan times, and availability as a screening device on large populations [18, 60]. The volumetric modalities also require modified techniques and algorithms in an attempt to remove artifacts produced by metallic implants which can severely impact image quality [118], and these techniques are not yet ideal. CT images are of lower precision and resolution than radiographs, and incur a much higher radiation dose [119], with that dose substantially increased again when an implant is present [118, 120]. There have been many studies linking 3D bone properties to 2D projection parameters [99, 121, 116], which gives us the ability to use the more accessible x-ray radiographs to obtain bone quality surrogate variables.

1.6 Purpose

The purpose of this study was to examine the link between radiographic measures of bone quality on implant stability as measured by RSA. Radiograph image texture analysis was used to characterize bone microarchitecture, and bone mineral density scans determined information about bone matrix content. These parameters were compared to assessed implant motions at one and two years after surgery, which Ryd et al. [20] showed predicted future loosening. A feasibility study was conducted to determine if the SR Suite at the Halifax Infirmary could be used to obtain another measure of bone quality, bone mineral density, as well as RSA measured migration.

1.7 Objectives and Hypotheses

Objective 1

Create an algorithm to assess bone microarchitecture of the knee, and combine with bone mineral density data from DXA scans. Evaluate the links between these measures of bone quality and uncemented total knee arthroplasty stability in the first two years post-operative as measured by RSA migration.

Rationale 1

Bone microarchitecture and bone matrix composition are both known to affect the mechanical properties of bone. FEM studies of implant-bone interaction show that stress concentrations which exceed the bone's ability to elastically deform and recover result in fatigue damage which alters the tight fit between the implant and the bone. RSA studies have shown that early continuous migration of an implant predicts later failure via mechanical loosening, and that migration between one and two years is predictive of continuous loosening. Implant stresses overwhelming bone mechanical properties may be one of the factors causing early continual migration.

Hypothesis 1

A model based on radiographic derived bone microarchitecture and bone mineral density parameters will identify study participants with RSA measured implant migration between one and two years above and below a set cut-point.

Approach 1

A total of 65 uncemented knee replacement study participants have been followed for two years, and have had RSA and DXA scans at post-operative, 3, 6, 12, and 24 months. Image texture analysis was conducted on the RSA exam radiographs. Random Forest™ statistical models were built using texture and mineral density parameters to determine if it is possible to classify implant migration outcomes based on bone quality.

Objective 2

Evaluate the links between peri-operative radiographic measures of bone quality and cemented total knee arthroplasty stability in the first year post-operative as measured by RSA migration.

Rationale 2

An extension of Rationale 1, this hypothesis examines the predictive ability of these bone quality parameters: can an exam taken before surgery (here using available images taken one to two days after surgery as a proxy for pre-operative bone condition) assess risk of implant instability?

Hypothesis 2

A model based on radiograph derived bone microarchitecture parameters calculated from immediately post-operative x-ray images will predict study participants with RSA measured implant migration at one year above and below a set cut-point.

Approach 2

A total of 16 cemented knee replacement study participants have been followed for one year, and have had RSA exams with digital x-ray images taken at post-operative, 3, 6, and 12 months. Image texture analysis was conducted on the RSA exam radiographs. Random Forest™ statistical models were built using texture parameters to determine if it is possible to classify implant migration outcomes based on bone quality.

Objective 3

Assess the feasibility of obtaining bone thickness from x-ray images using the radiographic equipment in the SR Suite at the Halifax Infirmary.

Rationale 3

With a known volumetric density of cortical bone, the areal BMD can be determined if cortical bone equivalent thicknesses are measured from the radiograph attenuations. Two dimensional image based bone mineral density measurement has been successfully conducted in research on the hand. Using the SR Suite instead of dedicated DXA scanners offers much higher spatial resolution, and the potential to use x-ray exams for multiple purposes to reduce patient exposure.

Hypothesis 3

An empirical calibration of the system using an x-ray phantom with bone and soft-tissue mimicking materials will accurately identify the material thicknesses from high and low energy image greyscale values and maintain the calibration over one day.

Approach 3

A cross-wedge phantom was designed to cover the full range of bone and soft tissue thicknesses found in CT scans of 50 early OA study participants. X-ray exposure levels were tested to determine if a large spread in energies between high and low images was possible, and determine exposure levels which do not oversaturate thin areas while still being high enough to penetrate thick areas. An algorithm was written to take the greyscale values in the high and low energy images and fit a second order polynomial to link those values to the known thicknesses of the phantom. The fit was then used to reassess the phantom images to determine the uncertainty of the thickness measurements over the whole image.

1.8 Structure of the Remainder of the Thesis

Chapter 2 outlines the study data used in these projects, including specific information on the SR Suite equipment, RSA and DXA exams. Chapter 3 examines Hypotheses 1 and 2, describing the methods and results of obtaining radiographic image based bone microarchitecture parameters and determining if models based on these and bone mineral density can help classify study participants based on implant migration. Hypothesis 3 is investigated in Chapter 4, where the methods and results of cross-wedge phantom testing are described. Chapter 5 includes a discussion of the results, the limitations of these experiments, and directions for future work.

Chapter 2

Total Knee Arthroplasty Clinical Studies

Currently there are two uncemented total knee arthroplasty studies being conducted by the Department of Orthopaedics Research at the QEII Health Sciences Centre, and one continual-enrolment study of cemented hip and knee replacements which are monitored using radiostereometric analysis. Informed consent was obtained from all study participants in accordance with the requirements of the Capital Health Research Ethics Board. All exam data was anonymized by study coordinators before analysis.

2.1 Uncemented Knee Studies

2.1.1 Wright Medical Biofoam

The Wright Medical ADVANCE® Knee System with Biofoam™ Cancellous Titanium Tibial Base (Wright Medical Technology, Inc., Arlington, TN) ("Wright Medical Biofoam") is an uncemented tibial implant with foamed metal exterior to allow for bone ingrowth. The tibial implant provides the option to either use screws or not. Participation in this study was offered to subjects referred to three orthopaedic surgeons who fit the inclusion and exclusion criteria listed below, until 50 participants were enrolled. The study participants were randomized to receive screws or no screws, and the objective of the study is to assess whether screws have an effect on implant stability.

Inclusion Criteria

1. Symptomatic osteoarthritis of the knee indicating surgical intervention
2. Between the ages of 21 and 80 inclusive
3. Ability to give informed consent

Exclusion Criteria

1. Significant co-morbidity affecting ability to ambulate
2. Flexion contracture greater than 15°
3. Extension lag greater than 10°
4. Tibial subluxation greater than 10 mm on standing AP radiograph
5. Prior arthroplasty, patellectomy or osteotomy with the affected knee
6. Lateral or medial collateral ligament instability (> 10° varus/valgus)
7. Leg length discrepancy greater than 10 mm
8. Active or prior infection
9. Morbid Obesity (BMI > 40)
10. Medical condition precluding major surgery
11. Severe osteoporosis or osteopenia
12. Neuromuscular impairment

A total of 51 study participants were enrolled, with two withdrawn due to insufficient RSA beads visible for migration calculations. Joint replacement surgery took place between June 2008 and January 2010, with 45 completed 2 year RSA and DXA BMD scans available for analysis at the time of this work.

2.1.2 Stryker Peri-Apatite

The Stryker® Triathlon® Knee System with Peri-Apatite™ (Stryker Orthopaedics, Mahwah, NJ) ("Stryker Peri-Apatite") has a coating that encourages bone ingrowth. This design has a shorter flanged stem than the Wright Medical Biofoam, and is used in a muli-centre trial in Halifax and Perth, Australia. Due to the differences in patient population and x-ray equipment used, only the 18 study participants enrolled in Halifax are used in these analyses. Subjects referred to two of our surgeons were recruited based on the following inclusion and exclusion criteria:

Inclusion Criteria

1. Symptomatic osteoarthritis of the knee indicating surgical intervention
2. Between the ages of 21 and 80 inclusive
3. Ability to give informed consent

Exclusion Criteria

1. Significant co-morbidity affecting ability to ambulate
2. Flexion contracture greater than 15°
3. Extension lag greater than 10°
4. Tibial subluxation greater than 10 mm on standing AP radiograph
5. Prior arthroplasty, patellectomy or osteotomy with the affected knee
6. Lateral or medial collateral ligament instability (> 10° varus/valgus)
7. Leg length discrepancy greater than 10 mm
8. Active or prior infection
9. Morbid Obesity (BMI > 40)
10. Medical condition precluding major surgery
11. Severe osteoporosis or osteopenia
12. Neuromuscular impairment

Of the 18 subjects enrolled, 2 withdrawn at the time of primary surgery (one due to a missed exclusion, the other due to a deformity of the tibial plateau, unable to be determined before surgery), and 1 required revision after the first year for loosening. Primary surgeries occurred between April 2009 and April 2010, with 13 completed 2 year RSA and DXA BMD scans available for analysis.

2.2 Cemented Stryker Triathlon Study

There is a third study that began in the fall of 2010, with ongoing recruitment, which is open to those referred to one of 6 surgeons, scheduled for total hip or knee replacement, who are able to provide informed consent and attend required RSA exam follow-ups at the Stereoradiography (SR) Suite at the Infirmary. No other exclusion criteria is applied. All knee implants included in these analyses are Stryker® Triathlon® Knee System (Stryker Orthopaedics, Mahwah, NJ) ("Stryker Triathlon"), using cement fixation, and these study participants do not receive bone

mineral density scans. There is one subject with a Zimmer® Gender Solutions® NexGen® System knee, but the exam images had no usable regions of interest due to the spread of radiopaque cement further into the periprosthetic bone. Because this study started after the installation of the digital x-ray detectors, post-operative bone architecture can be examined and compared to later implant migration to test predictive value. However, only one year data (n=18) are available for analysis at the time of this report, and there is less support in the literature that one year migration values are useful in predicting later implant failure.

2.3 X-ray Detectors

Since July of 2010, the x-ray detectors used in the SR Suite are Canon CXDI-55C general radiography digital plates (Canon USA, Inc., Lake Success, NY) with 2208x2688 160 μm square pixels, 3.1 lp/mm resolution, and 12-bit grey scale range (4096 intensity levels). Exams completed before that date used the Agfa MD4.0 computed radiography system (Agfa HealthCare NV, Mortsel, Belgium), which had a lower effective resolution which resulted in the trabecular structure of the bone being not clearly visible. For this reason, only those RSA exams taken with the digital Canon detectors were used for the following texture analysis.

2.4 Radiostereometric Analysis

During surgery, small tantalum spheres 0.8 to 1.0 mm in diameter are inserted into the proximal tibia bone and the polyethylene insert of the tibial implant, in accordance with the ISO 16087 *Implants for surgery—Roentgen stereophotogrammetry for assessment of micromotion of orthopaedic implants* standard for uniplanar analysis. Tantalum is both biocompatible and radiopaque; the high contrast markers are easy targets for the semi-automated RSA analysis software during follow up exams comparing the relative positions of the implant to the bone.

Each Radiostereometric Analysis exam saves two x-ray views of the knee (Figure 2.1). These exams are taken with 90 kVp and 6.4 mAs for the average subject. The Model-Based RSA (MBRSA) software (version3.3, Medis Specials, Leiden, The Netherlands) takes these two images with known equipment geometry and back

Figure 2.1: SR Suite at the Halifax Infirmary. Dual x-ray heads at a 30° angle to vertical and a calibration box (HalifaxBox007, Halifax Biomedical Inc., Mabou, NS, Canada) under the table which houses the RSA spatial reference beads and the digital detector plates.

projects the path of the beams which created each marker shadow on the image. The intersection of these paths defines the true marker position in 3D space (see figures 2.2 and 2.3). The markers in the bone can be aligned in images at different time points, and any change in position of the implant relative to that rigid body is due to the migration of the implant. As per ISO 16087 recommendations, the maximum acceptable rigid body error was set to 0.35mm, and software identified bead positions were double checked if the error exceeded 0.30mm. The condition number maximum was set to 100, although very few exams exceeded 40, and were checked at this smaller value. All RSA measured implant migration of these studies was completed by Halifax Biomedical Inc. (Mabou, NS, Canada).

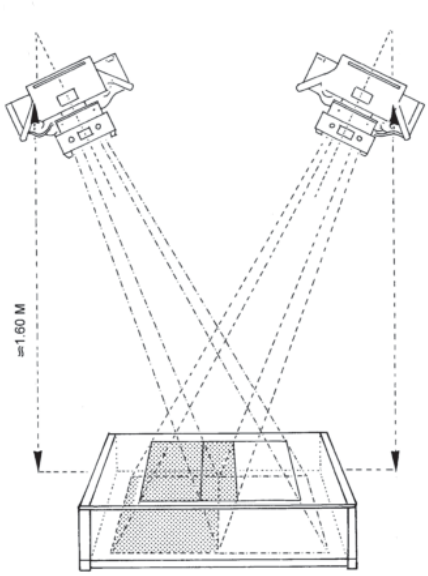

Figure 2.2: Stereoradiography equipment set-up for taking RSA images. The x-ray generator heads at the top of the drawing are angled at 30° from vertical, the participant's anatomy is positioned in the field of both beams, and two images are taken (the two detectors are in the grey-shaded and white sections below the calibration box). Courtesy ISPRS [19]

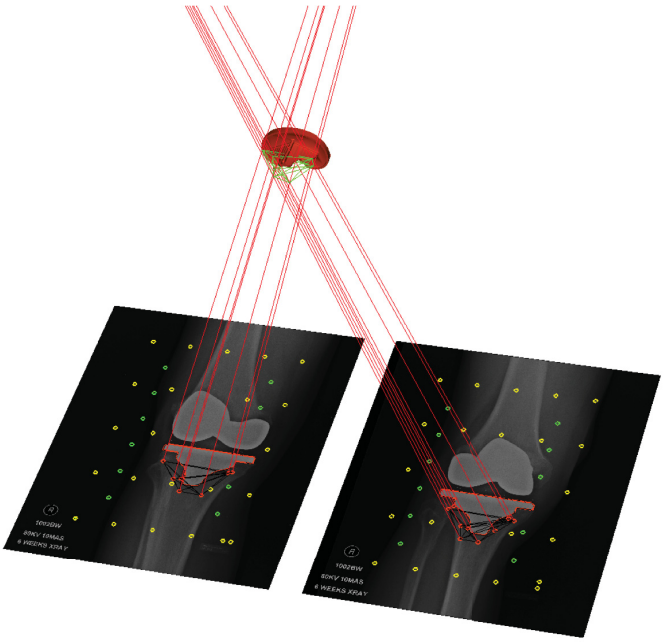

Figure 2.3: Tracing the ray paths backwards from the images allows for a 3D reconstruction of the RSA bead locations.

Migrations are measured via medial-lateral (x), superior-inferior (y), and anterior-posterior (z) translations and anterior tilt, internal rotation, and adduction angles. The maximum any point moves is captured by maximum total point motion (MTPM), which is the most often used RSA parameter in the literature.

2.4.1 RSA Precision

Using markers placed in the implant and bone, double exam analysis has shown the 95% confidence interval range for the repeated measurement RSA translations in the Wright Medical Biofoam study (n=44 double exams) to be 0.14mm to 0.39mm in translation.However, there can be sight line issues with the beads that are injected into the polyethylene insert in the tibial implant, as it is in close proximity to the radiopaque femoral and metal tibial components. Unless three of the same beads are unobscured by implant overlap in exams in question (here the 2 year, 1 year and post-op exams), it is difficult or impossible to determine the migration of the implant. When this happens, the model-based calculation of migration in the MBRSA software is conducted. Instead of matching the rigid body created by the markers in the polyethylene, the software matches a 3D model of the implant itself to the outlines seen in the 2D x-ray images (see Figure 2.4). Our group's double exam testing showed confidence interval ranges similar to marker based migration in translation.

There are three inherent difficulties in assessing the precision of the MTPM measurement. First, it is a magnitude of a vector and thus always positive, so while the other measurements vary around a mean of zero, the average error in MTPM will always be a positive value (bias). Second, the errors are not normally distributed, so finding the standard deviation or confidence interval as a measure of variance is inappropriate. And third, this is a measure of the maximum movement of any one point in the rigid body - if that point were hidden on the next exam, the MTPM value will change. The median MTPM error in the double exams for the Wright Biofoam study is 0.26mm for marker-based analysis, and 0.39mm for model-based, with a range of 0.053 to 1.502mm for the latter.

There are a limited number of study participants with available one and two year data, and further restricting the results to only those with the more accurate marker based migration dropped the available pool by an additional 8% for comparing to

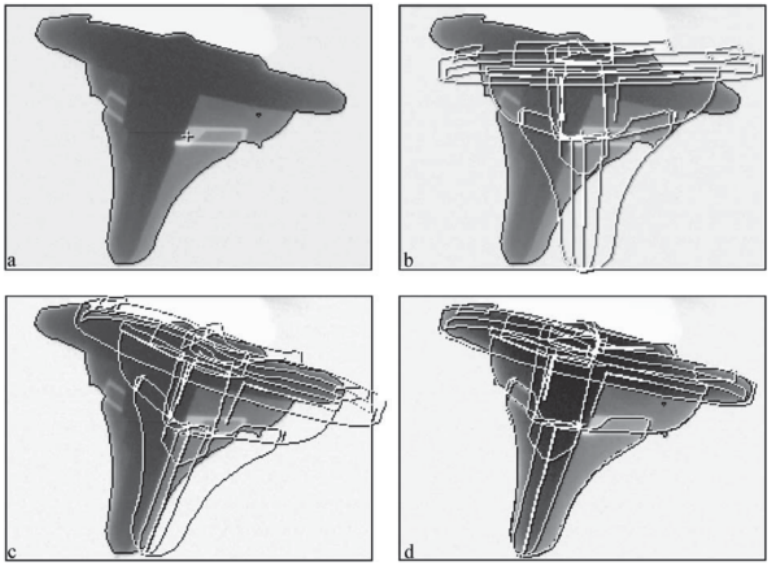

Figure 2.4: Matching the model of the implant (wire frame) to the x-ray image of the implant. [19]

post-operative position, and 32% for two year with one year as reference. In order to keep consistent, all implant migrations were therefore calculated using the model based analysis.

2.5 Bone Mineral Density Scans

Both the Wright Medical Biofoam and Stryker Peri-Apatite study participants had bone mineral density scans of both knees, AP and lateral views. Scans were conducted using a Lunar Prodigy (GE Healthcare, Waukesha, WI) dedicated DXA scanner by a qualified radiation technologist within 1 month pre-operatively and 2 weeks post-op, then at 3 months, 6 months, 12 months and 24 months, using the following protocol.

2.5.1 DXA Protocol

1. The subject was positioned parallel to the lines on the table, with the leg to be scanned straight and the knee cap was straight up. A foam positioner was placed under the knee with the tapered end toward the thigh.

2. The subject's foot was strapped into a vertical position using a foot positioner.
3. The positioning laser was adjusted to 10cm below the patella.
4. Scans were conducted over the knee such that they started and stopped in areas with at least 1-2cm of tissue on each side of the bone.
5. Both right and left knee AP views were scanned, and the resulting image was checked for correct detection of the bone edges.
6. For lateral views of both right and left knees, the subject rotated their whole body in the direction of the knee to be scanned such that the knee lay stable on the table, and flexed the knee to approximately 45° (verified with a goniometer).
7. The laser was positioned in tissue next to the femur on a line parallel to the table line directly above the centre of the knee joint.
8. The final scanned image had the knee centred, the patella completely shown, and bone edges detected appropriately.

The scan data is assessed by our orthopaedics research team using the enCORE software (Lunar Prodigy enCORE 2007, ver. 11.40.004, General Electric Company, Madison, WI) that is packaged with the Lunar Prodigy equipment. Regions of interest were chosen on each side of the stem of the implant and three 1cm deep regions below the implant (see Figures 2.5 and 2.6), and were outlined by hand based on a standard operating procedure outlined below. The enCORE software then calculated the bone mineral density for the region outlined.

2.5.2 DXA Analysis Method

In the enCORE software, the ROI tool was selected from the Analysis toolbar. The ROIs were created in the following order, to ensure consistent numbering.

1. Region 1 in the AP view of the operated side covered the bone area from under the baseplate of the implant to the base of the stem, on the lateral side (see Figure 2.5. The polygon tool was used to outline the bone, with vertices added as needed to avoid the implant and

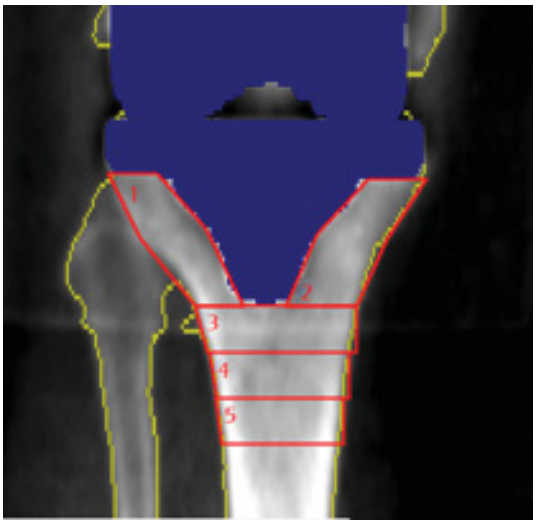

Figure 2.5: Regions of interest on anterior-posterior bone mineral density scans.

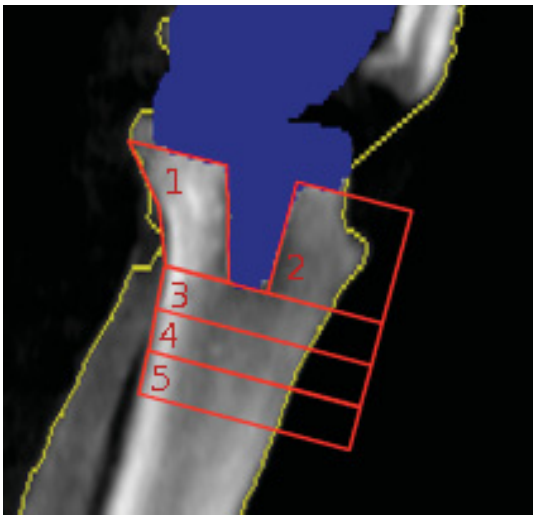

Figure 2.6: Regions of interest on lateral bone mineral density scans.

curve along the edge of the bone. Note that the software ignores everything outside of the yellow bone edge detection line, and the blue implant masked region.

2. Region 2 was created in the same way as region 1 for the medial side of the bone.
3. Region 3 was created by first choosing the rectangular region option, and drawing a rectangle 1cm high (as given by the region statistics on the right panel), and as wide as the bone below the stem of the implant. ROI 3 was placed immediately distal to the stem
4. Region 4 and 5 were created in the same manner as ROI 3, and stacked distally in order (see Figure 2.5).
5. The 'Calculate' option was clicked to obtain bone mineral density for each region.
6. Regions on the lateral view were created in the same manner, with ROI 1 posterior, and ROI 2 anterior of the implant.
7. The region templates were saved and copied to the unoperated side for both AP and lateral views.

The 24 month scan includes a double exam to assess in vivo precision. Two analysts did separate analyses of these scans, and one of our staff calculated the

differences between the two sets of results: 95% of the anterior to posterior (AP) BMD values are within ± 13.7% of the average ROI value in the AP view, and all but one region is within ± 12.6% in the lateral view. This is variation due to ROI placement only, and is much higher than standard precision of hip and spine scans with this equipment (Lunar quotes < 1.0% CV in their technical specifications, whereas we are finding a maximum CV of 6.7%). This is likely due to incomplete masking of the implant (making it possible to capture metal in the region) and lack of precise landmarks for placing edges of the ROIs.

Chapter 3

Bone Texture Project

As discussed earlier, image texture analysis is a recognized means of obtaining information about the microarchitecture of the trabecular bone. The Singh Index for parameterizing the patterns of hip trabeculae is a visual means of obtaining similar information and has been in use since 1970 to assess osteoporosis, although it suffers from interobserver variability [122, 123]. While this type of analysis has been examined quite a bit in relation to fracture risk prediction, and in one instance for distinguishing osteolytic versus healthy bone [38], it has never been used to predict knee implant migration.

First, the set of texture parameters to be analyzed needed to be chosen. Before these parameters could be calculated, standard region size and placement needed to be determined, and image artifacts had to be removed.

3.1 Image Texture Parameters

Of the texture analysis techniques from the literature outlined in section 1.5.3, the statistical methods (e.g. grey level co-occurrence matrices) and Law's masks had too many potential parameters for the small study sizes used here. The Fourier-based fractal method was cautioned against in the literature due to discontinuities at the boundaries of the region, and the binary image techniques were avoided due to the difficulty in setting a "bone-not bone" threshold for each region. Early tests showed variability of the parameter results were an issue with the root-mean-squared of the power spectrum (using the method of Vokes et al., who also found it to have the most variation of all their tested parameters [124]), and the surface-area

fractal method (following Lynch et al. 1991 [48]). Thus four of the techniques from the literature were chosen for full analysis: the first moment of the Fourier power spectrum (FMP), the minimum directional value of same (minFMP), the Minkowski Fractal Dimension, and the wavelet energies from image wavelet decomposition. The Gini coefficient from economics and astrophysics research was added to these chosen texture parameters, as a unique way of examining contrast in the region. More details and methods for calculating each are described below.

3.1.1 Fourier Power Spectrum Parameters

The first moment of the Fourier power spectrum looks at the coarseness/fineness of the trabecular structure, and in that way can distinguish between the thin and closely spaced trabeculae in osteoporotic bone with the wide spaced thick trabecular structure of healthy bone [124]. FMP and minFMP were calculated based on the equations 3.1 and 3.2 from Wilkie et al. and Chinander et al. papers [38, 100], with the minFMP being the minimum directional FMP in equation 3.2 over 15° increments.

$$FMP = \frac{\sum_m \sum_n \sqrt{m^2+n^2}|F_{m,n}|^2}{\sum_m \sum_n |F_{m,n}|^2} \tag{3.1}$$

$$dirFMP(\theta_i \leq arctan\frac{n}{m} < \theta_{i+1}) = \frac{\sum_m \sum_n \sqrt{m^2+n^2}|F_{m,n}|^2}{\sum_m \sum_n |F_{m,n}|^2} \tag{3.2}$$

In these equations, $|F_{m,n}|^2$ is the power of the 2D Fourier spectrum at frequencies m (along the horizontal) and n (along the vertical), and is found using the built-in Matlab (ver. R2008b, MathWorks, Natick,MA) algorithm `fft2` (see Figure 3.1). Vokes et al. also use a similar method, although they calculate $\sqrt{m^2n^2}$ weighted by the power spectrum instead of the weighted mean spatial frequency found with $\sqrt{m^2+n^2}$, which is unique to their group [125, 124].

3.1.2 Fractal Dimension

Pothuaud et al. found a significant relationship between the fractal dimension of a two dimensional bone image and the three dimensional porosity and connectivity of the trabecular bone [126]. The Minkowski Fractal Dimension calculated here was analyzed using the Matlab `imdilate` and `imerode` functions via the same process

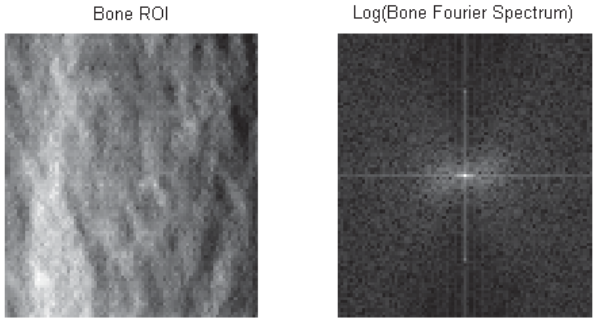

Figure 3.1: Example bone region with its Fourier power spectrum.

as outlined in Wilkie et al. 2008 and others [38, 127, 97], giving a roughness, or complexity, measurement.

$$V_g(r) = \sum_{i=1}^{N}\sum_{j=1}^{N}[(f \oplus rg) - (f \otimes rg)] \tag{3.3}$$

$$MINK_g = \lim_{r->0} \frac{log[V_g(r)/r^3]}{log[1/r]} \tag{3.4}$$

In this method a "volume" difference (V_g) between the dilated and eroded versions of the ROI over a range of structuring element sizes (r, used in the dilation/erosion process) is compared to the scale of the structuring element (see equations 3.3 and 3.4). In essence, this finds the number of pixels along the boundary at different scales. The fractal dimension is derived from the slope of a logarithmic plot of the volume difference V_g/r^3 against $1/r$. $\oplus$ symbolizes the dilation function, and $\otimes$ the erosion function. Smooth boundaries would show a zero slope (the number of pixels at the boundary increases linearly with the dilation/erosion element size), self-similar rough fractal boundaries have a linear slope on the log-log plot. All global fractal dimensions calculated here begin with a 3x3 square structuring element, which is multiplied by the scale values 1 to 10 to cover increasing scales.

In Figure 3.2 the solid line shows the linear fit to all of the volume vs. element

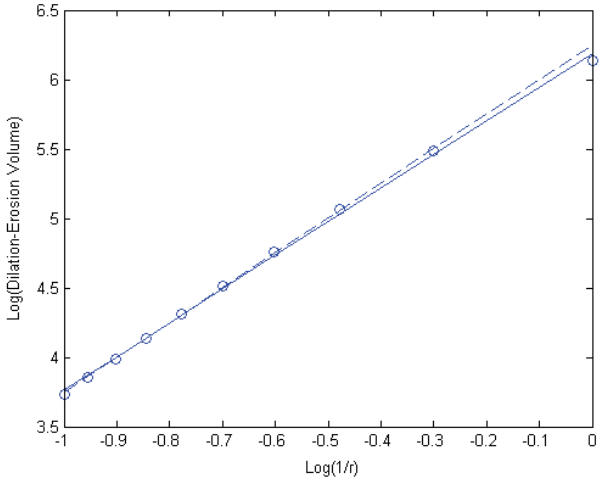

Figure 3.2: Slope of the linear fit to volume vs. structuring element size is the Minkowski Fractal Dimension. The solid line includes all points and the dashed line ignores the most smallest and largest structuring elements, corresponding with the highest and lowest spatial frequency changes.

size points, whereas the dashed line focuses on the most fractal region of the image, bypassing the smallest and largest structuring element sizes where the fractal dimension begins to change. The fractal dimension corresponding to the slope of the dashed line is used in all subsequent analyses.

3.1.3 Wavelet Analysis

According to Faber et al., wavelet transforms had significant differences between normal and osteoporotic bone [106]. The wavelet decomposition is a standard function in the Matlab Imaging Toolbox, more often used for compressing and enhancing images. This method has the advantage over Fourier analysis by keeping both frequency and location information, since it fits finite wavelets instead of global sine and cosine functions, and examines structures at several different scales. Matlab's `wavedec2` function returns the wavelet decomposition of the matrix based on the given wavelet; here the parameters were chosen according to Bharati et al. [93], with the first Coiflet wavelet and a three level decomposition conducted. The `wenergy2` function returned the energy corresponding to the approximation of the image (global) and the energy percentages for the horizontal, vertical, and diagonal details. The global approximation contained overall patterns such as photon intensity variations over the region, and thus acted as a powerful high pass filter when

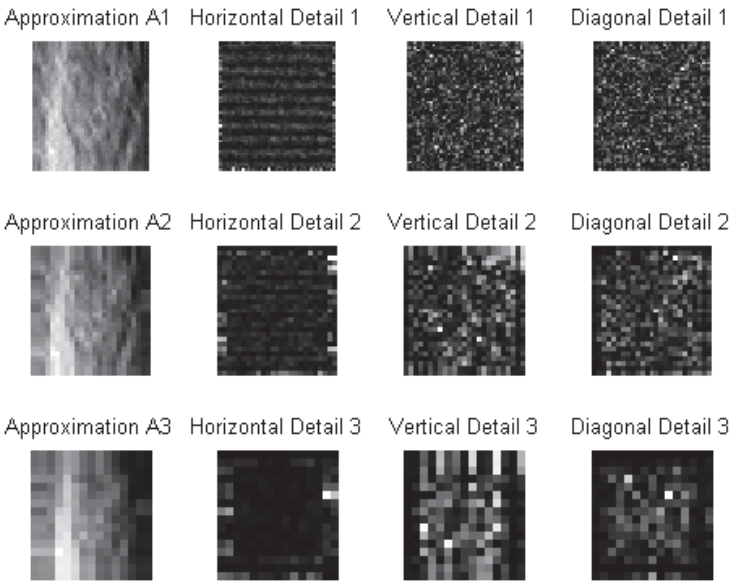

Figure 3.3: Wavelet decomposition of the same bone region as figure 3.1.

this coefficient was ignored [93]. It was the strength of the pattern details where the bone texture measures were sought.

```
[decompVect,matS]=wavedec2(imageROI,3,'coif1');
[Ea,Eh,Ev,Ed]=wenergy2(decompVect,matS);
```

In these Matlab commands, Eh, Ev, and Ed are the energies in the horizontal, vertical, and diagonal wavelet details, and were used in subsequent analyses. The three level decomposition provides three energies for each of Eh, Ev, and Ed. Figure 3.3 shows a graphical depiction of an example wavelet decomposition.

3.1.4 Gini Coefficient

The Gini Coefficient is a summary statistic used in economics to describe the amount of inequality of wealth in a population. Based on the Lorenz curve, which is a straight line with a slope of 1 in an equal distribution and a curve which falls below that for any inequality, the Gini coefficient is a ratio of the area between the Lorentz curve and the line of equality compared to the total area under the line of equity (see Figure 3.4). Thus a totally equal distribution would have a Gini coefficient of 0, and a completely unequal (all the measured value in one location) has a Gini coefficient

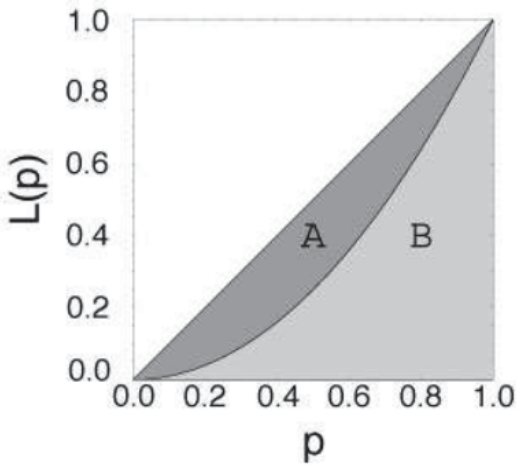

Figure 3.4: Lorentz curve used in economics to show distribution of wealth: equal distribution is a straight line at a 45° angle, any inequality curves below that line. The Gini Coefficient is the ratio of the areas A:A+B, where a value of 1 means all the wealth resides with one person, and a value of 0 is completely equitable.

of 1. This summary of distribution need not be based on money; Abraham et al. [128] used it to define the concentration of light in galaxies to distinguish between spiral and elliptical morphologies (elliptical galaxies have their light concentrated more centrally). In osteoporosis, the trabecular bone appears "washed-out" or low contrast compared to healthy bone; the Gini coefficient may pick out a difference in contrast and be related to bone quality in a similar way as the contrast assessing root mean squared of the power spectrum has been found to be significantly different between a groups of women with (n=42) and without (n=128) vertebral fractures [125]. Equation 3.5 is the basis for the computer-optimized equation 3.6, in which the pixel greyscale values are sorted first, then equation 3.6 is calculated.

$$G = \frac{1}{2\overline{X}n(n-1)} \sum_{i=1}^{n} \sum_{j=1}^{n} |X_i - X_j| \tag{3.5}$$

$$G = \frac{1}{\overline{X}n(n-1)} \sum_{i=1}^{n} (2i - n - 1)X_i (n > 2) \tag{3.6}$$

Both versions are as published by Abraham et al. [128]. X_i and X_j are the individual greyscale values of the pixels, $\overline{X}$ is the average pixel value, and n is the number of pixels.

3.2 Choosing Bone Regions of Interest

The size and placement of regions of interest on the bone needed to be chosen. The greatest area of bone turnover is periarticular, as this is the region most influenced by osteoarthritis pre-operatively as well as stress-shielding post-operatively. Although shown to increase stability, implant stresses are channelled through the stem and may impact bone properties near the tip, and the areas distal to the tibial implant and proximal to the femoral implant ought to reflect the general bone health of the area. Thus six regions of interest (ROIs) were chosen: one on each side of the implant under the tibial tray, one on each side of the stem at the distal end, one below the tibial implant and one above the femoral implant (Figure 3.11 will show an example after the ROI size calculation below).

As it was determined that some of the texture parameters are dependent on the size of the region, the number of pixels in width and height needed to be fixed for each. Set too large, and there is a much greater chance of having the region contaminated by beads, bone overlap with the fibula, or going off the bone completely. Set too small, and spatial information is lost and variability goes up, meaning a slight movement in the ROI placement will produce a relatively large change in parameter value.

3.2.1 ROI Size Test: Methods

To test the effect of size on variability, an unoperated knee x-ray without the calibration box or antiscatter grid was used and three set of ROIs were laid down in a brick-like pattern across the proximal tibia, with sizes 32, 64, and 128 pixels square (Figures 3.5, 3.6, and 3.7). Each region was then moved by 3 pixels in each of the 8 directions to simulate precise human positioning of the region. The variation in the texture parameters over this small local region was compared to the variation over the whole distal tibia as given by the range in all the ROIs. To test the effect of moving the region to avoid an image artifact (such as an implant screw), the range in texture parameters was calculated for three regions together: the upper left 64x64 pixel region combined with the region to the right and below.

3.2.2 ROI Size Test: Results

The box plots in Figure 3.8 show high variability in the 32x32 pixel regions when the position of those regions were changed slightly, with a coefficient of variation as

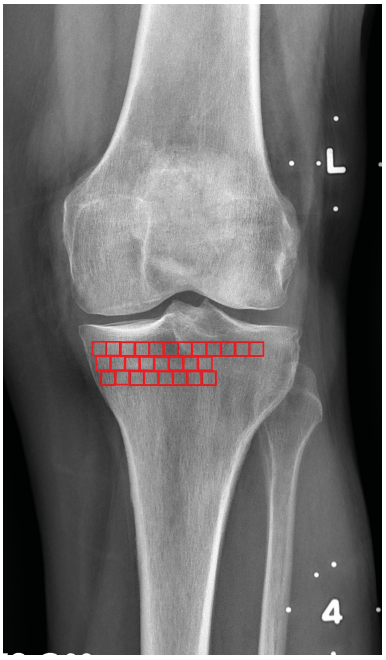

Figure 3.5: 32x32 pixel region locations for variability tests.

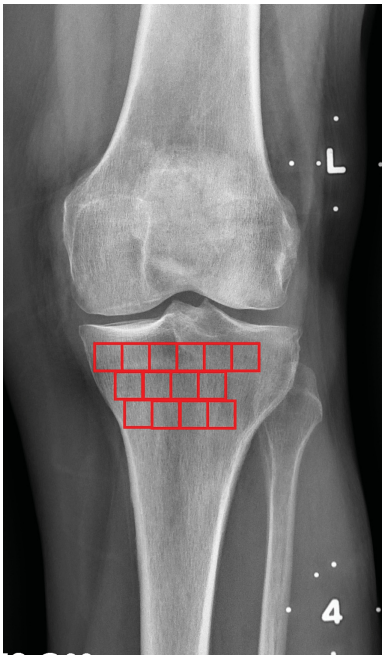

Figure 3.6: 64x64 pixel region locations for variability tests.

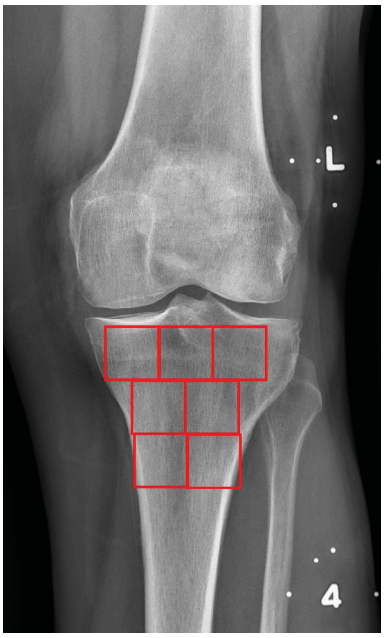

Figure 3.7: 128x128 pixel region locations for variability tests.

much as 45% in the wavelet energies. 64x64 regions have variations up to 23% in diagonal wavelet energy. The 128x128 test ROIs were very stable (fractal dimension coefficients of variation less than 0.25%, and the rest of the parameters less than 14%).

The true danger of parameter variability is swamping the signal between images. This was examined by comparing the distribution of values in the 64x64 test ROIs from placement variability, and the variation from moving the ROI by looking at the range in values in the first two regions of the upper left top row and the first region in the row below, with the values obtained from the radiographs of the study participants in the same periarticular location. Figure 3.9 shows an example of a good range in bone parameter values across the study population (c) vs. the placement and movement variability (a and b), and figure 3.10 shows a texture parameter movement variability which is a considerable percentage of the population range. Plots for the remaining parameters are included in the appendix.

3.2.3 ROI Sizes Selected for Bone Analysis

The algorithms to calculate these parameters require rectangular regions of interest, which are difficult to place on peri-prosthetic bone without overlapping the implant or overreaching the edge of the bone. The high variability in the smallest 32 pixel square regions suggests building up a non-rectangular region or skirting around an obstacle using the combination of small regions is not feasible. 64x64 pixel regions have about half the variability of the small regions, but no region larger than this is able to fit under the tibial tray of an implant while avoiding screws in the Wright Medical Biofoam study. Even with this size, a lot of images still need to be discarded for the periarticular regions. While the 128 pixel square regions were the most stable, only the distal tibia and proximal femur might have room for that size. The algorithms for the parameters examined here require rectangular regions.

Countering the need for reducing variability is capturing the aspects of the bone most likely to reflect a problem that will impact implant stability: large regions have stable parameters because they find a global value over a substantial piece of the anatomy, whereas changes to bone in the few millimetres proximal to the implant can cause implant migration [49].

The minFMP and Gini Coefficient parameters showed high variability over three

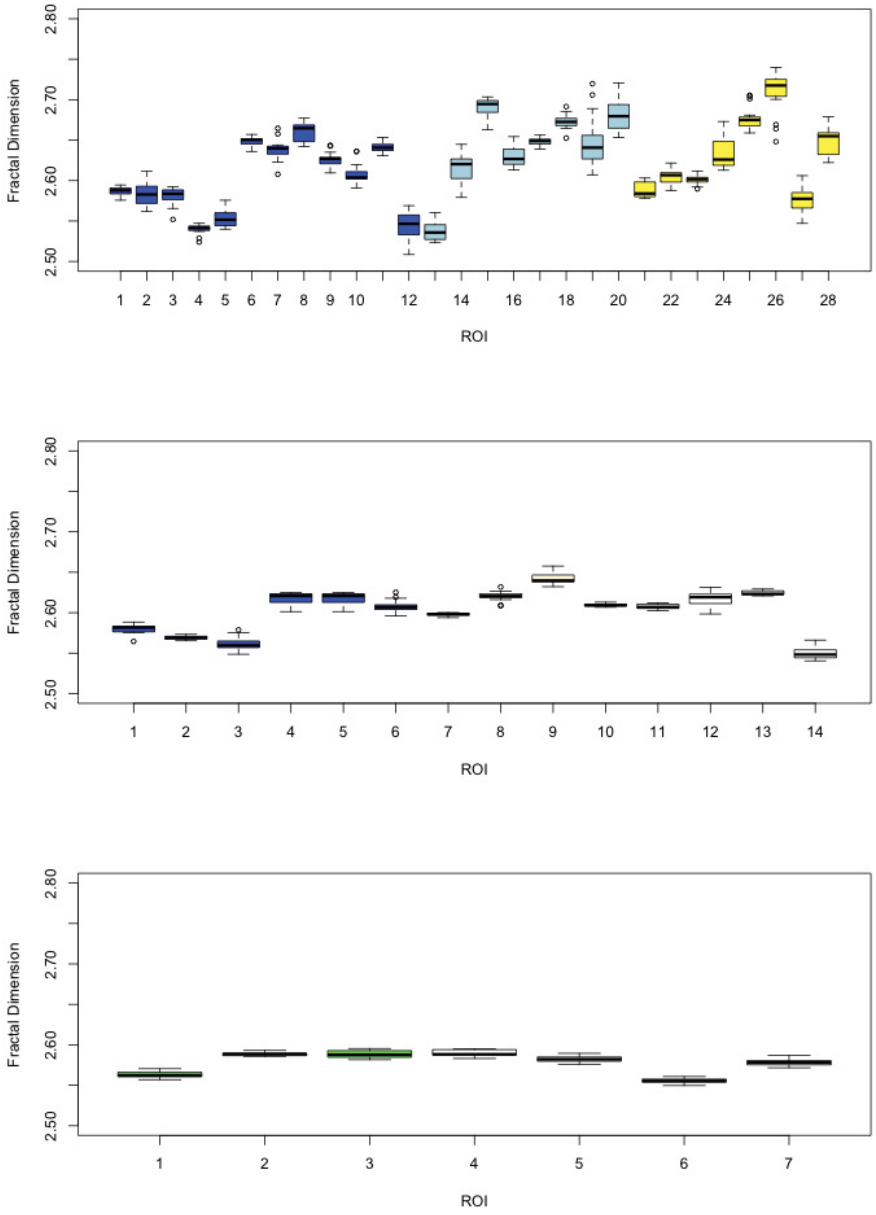

Figure 3.8: Fractal Dimension over test regions. Top plot shows variability for 32x32 pixel regions when position shifted by 3 pixels in each of 8 directions (ROI diagram in Figure 3.5). Middle and bottom plot are the same for 64x64 pixel and 128x128 pixel regions, diagrammed in figures 3.6 and 3.7.

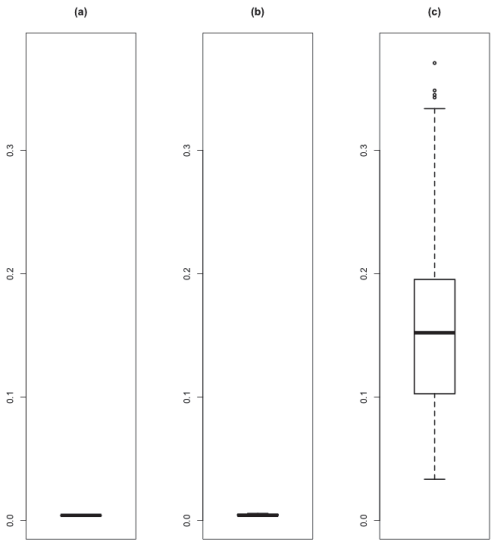

Figure 3.9: Diagonal Wavelet Energy 1. (a) Wavelet energy values for upper left 64x64 ROI when moved ± 3 pixels; (b) Wavelet energy values for (a) plus same for ROI to the right and below to model moving the ROI to avoid contamination; (c) Wavelet energy values for periarticular 64x64 ROIs all 2 year study participants.

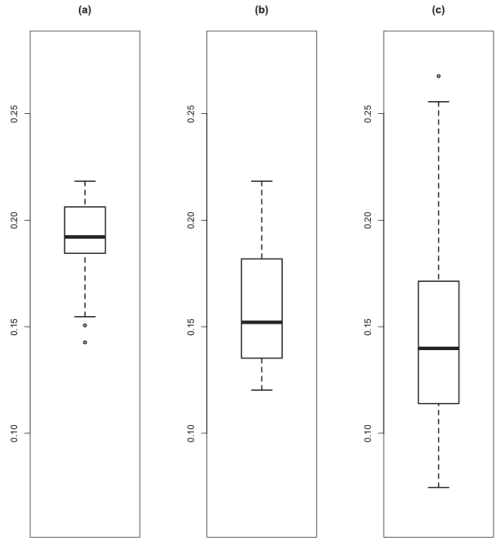

Figure 3.10: Gini Coefficient. (a) Gini values for upper left 64x64 ROI when moved ± 3 pixels; (b) Gini values for (a) plus same for ROI to the right and below to model moving the ROI to avoid contamination; (c) Gini values for periarticular 64x64 ROIs all 2 year study participants.

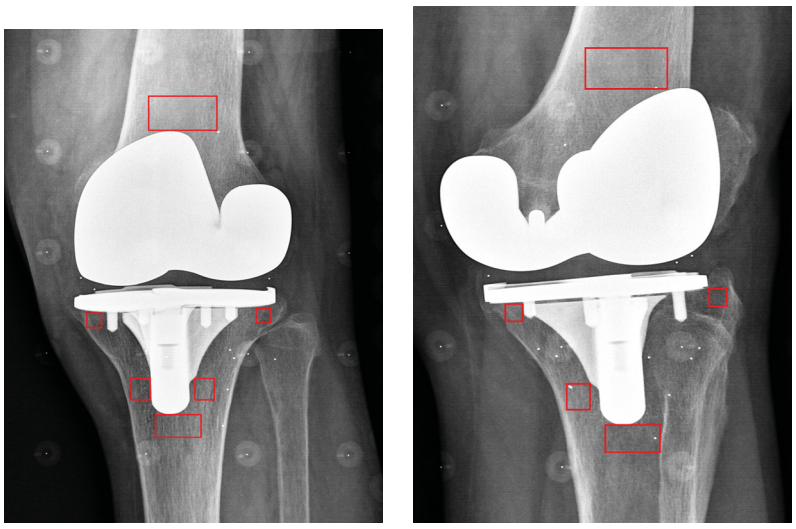

(a) View 1 (b) View 2

Figure 3.11: Region of interest size and placement.

regions on the upper left on the test image compared to the range of values over all subjects in the same area. This suggests that if moved regions are used as part of the statistical analysis, these texture parameters should not be used to try to discriminate between subjects. It is worth noting that the wavelet energies, which had the highest coefficients of variation in the placement tests above, have the lowest range percentage compared to population variability.

Based on a balance between the number of usable images and maximizing the size of the regions, the regions beside the stem were set at 85x95 pixels, the distal tibia set to 200x100 pixels, and the proximal femur to 300x150, along with the 64x64 pixel periarticular regions (see Figure 3.11).

3.3 Artifact Removal

3.3.1 Background Trend Correction

The generated x-ray flux is not uniform over the whole image, which will affect the number of photons received at the detector independent of any absorption or scattering along the way. To assess whether this nonuniformity will affect the calculated texture parameters, images were taken at standard RSA settings with only the calibration box and antiscatter grid in the path before the detectors. The overall background trend was then calculated using the Fit_Polynomial plugin for ImageJ (ver. 1.43u, National Institutes of Health, USA).

A similar fit was made to a typical bone region to test whether the variation over the ROI is due to changes in the photon intensity over the region (which would be seen in the background fit), or due to changes in the bone structure itself.

3.3.2 Background Trend: Results

Figure 3.12 shows the overall background trend, and Figure 3.13 shows that over the region, the background trend variation is less than 10% of the fit to the average bone intensities in the same location. Note that RSA images are automatically rescaled to maximize viewing contrast, which means both the flat field images and bone images are scaled from 0 to 4095. Consequently, the ranges for the background trend are actually higher than would be seen on bone images, which rescale the

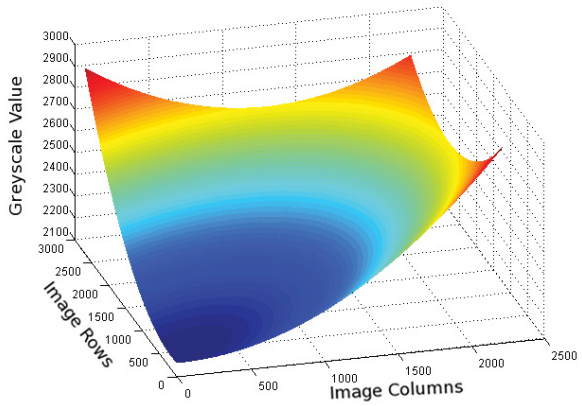

Figure 3.12: Polynomial fit to background only image (=background intensity variation). x- and y-axis are pixels in the original image, z-axis is greyscale value. Note greyscale values in all figures are inverted, low values = low attenuation.

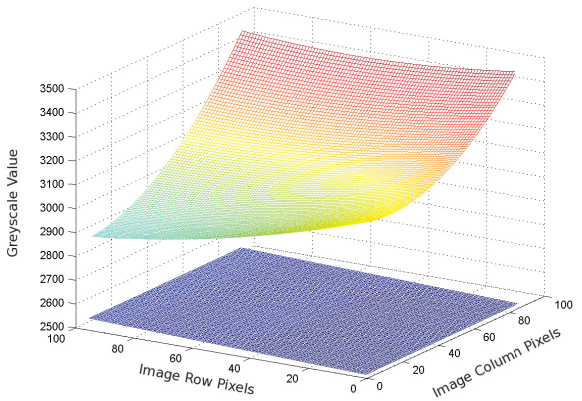

Figure 3.13: Polynomial fit to bone region (=average bone intensity variation), compared to background intensity variation (note: background greyscale values are not adjusted to the smaller range they would be in actual exam images).

background over a smaller range, and the comparison between the two are even more distant. Therefore no background trend subtractions are conducted during the following analyses.

3.3.3 Antiscatter Grid

Photons scattered by the intervening material may still hit the detector, just coming from a different angle than the transmitted photons. Because the atom that caused the interaction is no longer in the direct path between the generator and the detector, these photons add a haze or noise to the final image. The majority of photons reaching the detector have been scattered at least once (80% of photons have been reported to be scattered in 2D imaging [129]). In the SR Suite, to reduce the amount of scattered photons recorded, lead plates are adjusted within the x-ray head to only project x-rays over the necessary area; this columnation of the beam prevents photons from outside the area being scattered back into the relevant portion of the image, as well as reducing dose. On the detector side, an antiscatter grid is used. These preferentially block photons coming in at an angle different than that of the primary beam (Figure 3.14).

The antiscatter grid used for the RSA exams has very small lead septa interspaced with radiolucent fibre at a line rate of 44 cm^{-1} from smit röntgen (Veenpluis, Netherlands), which improves the primary-to-scattered ratio to 6.4. During normal clinical use, these thin strips of lead successfully absorb sharp angled scattered radiation without obstructing the final image. When examining small bone regions which a high resolution detector, however, the individual regions of the bone now have strong horizontal lines which all but obscure the trabecular pattern, as in Figure 3.15.

3.3.4 Antiscatter Grid Removal: Method and Results 1

Since the lines are horizontal, in a visually obvious pattern, two related methods were first tried to remove this interference. In the first case, the average change in brightness from one row to the next was subtracted from the image. A related high spatial frequency filtering via a median and maximum filter tried to remove the fluctuations on a scale of 7 rows.

In some cases, namely small areas with an aligned grid, subtracting the average change worked well. However, the grid lines were not always perfectly horizontal,

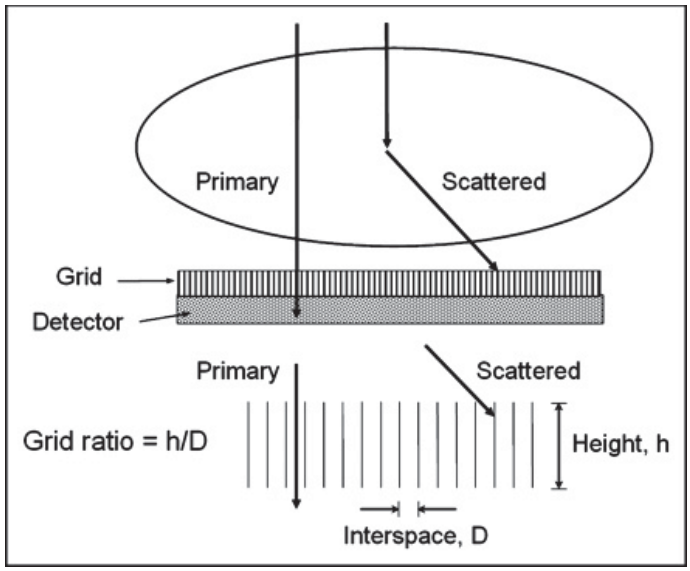

Figure 3.14: Antiscatter grid preferentially absorbs scattered photons. Reprinted by permission of the Society of Nuclear Medicine from [130] (Figure 10).

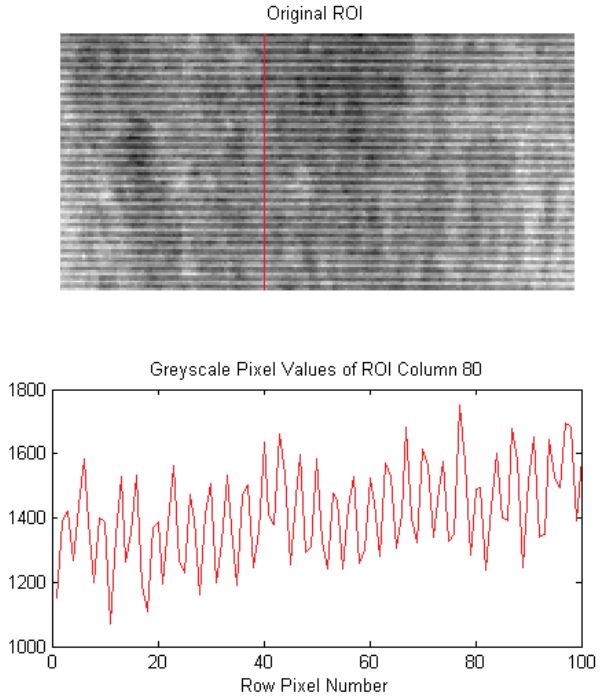

Figure 3.15: Horizontal antiscatter grid lines on example region of interest.

especially over larger scales. When a lead septum in the antiscatter grid crosses rows of pixels, a deep absorption occurs over a group of pixels in the first row, followed by a lesser absorption amount distributed over two rows, then the peak absorption completely moves into a new row. This makes using a relative brightness model impractical. Extending the filter over a larger number of rows introduced artifacts, affecting the underlying bone texture.

3.3.5 Antiscatter Grid Removal: Method and Results 2

The next attempt read the background image (with only the calibration box and grid, mentioned earlier in section 3.3.1) into a Matlab matrix, and subtracted it from the subject exam image matrix, with the intent of subtracting off not only the grid, but also the calibration box artifacts such as the control bead halos which are also superimposed on the bone.

Unfortunately two issues proved this also unworkable: (1) the antiscatter grid is slid into a slot in the calibration box without fixation, and any small movement of the box means the exact pixels that are shadowed by the grid lines change, and (2) the Canon software automatically adjusts the greyscale values of the image to optimize it for viewing in the saved clinical exams. The latter means that a complicated, and unknown, polynomial scaling of pixel intensities is needed to match the brightnesses of the control beads or the antiscatter grid lines between background and clinical images.

3.3.6 Antiscatter Grid Removal: Method and Results 3

One of the textural analysis parameters, wavelet energy decomposition, breaks the image region into horizontal, vertical, and diagonal patterns. This decomposition was conducted, the horizontal energy was suppressed to 20%, 10%, and 1% of original, and the image was reconstructed using Matlab's `waverec2` function (see code in Section B.1). A test of this method of removal was conducted using a region on a bone x-ray image without an antiscatter grid in place. Texture analysis was completed using the methods outlined in section 3.1, then antiscatter grid lines were virtually overlaid on the region by adding the line brightness changes from one of the RSA exams to the bone ROI matrix. The virtual antiscatter grid was removed

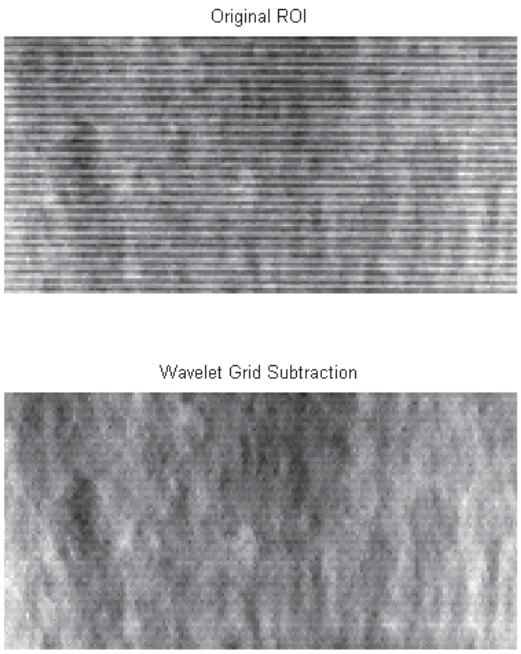

Figure 3.16: Antiscatter grid lines removed.

by suppressing the horizontal energy to 10% as outlined above, and the bone texture parameters were recalculated on the newly cleaned image and compared to the original values.

In the reconstructed image, the horizontal lines are effectively suppressed, as seen in figure 3.16. Comparing the original no grid texture parameter values with the grid subtracted version (using the 10% horizontal energy version) found the results to be within 1% of the original for the fractal dimension, and within 8% for the other texture parameters aside from the Gini coefficient which was 12% lower than baseline. Of the different levels of horizontal energy reduction were tested, the suppression to 20% was too little and the grid lines remained visible, and 1% of the original horizontal wavelet energies was too much suppression and caused bone texture to be blurred (Figure 3.17). All regions used in the following texture analysis have had the horizontal wavelet energies reduced to 10% to remove the effect of the antiscatter grid lines. Because of this, the horizontal energies were not used as texture parameters themselves when comparing to implant migration.

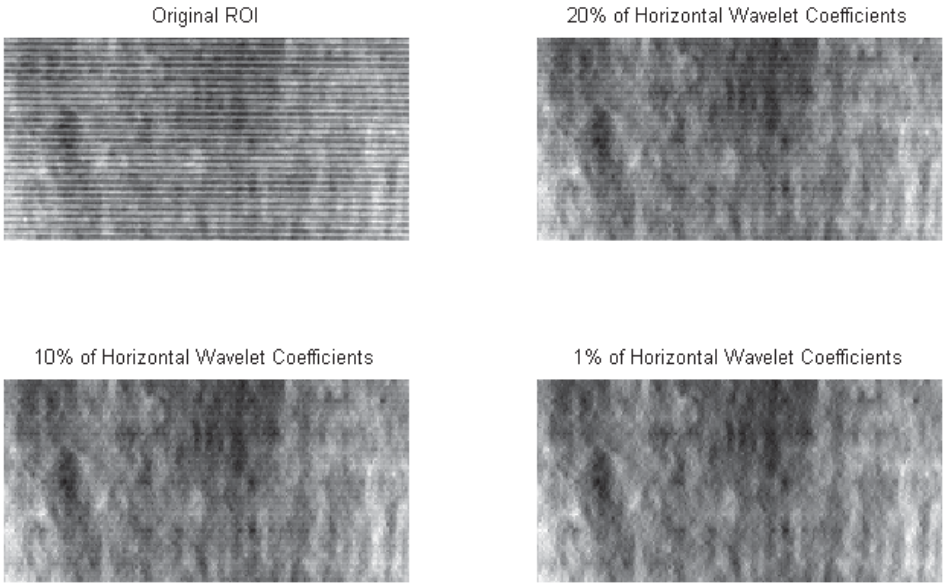

Figure 3.17: Antiscatter grid removal test: horizontal pattern levels at 20%, 10%, and 1%.

3.3.7 Tantalum Marker Bead Removal: Methods

The tantalum beads inserted into the bone have a high x-ray attenuation coefficient, which makes them easy to detect on the x-rays, both by human eyes and computers. They do, however, affect the results of texture parameter analysis, as they interrupt the patterns of the trabecular bone. Tests were conducted to assess removing them from the regions of interest.

A threshold was set to isolate the brightest 150 pixels in a given region, then only those who are grouped together were kept. By requiring 35 contiguous pixels, isolated bone density peaks in the trabecular structure were ignored. These chosen regions were then dilated to grab the dimmer rim(s) of one or more markers. Once the marker has been subtracted from the image, a prediction of what the bone would have looked like underneath the marker has to be added back in or the texture analysis will produce erroneous results. A statistical-based texture inpainting algorithm [131] searches the unmasked background and finds the pattern most likely to match the edges of the affected area and works inward to recreate the masked region. Figure 3.18 shows the progression of marker masking, inpainting, and grid

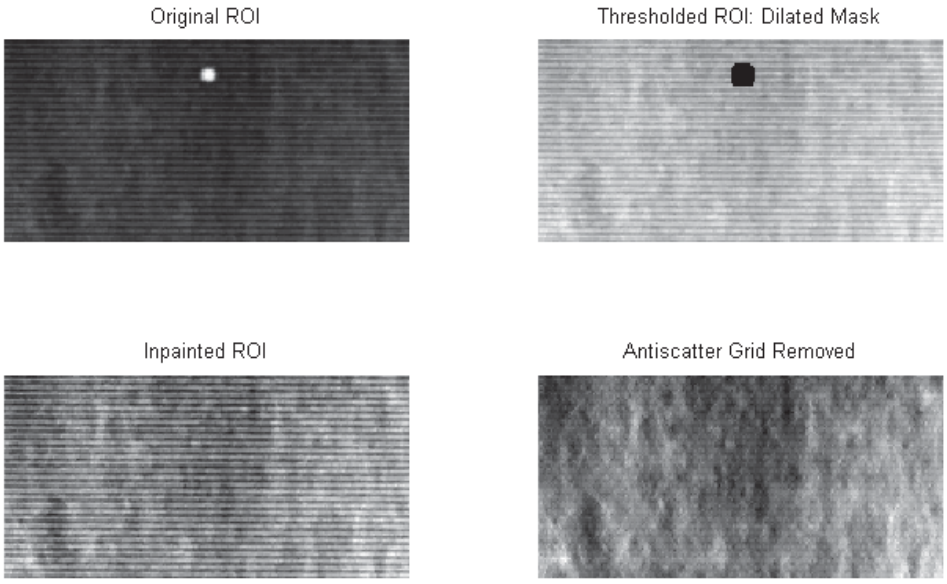

Figure 3.18: Region with bone marker: bone marker masked, masked area inpainted, and grid removed.

removal.

3.3.8 Tantalum Bead Removal: Results

The human brain is very good at assessing pattern, and will immediately pick up when something is off: in none of the bone areas with inpainted markers were the original locations of the markers visually distinguishable. A computational check using the same technique as with the antiscatter grid was conducted for verification, and the change in the parameters when a marker was added, masked, and inpainted was less than 1% of the baseline for all parameters.

The order of operations has been tested: attempting to clean off the grid before removing the beads distorts the bead enough (see Figure 3.19) to cause the above masking technique to incompletely cover the new bead area and the resulting cleaned image contains artifacts. It is possible that adjusting the masking technique would account for this variation, but since the marker-then-grid technique works well, it was not pursued further.

This same technique proved equally able to handle the ends of staples or screw tips, but is limited in the area that can be masked. Unfortunately this technique

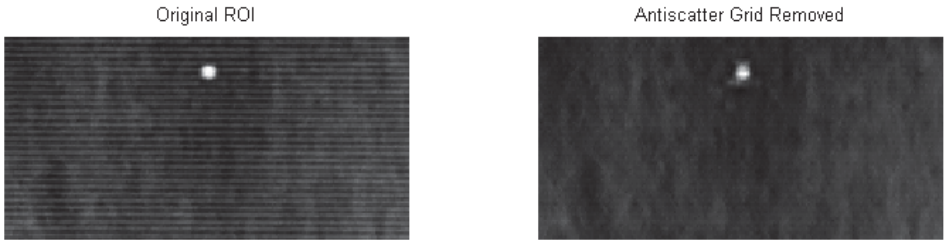

Figure 3.19: Antiscatter grid lines removed before marker: distortions of marker shape make identification of the marker area more difficult.

proved unfeasible for removing the tantalum bead markers in the calibration box, as these beads have a washer surrounding them which casts a halo on the image. The main problem is the large extent these halos cover. The inpainting program needs a considerable background-to-masked area ratio to successfully fill in the missing pieces: masking a halo or a section of implant on the chosen scale of the bone regions of interest for this project created obviously incorrect texture inpainting.

3.4 Algorithm for Determining Microarchitecture Parameters

A Matlab program was written which read in the radiograph, and displayed the image on a graphical user interface. Rectangular regions of interest pre-sized to the number of pixels chosen in section 3.2.3 were presented for placement on the first image, and these positions were saved. By registering each image to this baseline image using the Matlab function `dftregistration`, an initial guess for each ROI position was made, and each region was then shown on the GUI interface in turn for adjustment and acceptance.

The optimal region positions were determined based on Wright Medical Biofoam implant landmarks (Figure 3.11). The Stryker Peri-Apatite implant has flanges in approximately the same position as the Biofoam version, although the Biofoam implant has a central stem that continues more distally than the end of the former. To keep the same region of bone analyzed, the beside-the-stem regions were centred

vertically at the end of the PA implant, and the distal tibia ROI was placed approximately 100 pixels (one ROI height) below the implant, which roughly corresponds to the base of the Biofoam implant. The Stryker Triathlon implant is the cemented version of the Stryker Peri-Apatite design, and the same ROI placements were used. However, since these implants were cemented, the ROIs were shifted a millimetre or two away from the edge of the implant to not capture radiopaque cement in the analysis. Any visible cement was avoided, and additional ROI movement was noted if it was necessary.

If the regions placed above were accepted as viable, any bone markers or staple edges in the region were removed as well as the horizontal lines from the antiscatter grid. A maximum of three bone markers can be consistently removed with the masking algorithm described in section 3.3.7; usually all that was required was a minor shift of the region to keep the number of bone markers within this range. A change in the threshold for choosing the bright pixels would allow more populated regions, if it were required. The region pixel values, in a matrix, were then sent to sub-functions for the calculation of the first moment of the power spectrum (FMP), minimum directional FMP, fractal dimension, wavelet decomposition, and Gini coefficient, using the equations described in section 3.1.

The texture of all available images was analyzed. If an artifact required moving the region, up to approximately the size of the small region (64 pixels) was allowed in each direction for the peri-implant regions, and the height of the distal tibia or proximal femur region in the vertical direction for those regions. If the obscuration could not be skirted within that window, or the region extended past the edge of the bone, the region was rejected. All results were output to a comma separated value file readable by spreadsheet and statistical software packages.

3.5 Bone Parameter Results and Statistical Analysis

About 15% of accepted regions were moved away from the optimal location, and all moved regions were noted.

A table of all regions and texture parameters for each region was then sorted by study participant and stereoscopic image view (1 & 2). In order to keep as complete a set of input variables as possible, the regions that were moved were kept, thus two

of the total 10 texture parameters (minFMP and Gini coefficient) were discarded as they are highly variable on an individual local scale compared to the range across all study participants. The remaining 8 texture parameters (FMP, fractal dimension, and 6 wavelet energies) for each of the 11 regions over the two views adds up to a total of 88 parameters. This presented a problem, as this is more than the number of participants in either study group.

The intention of this analysis is to predict migration classification using measures of bone quality, which requires statistical models with supervised learning. From initial examination of the data, it was seen that these parameters do not have an obvious relationship with the migration outcomes, and linear regression did not prove a useful technique. Breiman argues that model-based statistics have several shortcomings, including difficulty in accurately determining the goodness-of-fit, especially when using nonlinear combinations of variables [132]. He found that although variable relationships were more difficult to interpret, algorithm-based statistics were more accurate in predicting outcomes.

An adaptive technique, decision trees recursively split the data space, choosing an input variable and cut-point for that variable to divide the results into two groups, separating the average outcome for each group as much as possible. Each subgroup is then subdivided based on whichever input parameter best separates that data into clearer outcomes. In the case of classification trees, new data can be entered into the top (root) of the tree, travel down the branches based on how the observed parameters compare to the node splits, and reach a terminal leaf which classifies the observations to which outcome is most probable based on the fitted model (Figure 3.20). Classification trees do not *a priori* define a model for the fit and can include multiple splits on the same variable allowing for nonlinear and even nonmonotone relationships to be modelled [133].

Any individual statistical model has its drawbacks, and classification trees are no exception. The very flexibility of the modelling makes it quite easy to overfit the training data, creating a model that perfectly fits the sample, but is therefore likely to have higher errors when applied to another sample (high variance). Ensemble techniques ameliorate the drawbacks of individual models by creating a collection. While trees have high variance, they have low bias, and by averaging an ensemble

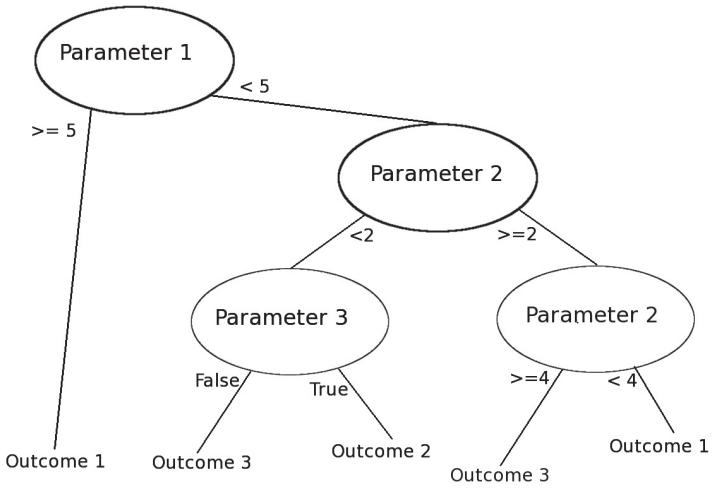

Figure 3.20: An example of a decision tree.

of trees, the variance is reduced. The most accurate results occur when the trees are diverse.[134]

Random Forest™ models [135] are an ensemble of decision trees, with a two-step method to increase diversity in the individual trees. The first step is bagging (bootstrap aggregating), where subsets of the original data are drawn randomly with replacement. Two-thirds of the data are used to train the model, and one-third is held in reserve to give an out of bag (OOB) error estimate. The second step is in the creation of the nodes of the decision tree: instead of finding the best input variable out of the whole set to provide the split, a random sample (m) of the input variables is available for comparison. For classification trees, a suggested one-third of the input variables are examined at each node, although in most cases the fit is robust to the size of m. Each choice in the creation of these models is now based on a random subset of data and of input variables. This reduces the correlation between trees, which can hamper efforts to reduce variance. The achieved reduction in variance means, effectively, that overfitting is seldom seen with Random Forest™ classification [134].

Because of the use of variable subsets, Random Forest™ models have been used extensively in overparameterized systems (the so-called “small n, large p” problem) [133]. The built-in error checking (both the OOB for the individual trees, and a

final cross-validation error estimate for the whole forest by averaging all the trees corresponding to samples that do not include each variable in turn) means small datasets do not need to be split into training and validation sets. As Breiman points out, the more predictor variables available, the more potential information, and that connections may be found in combinations of these variables; which may be why his research found Random Forest™ analysis to be more accurate in prediction than data modelling [132].

The forest can also be used to filter the input variable set to determine the most important predictors. There is a package available ("Boruta") in the R statistical program (R version 2.12.2, The R Foundation for Statistical Computing) which uses this ability of Random Forests™ to determine which parameters have an impact on the final classification: it doubles the input variables, permuting the second set. If the classification result is better with the true parameter than the permuted one (within a set limit), it is important.

In order to determine links between input variables and outcome classifications, Random Forest™ analysis requires a complete data set. For this study many individual regions of interest were rejected for contamination, thus if only those images with all regions accepted are kept, the study population would be reduced to less than five. Region subsets were therefore created to maximize the number of participants within each group, but to also allow for the possibility that a combination of regions would give a better model than each alone.

The Boruta package was run on each region subset (usually around 36 input variables), and the important or tentatively important variables extracted (usually 1-5 variables were deemed potentially important). Those few important variables were put through the Random Forest™ analysis, which creates a predictive model which minimizes the out-of-bag classification error rate.

Receiver operating characteristic (ROC) curves are a standard graphical representation of sensitivity (true positive rate) versus 1-specificity (false positive rate) of a test. When different cut-points of the input model are used, there are trade offs between sensitivity and specificity: in order to catch all of the positive outcomes, more negative ones will be incorrectly labelled positive, and vice versa. This gives a characteristic bow shape to the ROC curve, where the point on the curve closest

to the upper left corner (100% true positive rate, 0% false positive rate) is the one with the lowest total classification error. In this study, the forest model already determines the fit with the lowest OOB classification error, so in essence it chooses that point of the curve closest to (1,0).

3.5.1 Migration Output Classification

As was mentioned in the introduction, RSA measured migration within the first few years has been shown to be a predictor of risk for aseptic loosening, the most common cause of implant failure. The most referenced research on this link is by Ryd et al. in 1995 [20], who found that 81% of a pool of 131 cemented and uncemented implants with a change of magnitude of the migration vector (MTPM) between one and two years greater than 0.2mm would go on to further loosening (defined as more than 0.2mm in any 2 year time frame, although often seen as a continual migration over time). They quote an accuracy of 0.2mm for their RSA technique, which used film-digitized images assessed with computational rigid body kinematics. Of 14 revision cases, 12 would have been identified at 2 years using a combination of change in MTPM from one to two years and the absolute migration value at two years, although no mention is made of how many of the unrevised implants were also flagged using these criteria.

There is a dearth of long-term follow-up studies of knee arthroplasty with RSA analysis [136]. Pijls et al. in 2012 [137] showed the results of their study comparing hydroxyapatite coated (n=24) implants to non-coated (n=20) and cemented (n=24) versions at 11-16 years. Before 10 years they had three cases of aseptic loosening, one had early continual migration (5.92mm over the first 3 years), one had high initial migration that appeared to stabilize, and one was stable then developed late-term osteolysis, which was seen by an increase in implant migration around 7 years post-op. They had 3 cases of continual migration after 10 years, but only one of those is the study participant still living and considered at risk for aseptic loosening. With these small numbers of aseptic failures, it isn't possible to prove whether the 0.2mm cut point between one and two years is a good indicator of aseptic loosening for their study.

In order to retain as many data points as possible, the analysis for this work is based on model-based RSA calculations of migration (see section 2.4). The median

2 year MTPM for the Wright Medical Biofoam study increases from 0.81mm to 1.16mm when using model-based versus marker based analysis for the same study participants; the Stryker Peri-Apatite median increases from 0.60mm to 0.82mm. CAD models of the implants were used to fit the implant position, which have been shown *in vitro* to be less accurate than both marker based and scanning the actual implant used [138].

Maximum total point motion (MTPM) is a vector, although only the magnitude is calculated. To find the true change in MTPM, the RSA analysis must use the earlier image as the reference for the migration of the later image (e.g. 1-2 year change in MTPM must use the 1 year images as the reference). Only Pijls et al. [137] specifically state they recalculated change in MTPM in this way. On the other hand, the direction of the MTPM vector may not be clinically relevant, as bone resorption allowing for an anterior-posterior tilt range of motion for example may show up as tilted on one side in one set of images and the other on the next, with similar absolute MTPM magnitudes: the fact that the vector moved over that space may or may not be important. Both methods are calculated here, the vector-based MTPM calculation gives larger changes, as expected. Subtracting the vector magnitudes, 22% of the uncemented study participants have a change in MTPM larger than 0.2mm, which is similar to the Ryd study who had 31% classified at risk at that time with a combination of implant fixation types. Using the 1 year exam as reference and finding the full vector change, however, has 87% of implants with greater than 0.2mm migration; the cut-point would have to be set to 0.6mm to have a similar at risk percentage.

Due to the use of both vector and magnitude subtracted MTPM and the use of the less precise model-based RSA migration values, a number of different cut-points have been used to divide the results, and models created for each to see whether the bone quality parameters can be used to correctly identify the participants in each group. These results can then be used at a later date when longer-term results clearly identify those implants who are continuous migrators or develop aseptic loosening, to see if these bone models could have predicted outcomes.

3.6 Migration Classification Results

3.6.1 Change in Maximum Total Point Motion Between One and Two Years

Of all the regions of interest, two were continually found important in Random Forest™ models which best minimized the out-of-bag classification error for change in MTPM: the distal tibial region in the one view of the double exam image and the beside-the-stem regions in the second radiograph (the image in which the fibula is overlapped with the tibia).

A subset of data using only these two regions was created, and any images that did not have acceptably unobstructed bone for both regions were discarded. As regions that needed to be moved slightly to avoid obstructions were kept, only FMP, fractal dimension, and vertical and diagonal wavelet energies (three each) were used as descriptive variables. Both magnitude-subtracted and one-year reference change in MTPM was used as the outcome, with binary groups created using cut points of 0, 0.1, 0.2, and 0.3mm for magnitude-subtracted MTPM ($\Delta MTPM_{mag}$) and 0.2mm to 0.7mm at 0.1mm intervals for one-year reference MTPM ($\Delta MTPM_{1yrRef}$). The cut points were chosen such that there are at least 6 implants in the smaller group. Small numbers in a group make it difficult to train the Random Forest™ model, and lead to a lack of robustness: flipping the classification of one implant can change the sensitivity or specificity by a large fraction.

The Boruta package was run to find the important descriptive variables for each classification. For $\Delta MTPM_{1yrRef}$, models based on one parameter (the second diagonal wavelet energy in the region beside the stem) proved the most discriminative for three out of the six cut-points, and provided similar results for two more. Adding a second variable to the model (the first diagonal wavelet energy in the same region) did increase both sensitivity and specificity for classifying implants with more or less than 0.6mm of motion in the second year (75% sensitivity, 100% specificity). True positive and false positive rates for the single-variable model for all cut-points are given in Table 3.1. A graphical representation of the same data is given in Figure 3.21, in a manner similar to an ROC curve (see section 3.5). Instead of varying the cuts on an input model, the lowest error results, as chosen by forest model, are plotted for each of six outcome classification cut-points. Thus Figure 3.21 is in fact

Table 3.1: Sensitivity and (1-Specificity) of Random Forest™ models classifying change in MTPM at 2 years with 1 year as reference.

Cut-Point	0.2mm	0.3mm	0.4mm	0.5mm	0.6mm	0.7mm
True Positive Rate	0.94	0.875	0.6	0.64	0.625	0.17
False Positive Rate	0.5	0.2	0.21	0.11	0.06	0.12

the equivalent of stacking six ROC curves on the same graph (one for each output classification scheme), but only retaining the best point on each curve.

The same method was applied to the $\Delta MTPM_{mag}$ results. Here both the distal tibia and proximal to the stem ROIs were important in the optimal models. Using the FMP of the proximal stem region and the a vertical wavelet energy from the distal tibia region, the most sensitive and specific models to distinguish change in migration based on a 0mm (68% sensitivity, 50% specificity) and 0.1mm (50% sensitivity, 93% specificity) cut-points was found. Taking the proximal stem parameter individually however created more sensitive models for both the 0.2mm (40% sensitivity, 85% specificity) and 0.3mm (57% sensitivity, 89% specificity) cut-points. None of these models were as able to distinguish true classifications in $\Delta MTPM_{mag}$ as the models based on $\Delta MTPM_{1yrRef}$.

3.6.2 Change in Subsidence Between 1 and 2 Years

Total point motion is the most referenced RSA indicator of implant stability in the literature, but its clinical significance is unclear. Historically, measures of subsidence and liftoff (negative and positive motion along the y-axis), and varus angle were most assessed. Li & Nilsson found a non-linear relationship between bone mineral density and subsidence and lift-off, where participants with both low and high BMD had more migration than those with average values [85].

Tests conducted assessing the ability of these bone architecture and bone mineral parameters to explain variability in x and z direction migrations found no significant links. A diagonal wavelet model based on the distal tibial region had a sensitivity of 90% and a specificity of 70% when classifying groups based on lift-off versus subsidence (cut-point of 0mm in the y direction). A three parameter model using vertical and diagonal wavelet energies of the same proximal stem region that was found to be helpful in classifying MTPM changes above was overall the best at classifying migration based on subsidence cut-points of -0.05mm (78% sensitivity,

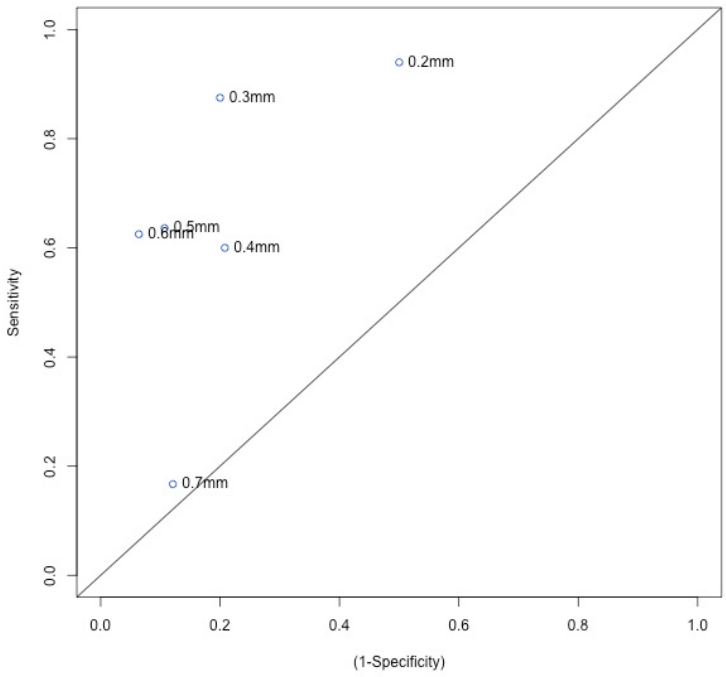

Figure 3.21: Ability of Random Forest™ models based on the diagonal wavelet energy in the stem proximal ROI to correctly identify implant migration based on a number of cut-points. Each point represents the minimized out-of-bag classification error, and thus the best result of a standard ROC curve.

71% specificity) and -0.1mm (44% sensitivity, 83% specificity).

3.6.3 Predicting Future Migration

While adding bone quality assessment tools to existing RSA setups may prove to be beneficial, an even more valuable aspect of these analyses is the possibility that an x-ray exam pre-surgery could assess risk of future implant instability.

A preliminary study testing the predictive feasibility these parameters used the immediately post-operative (as a proxy for pre-operative) and 1 year exams of 18 cemented knee replacement study participants. As this study only began in the fall of 2010, further study data is not yet available. As has been discussed, contamination of bone regions or areas too small to completely fill the designated ROIs necessitate making smaller subsets of data to have a complete set of descriptive variables. In this study, the smallest subset had 13 subjects, and the ability to categorize based on change in MTPM from post-operative to one year was assessed using the bone quality parameters calculated from the post-operative images. Figure 3.22 shows the sensitivity and specificity of a model based on the vertical wavelet energy in a periarticular region. This model found a sensitivity of 75% and a specificity of 80% when predicting those study participants who went on to more or less than 0.4mm total migration by one year.

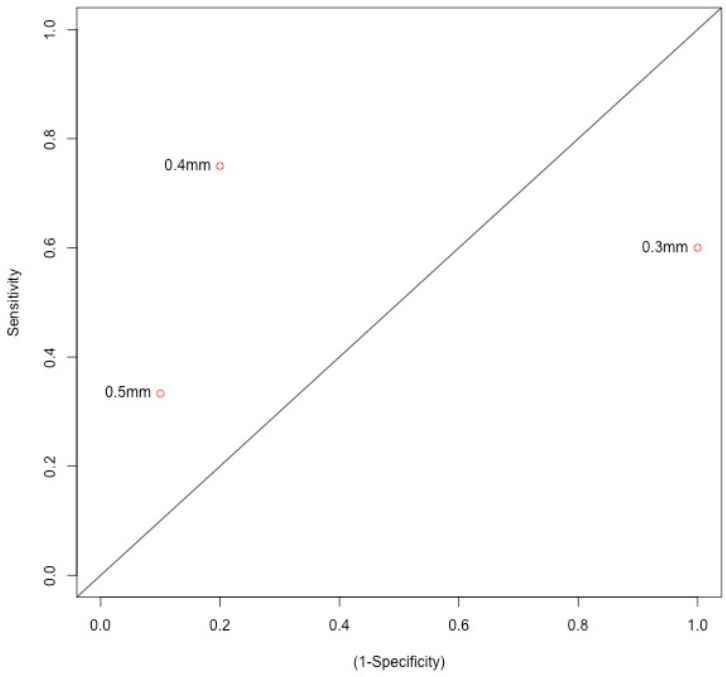

Figure 3.22: Ability of Random Forest™ models based on vertical wavelet energy in a periarticular ROI at the post-op exam to correctly identify 1 year total migration of a cemented implant based on a number of cut-points.

Chapter 4

2D Dual-Energy X-ray Absorptiometry Project

4.1 Overview

The current gold-standard measure of "bone quality" is bone mineral density as determined using dual-energy x-ray absorptiometry (see Section 1.5.1). This project examines the case for, and technical requirements of, adding bone mineral density assessment to the current Stereoradiography (SR) Suite at the Halifax Infirmary.

Current dedicated scanning equipment sacrifices spatial resolution for reduced dose levels; the Lunar Prodigy system (GE Healthcare, Waukesha, WI) has a resolution less than 0.5 line pairs/mm (less than 1 pixel per mm) [139], whereas the Canon CXDI-55C digital detectors in the SR Suite (Canon USA Healthcare Technologies, Rockville MD) have 3.1 line pairs/mm. For a general bone health parameter, the lower spatial resolution likely is not an issue, but this same systemic bone mineral density status has not been implicated in long-term implant loosening [27, 58, 54, 79, 88]. However, local changes in bone mineral levels surrounding the implant could theoretically be linked to local mechanical strength and affect fatigue failure of the bone, and thus the lack of spatial resolution in current systems may be masking real bone mineral density changes associated with implant migration [34].

Along with accessing greater spatial resolution, using the Stereoradiography Suite x-ray equipment to obtain BMD will also allow all the x-ray based bone quality parameters to be gathered at the same time, with the same equipment, and may reduce the number of exposures needed for each patient, if images taken for one type of analysis could be used for others.

This project is based on a similar work by Gulam et al., which validated obtaining BMD of the phalanges from dual-energy images using standard 2D x-ray equipment [75]. The intent of this project is to show proof-of-concept for cone-beam DXA analysis of the knee, by assessing the ability to empirically calibrate an algorithm linking high and low energy image intensities to the known material thicknesses of an x-ray phantom designed during this project, and by testing the ability of the equipment to hold a calibration over a day or more.

4.2 X-ray Phantom Design

Since the x-ray generators produce polyenergetic beams, the single-energy exponential equations 1.2 and 1.3 are no longer directly solvable. As the x-ray beam passes through the anatomy, lower energy photons are preferentially attenuated, the average beam energy is shifted higher ("beam hardened"), and the logarithm of the beam intensity now has a non-linear relationship with the absorber thickness [140]. One method to overcome this challenge is an empirical fit between the known material thicknesses of a calibration phantom, and the resulting high and low energy image intensities. A second order polynomial fit to the data is used here, similar to the approach of Chuang & Huang [141] and Brody et al. [142], following Equations 4.1 and 4.2, with l and h being the greyscale intensity of the low and high energy region respectively, and b and c the empirically fit coefficients.

$$\begin{aligned}\text{bone thickness} = \big(&b_1 + b_2 l + b_3 h + b_4 l^2 + b_5 h^2 + b_6 lh \\ &+ b_7 l^2 h + b_8 l h^2 + b_9 l^2 h^2\big)\end{aligned} \tag{4.1}$$

$$\begin{aligned}\text{soft tissue thickness} = \big(&c_1 + c_2 l + c_3 h + c_4 l^2 + c_5 h^2 + c_6 lh \\ &+ c_7 l^2 h + c_8 l h^2 + c_9 l^2 h^2\big)\end{aligned} \tag{4.2}$$

When conducting this empirical calibration, it is important that the calibration phantom covers the full range of soft tissue and bone thicknesses which may be measured, as the calibration cannot be extrapolated outside of the known values. A series of 50 CT knee scans of early OA patients [143] was examined to determine the maximum thicknesses of bone and soft tissue. To calculate bone thickness, a threshold was selected to separate the bone pixels in the volumes, then mock AP and

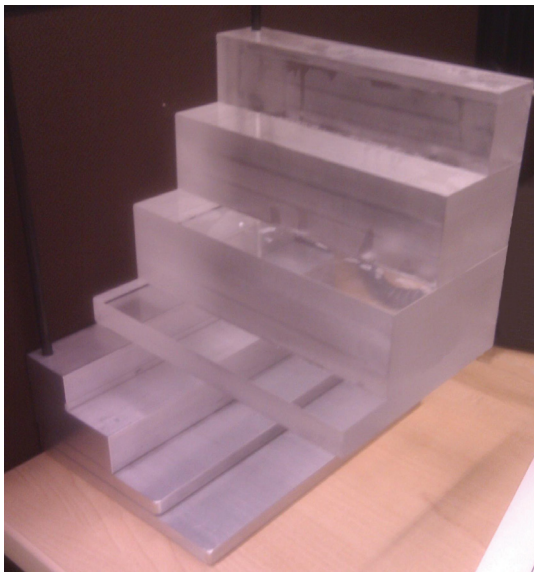

Figure 4.1: Cross-wedge phantom for calibrating empirical DXA equations. Aluminum simulates bone under x-ray, acrylic for soft tissue.

lateral views were created by summing all the pixels in those directions. The total values for the summed pixels was then divided by the equivalent cortical density in Houndsfield units to obtain a cortical bone equivalent thickness over the image from both views.

Standard materials used in creating x-ray phantoms include aluminum as a proxy for cortical bone, due to a similar atomic number and hence x-ray attenuation properties, and acrylic for soft tissue [61]. Aluminum is more dense than bone, however, so samples of aluminum and standard bone-equivalent plastic were scanned in two microCT scanners to compare attenuation.

4.2.1 Final Phantom Design Specifications

The peak bone thickness value measured from the CT images was found to be 8.69cm, where the cortical shell of the posterior femur lined up precisely with the lateral line of sight. Soft tissue was measured directly from the CT slices, with a maximum across the thigh above the patella of 16.0cm.

The linear x-ray attenuation of aluminum was found to be 1.3 $\pm$ 0.008 times higher than the bone equivalent plastic in the CT scans. Thus the maximum aluminum thickness needed for the x-ray phantom was 6.68cm.

In order to cover all combinations of bone and soft tissue, a cross-wedge phantom

design was used (see Figure 4.1), where steps of acrylic run perpendicular to the aluminum steps. The thickness of each step was set to span the most common thicknesses at the proximal tibia (much smaller than the maximum values), with the thicker levels adjusted to get a better spread in image brightness values, as the greyscale values and thickness are exponentially related. The aluminum wedge has four steps of 0.9525, 1.905, 4.445, and 6.83cm using stock 6061 bar aluminum, and the acrylic wedge has 1.763, 6.995, 12.228, and 16.662cm thick steps. The footprint is around 20cm square, including the "no step" regions on both wedges (which then encompass air to maximum thickness in each direction), which provides a stable base and is on the same scale as a knee to provide an estimation of scattering and noise. The aluminum bars are aligned using vertical carbon fibre rods threaded through common holes on each end of the step, and are long enough to also pass through a similar hole at the end of the acrylic wedge for support and alignment. The phantom was constructed by Dr. David Holdsworth's group at Robarts Imaging Institute (London, ON, Canada), and shipped for testing at the Halifax Infirmary.

4.2.2 Phantom Positioning and Background Subtraction

During imaging, the x-ray photons are generated at a point-source, then expand in a cone shape to cover the detector area (thus 2D x-ray imaging is often called "cone-beam imaging"). The angle the x-rays are to the horizontal surface of the detector causes the geometry of the object to be distorted, and this distortion depends on the distance that the object is from the source and the detector.

Due to the cone-beam distortions, it was determined that the acrylic wedge, instead of aligning precisely with the edge of the aluminum phantom, needs to be moved inward by about 2cm so the projected segments have approximately the same area. If the acrylic wedge is exactly aligned with the the aluminum one, with a common carbon fibre post through both, the top step of the acrylic phantom was projected beyond the footprint of the aluminum. Not being able to use the carbon fibre rod to support the weight of the acrylic wedge necessitated the use of a small acrylic post propped under the overhanging side (seen on the left side of the cross-wedge images as a small bright square).

This type of system also produces an incident beam that is not completely uniform over the surface of the detector. To ameliorate the effect of this on the DXA

calibrations, an image was taken with no phantom at both high and low energies, and a second order polynomial fit was made to this background image (see section 3.3.1). This background trend matrix was then subtracted from the phantom image matrix before analysis was conducted.

4.3 X-ray System Settings

As two sets of images are taken, at two different energy levels, consideration must be paid to the possibility of the patient moving between images. The characteristics of the system that contribute to this time between images are the time it takes to expose and transfer the image to the computer, and the time to set up the next image. Image registration post-processing can aid in removing motion that does occur, although is not expected to be as much of a problem with extremity images as it is with chest dual-energy subtraction, which commonly uses DXA to remove the ribs from lung images and has required the development of sophisticated image alignment algorithms. Nevertheless, it is simpler to reduce the chance of motion to begin with rather than try to remove it later. The image transfer and second image set-up times are beyond the scope of this project, but minimizing the time to expose the image was taken under consideration when choosing exposure levels.

The polyenergetic spectra produced by the x-ray generator have considerable spread (Figure 1.3). It is advisable to keep the peak energies for the high and low images as separated as possible to minimize the overlap of the spectra in both images, and keep the defining equations for bone mass assessment independent [74]. Of the dedicated DXA scanners, Hologic (Marlborough, MA) now uses 100kVp low energy and 140kVp high, Lexxos (DMS, Nimes, France) uses 75kVp and 140kVp, and Lunar (now GE Healthcare, Waukesha, WI) uses one 76kVp beam with a rotating filter to provide the low energy image. The new Canon CXDI-55C digital detectors at the Halifax Infirmary may be more sensitive than these systems, allowing for necessary contrast even at lower energies.

All tests were conducted with one x-ray source 150-160cm perpendicular above the detector, with two set-ups: (1) having the RSA calibration box between the phantom and the detector and (2) the phantom placed directly on the detector (Figure 4.2).

Automatic exposure control (AEC) was used for the first images to attain a ballpark figure for exposure variables at voltage settings which give a large separation between high and low energy images. These settings were then adjusted to prevent oversaturation, which leads to the same greyscale levels being assigned to the air segment as to the thinnest wedge sections.

4.3.1 X-ray System Settings: Results

The low energy settings using the AEC were 60kVp, 630mA, and 250ms, the high energy images were taken at 140kVp, 500mA, 25ms, with a 0.6mm copper filter; all images also have the lowest energy photons removed via the permanent 1.6mm aluminum system filter. The voltage settings remained the same, but subsequent manual entry of current and time was limited by software controls for such high current values (the software prevents the user from entering settings which might damage the generator system), so all the following low energy images use 320mA, and all high energy images 250mA. Setting the current to the maximum allowed minimizes the time for the same total exposure.

The original AEC exposure was too high to be able to distinguish between the air segment and the low thickness aluminum or acrylic, as the saturation limit of the detectors was reached. The exposure times, with the new lower currents, were adjusted to 160ms and 50ms respectively when the RSA calibration box was in the path of the beam, with a total exposure of 51.2mAs and 12.5mAs. Without the calibration box, the exposure times were dropped to 100ms for the low energy image and 25ms for the high energy image. Figure 4.3 shows the low and high energy images of the cross-wedge phantom, with the phantom directly on the detector.

4.3.2 Holding Calibration

The Canon software automatically adjusts the greyscale values of the images for optimum bone viewing before saving clinical images, which will not allow for intensity calibration between images. However, the raw images are held in a temporary folder, so those were retrieved for all the tests. Two images taken at different times on the same day with the same settings (with the phantom repositioned in between), and another taken two days later, were compared to determine how much the average greyscale values change between shots.

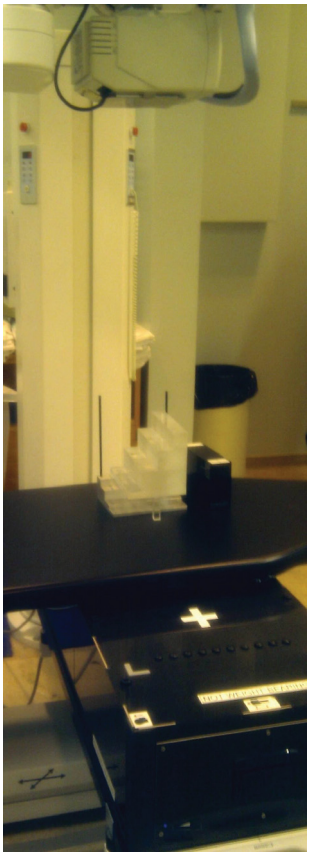

Figure 4.2: Example DXA test set-up: top of the image has the x-ray generator head, the cross-wedge phantom is on the table, and in this case under the table is the RSA calibration box with the digital detectors housed in the bottom.

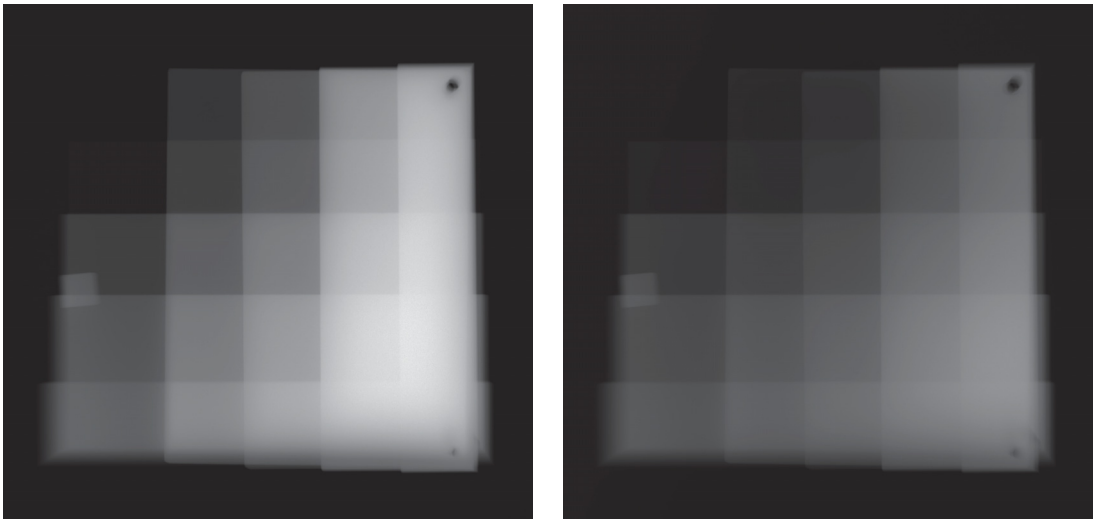

(a) Low Energy (b) High Energy

Figure 4.3: Low and high energy images of the cross-wedge phantom.

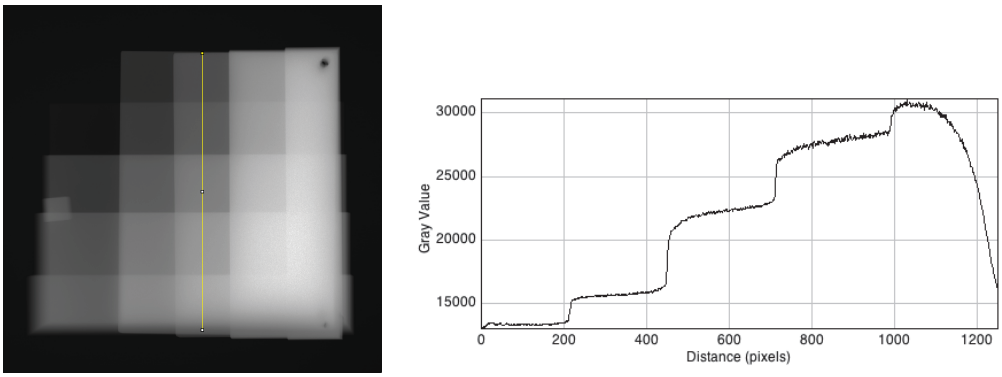

(a) Cross-wedge low energy image (b) Greyscale values along the yellow line in preceding image

Figure 4.4: Line profile of greyscale values along the second aluminum step of the cross-wedge phantom.

The coefficient of variation (CV) of four different regions on these images was a maximum of 3.5%, without adjustment for the intensity variation of the incident beam over the image area (background trend subtraction). The phantom was in the same general location each time, but some of that 3.5% is likely due to a spatial change in the field of view. Repositioning these regions on the same image gave a CV of less than 1%.

4.4 Material Thickness Calibration Results

4.4.1 Algorithm

The unprocessed images were read into Matlab, and an algorithm written to dynamically chose regions of interest with a graphical user interface using the `imrect` function. The average greyscale value in the low and high energy images for those region matrices was determined, and a fit to Equation 4.1 using the greyscale values and known aluminum thicknesses was found to obtain the empirical coefficients using Matlab's backslash operator (A\B, where A is the matrix of coefficients, and B is the vector of know thicknesses).

Region placement requires consideration due to the distorting effects of the cone-beam system (see section 4.4.2). The regions used for calibration were kept toward the centre of each segment unless otherwise noted (Figure 4.5).

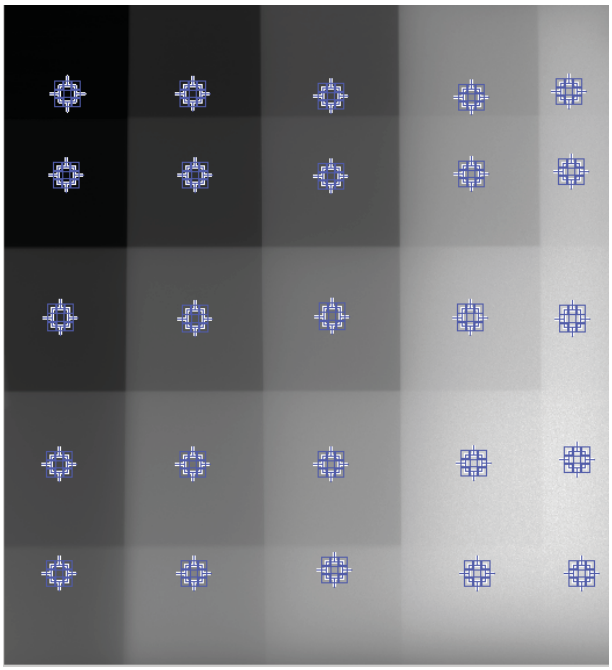

Figure 4.5: Small regions of interest placed for calibration of DXA algorithm. Locations were chosen to avoid the effects of cone-beam distortions and scatter on the average greyscale level.

4.4.2 Phantom Image Properties

Using 60kVp, 320mA, and 160ms for the low energy image, and 140kVp, 250mA, 50ms with a 0.6mm copper filter for the high energy image with the calibration box, and 100ms for the low and 25ms for the high energy image without the box, the difference between no material and the thinnest steps of the wedges is visible. This is excellent energy separation compared to the dedicated DXA scanners. Setting the acrylic wedge around 2cm before the end of the aluminum wedge provided image segments of differing aluminum and acrylic thickness that are approximately equal area. A line profile of the greyscale values along the second aluminum step is shown in Figure 4.4, with clearly distinguishable differences between each of the acrylic thicknesses.

The change in intensity along the highest aluminum step is more problematic. Even with higher exposure levels, or changing the voltage, the greyscale values create a continuous curve over the length of the step, instead of discrete steps (see Figure 4.7). A number of factors are likely influencing this result: the absolute change in greyscale value from the thinnest to thickest acrylic with that much aluminum

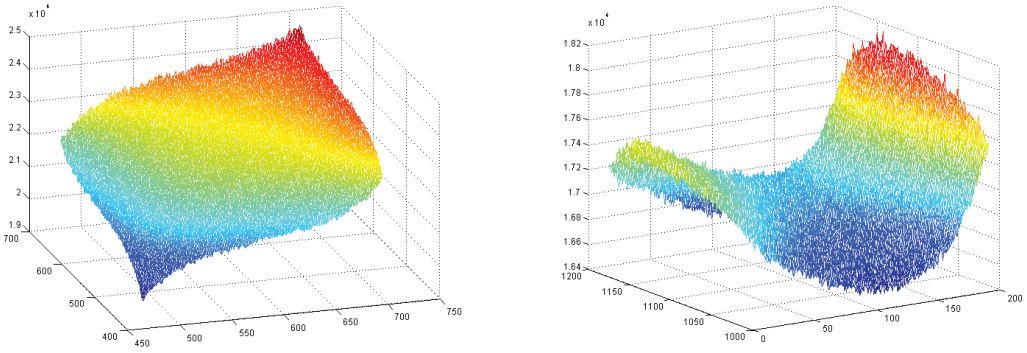

(a) Greyscale values of a centre segment

(b) Greyscale values of the lower left segment of the phantom (thickest acrylic, no aluminum)

Figure 4.6: Example greyscale value distributions of two segments of the cross-wedge phantom.

in the way is small; the amount of scattered photons in these thick regions will be a lot higher, adding more haze to the results; and the detectors have a limited dynamic range. The technical specifications suggest that the detectors can handle a change of 80dB in intensity values. Calculating the ideal intensity ranges using the single energy equations (1.2 and 1.3) shows that these thicknesses would produce a 78dB range of intensity over the image, so adding in broad spectrum energies and experimental variability, the dynamic range of the system may very well be affecting these results.

Figure 4.6 shows the distribution of the greyscale values in both directions of two segments of the cross-wedge phantom, thus expands the trends seen in the line profile in Figure 4.4. The centre segment plot is typical of most regions: instead of a flat profile, where the constant thickness causes a constant brightness on the image, there is a slope. In the centre segment, this slope gives greyscale values ± 12% of the average value from the peak to the trough. The higher values are along the edges of the segment that connect to thicker steps, and the lower values are against the thinner steps. The lower left segment is showing a more complicated pattern, however. This is the thickest acrylic step, and there is no aluminum below it. Instead of a simple slope, this segment shows a double saddle trend. For the segments showing this valley trend in greyscale value, the average value in the dip was used for calibration.

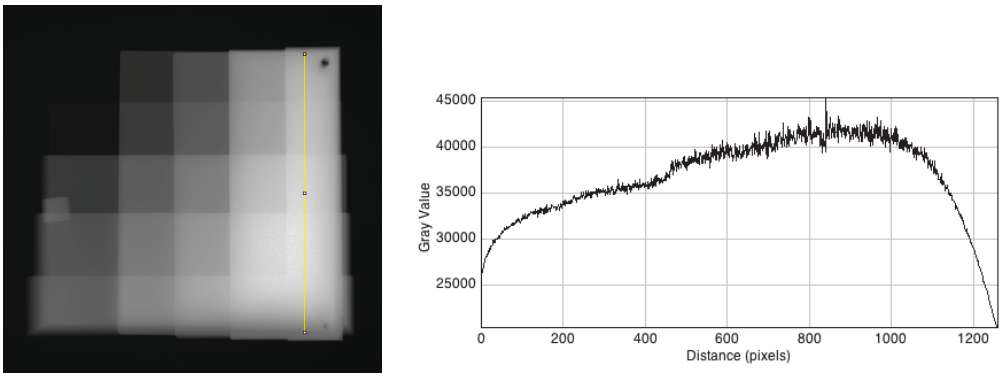

(a) Cross-wedge low energy image (b) Greyscale values along the yellow line in preceding image

Figure 4.7: Line profile of greyscale values along the thickest alumimum step of the cross-wedge phantom.

4.4.3 Coefficient Fit Results

Using any 3 region by 3 region square only, the Matlab algorithm finds a perfect solution to the nine coefficients in equations 4.1 and 4.2, and using those coefficients finds exactly the thicknesses used for the calibration. This restricts the range of thicknesses that can be determined by analyzing the images to those within the limits of that 3x3 region. When using more regions, the system is now overdetermined, with more equations than unknowns. Matlab's backslash operator automatically uses a least squares fit in these situations.

As was seen in the line profiles (Figures 4.4 and 4.7), it is difficult to pick the true greyscale values of the thickest regions, as many factors lead to blurring. So the next test used regions from the three middle columns (aluminum thicknesses 0.95 to 4.44cm) and top four rows (acrylic thicknesses 0 to 12.23cm) to calculate the empirical coefficients. Using those coefficients with the same region greyscale values gives aluminum thickness results within -0.48% and +1.3% of actual. Figure 4.8 shows the polynomial fit to the calibration data (red dots).

If centred regions on all 25 segments were naively used, the complex greyscale trend seen in Figure 4.6 means that the average value of the region in the thickest segment ends up being lower than the next step down. An empirical fit to these nonmonotonic values has given thickness values up to 31% lower than true aluminum dimensions for some segments (see Figure 4.9). Thus distorted sections of the image can greatly affect the coefficient fit.

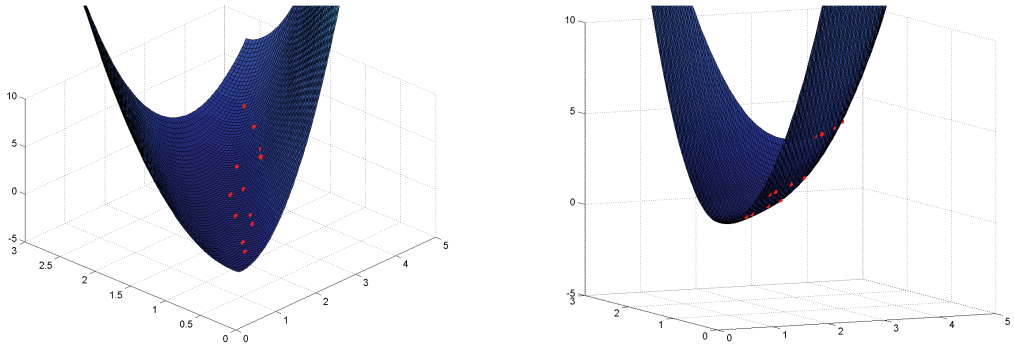

(a) Fit seen from above

(b) Fit seen from below

Figure 4.8: Polynomial fit of known aluminum thicknesses of 12 central segments to high and low energy greyscale values. x- and y-axes are greyscale values /10000, the z-axis is aluminum thickness in cm. Fit curve is within 1.3% of given thicknesses (red dots).

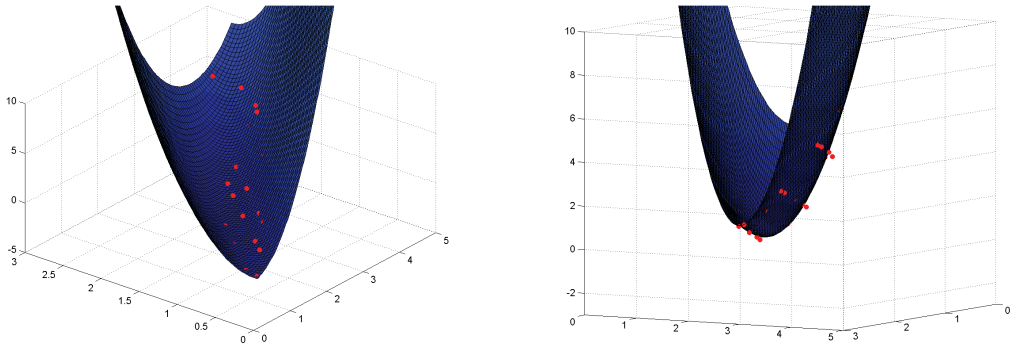

(a) Fit seen from above

(b) Fit seen from below

Figure 4.9: Polynomial fit of known aluminum thicknesses for all segments to high and low energy greyscale values. Fit curve is within 31% of given thicknesses (red dots).

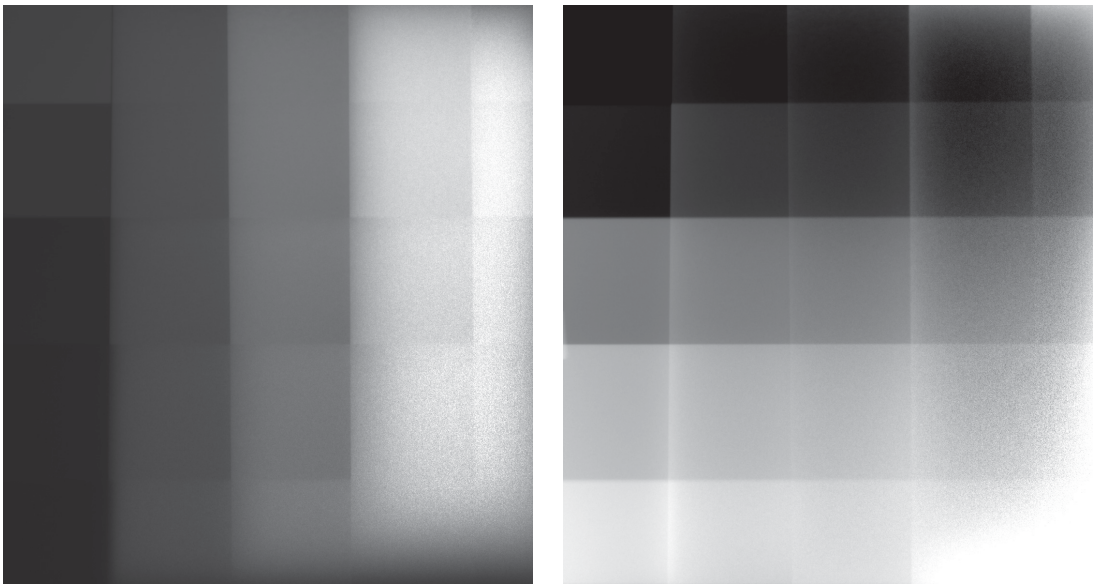

(a) Aluminum-only decomposed image (b) Acrylic-only decomposed image

Figure 4.10: Decomposed images using empirical calibration based on middle three columns and top four rows. Note that calibration is not valid outside of these regions, so variation in the peripheral regions is expected.

4.4.4 Applying Calibration Over Whole Image

With the coefficients found, the polynomial equations can then be applied to the whole images to create "bone-only" (or aluminum only) and "soft-tissue" only images. With the cross-wedge phantoms, the former should look like a set of vertical bars, and the latter a set of horizontal bars. Figures 4.10(a) and 4.10(b) are based on the more precise calibration over the three aluminum steps and four acrylic steps, so note that *the calibration is not accurate past these thicknesses.* In an ideal set-up, the three middle columns up until the last row should be a single value each in the aluminum-only image, and the three middle segments of each of the top four rows should be a single value each in the acrylic-only image. Only the aluminum image will be used for DXA calculations.

Increased noise is seen in the dual-energy subtracted images, as noted by Warp & Dobbins [144]: compare the line profile of the third aluminum step in the aluminum only image (Figure 4.11) against the original image line profiles. The combination of sources of experimental uncertainty, including noise, scatter, and cone-beam distortions, give calculated variations in thickness in the aluminum-only image between -35% and +63% of actual perpendicular projected amounts over the calibrated area.

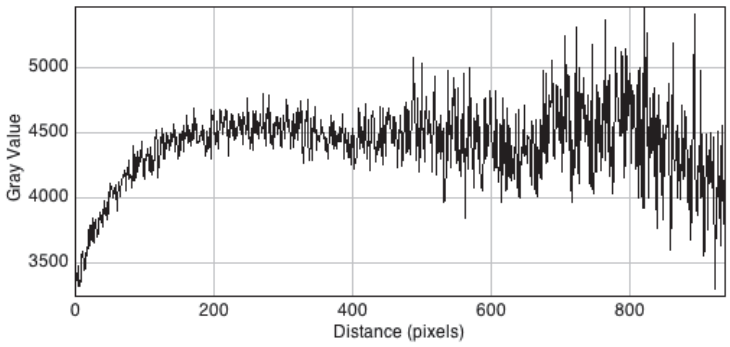

Figure 4.11: Line profile along the third aluminum step (fourth column) in the aluminum-only decomposed image. Y values are equivalent to aluminum thickness in cm *1000.

4.4.5 RSA Calibration Box Effects

The images used for the above tests are of the phantom directly on the detector. Having the RSA calibration box in the way, even with the increased air gap and an antiscatter grid, adds more noise to the image (see Figure 4.13). For tests with the RSA calibration box in the field of view, the calibration regions also needed to avoid the control bead markers and their associated washer halos. The spread of these artifacts can be seen in Figure 4.12, and force some regions away from the optimal positioning.

Between moving regions to avoid control bead artifacts (thus introducing more scatter effects and potentially overlapping with cone beam distorted areas), and increased scatter from the calibration box, the polynomial fits had residuals of up to ±20% for the aluminum thicknesses when the same greyscale values used in the calibration were placed back in the equations, as opposed to the less than 1.5% errors seen without the RSA calibration box.

4.5 Final Notes

Since the SR Suite operates two x-ray generator heads, it was thought that it might be possible to obtain AP and lateral views of the knee at the same time, by setting each at a 45° angle to the vertical and repositioning the subject. However, the tracks that the heads move on are not extensive enough to allow for this configuration and have the x-ray photons reach the detectors on both sides. The standard RSA set-up

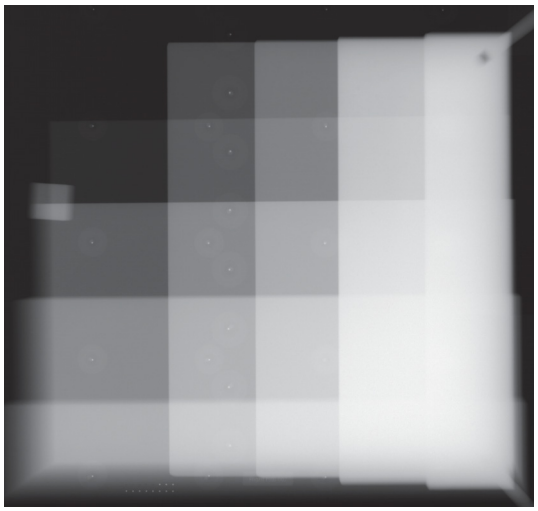

Figure 4.12: Low energy cross-wedge image with RSA calibration box between the phantom and the detectors. Note the bright control beads with halos around them from the calibration box which need to be avoided when placing regions for DXA calibration.

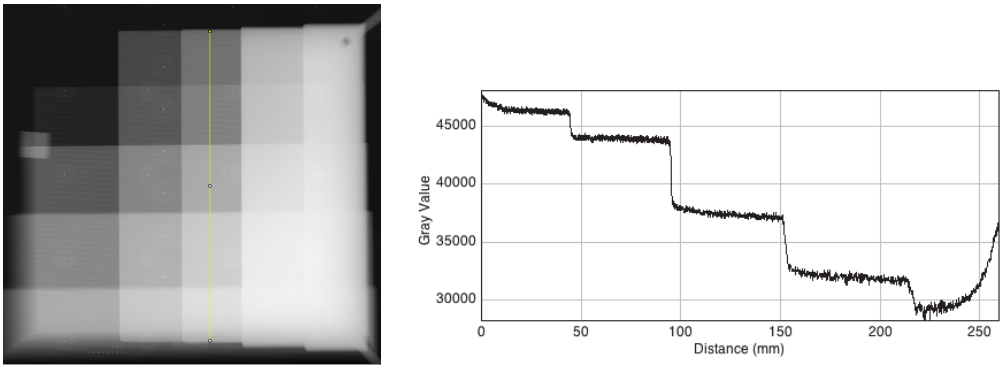

(a) Cross-wedge low energy image (b) Greyscale values along the yellow line in preceding image

Figure 4.13: Line profile of greyscale values along the second alumimum step of the cross-wedge phantom, with RSA calibration box between the phantom and the detector. Compare noise to Figure 4.4.

with the detector heads at 30° from the vertical necessitates the overlap of the fibula and tibia in at least one image. The overlapping bone region was rejected in the previous texture analysis, and will confound BMD measurement. It may be possible to use the second image to measure the fibula BMD to subtract off the overlapping version, although the accuracy of this technique will depend on how symmetrical the fibula profile is for each patient.

No attempts were made to clean the images of shot noise (dependent on number of photons), or dark current noise of the detectors. The field of view was limited by columnators to restrict the photon beam to only the area needed, which helps prevent extra scattered photons from other objects bouncing back into the portion of the image that is needed.

A word on dose considerations: digital detectors need less exposure than film or computed radiography to obtain clear images, and standard knee radiographs incur very little dose compared to average background radiation (about 65% of the average US daily background dose, and one-thousandth the dose of a pelvic CT scan), but they still expose the patient to about five times the radiation of a standard DXA scan [144, 145, 146].

Chapter 5

Summary and Discussion

5.1 Overview

The objective of this study to examine links between radiographically measured bone quality parameters and total knee replacement implant migration. Computational tools were designed to calculate image texture parameters that have been previously linked with 3D bone microarchitecture, as well as an additional one which theoretically could help distinguish between healthy high contrast trabecular structures and the washed out appearance of thin struts. Combining these parameters with measured bone mineral density provided a set of descriptive variables which were used to train Random Forest™ statistical models to assess sensitivity and specificity of classifying study participants based on implant migration. Additionally, the feasibility of determining bone thickness (linked to areal BMD through a single density factor) using the SR Suite radiography equipment was examined by creating an empirical fit to a purpose-built double step wedge x-ray phantom.

5.2 Conclusions and Discussion

Hypothesis 1

A model based on radiographic derived bone microarchitecture and bone mineral density parameters will identify study participants with RSA measured implant migration between one and two years above and below a set cut-point.

Conclusions 1

Texture analysis requires high spatial resolution in order to examine trabecular

bone structure. Thus only the two year images from the uncemented studies could be analyzed for these parameters. The use of model-based RSA analysis was needed to minimize the number of study participants lost due to lack of migration data, as insufficient bead matching in the more accurate marker-based technique would have prevented up to 32% of the study population from being analyzed. 88% of this study population would be classified "at risk" using the Ryd et al. [20] cut-point of 0.2mm when using model-based RSA MTPM at 2 years with 1 year exam as reference. Finding the vector based change in MTPM is the likely reason the average change much higher than in the reference study, as a subtraction of the two year MTPM from the one year motion, with both using the post-operative exam as reference, 22% would be classified at risk which is lower than the 31% in the Ryd study. With the same percentage "at risk", the vector based change in MTPM cut-point would be around 0.6mm.

Random Forest™ models were built which had a maximum sensitivity of 87.5% and specificity of 80% when classifying subjects who had more than 0.3mm maximum point motion of their implant at two years when the one year exam was used as reference. If 0.6mm proves to be a clinically significant indicator of future loosening, a second model had a sensitivity of 75% and specificity of 100% for classifying the implant migration of subjects based on bone texture. Other cut-points were examined, with models having a lower specificity for a tighter acceptable migration outcomes, and lower sensitivity if higher migrations were acceptable.

Subtracting the magnitude of the MTPM vectors at two years and one year gave smaller average values of migration over this time frame, as it does not include the change in direction. Models were not as sensitive when classifying this outcome, with a sensitivity of 50% and a specificity of 93% for a two parameter model determining groups based on a 0.1mm cut-point. Using the literature based 0.2mm cut-point for an "at risk" population, a one parameter model has a true positive rate of 40% and a true negative rate of 85%. For classification based on subsidence of the implant between one and two years, a three parameter model has a sensitivity of 78% and a specificity of 71% for a 0.05mm cut-point.

Most of the important parameters in the classification models were based on the image region wavelet decomposition. These were also the parameters which had the

lowest variability when the region was moved on a single image (placement error) compared to the range of values for all the study participants. The first moment of the power spectrum (Fourier analysis) was helpful in the models which classified the magnitude subtracted MTPM outcome measure. One distal tibia, proximal stem, and peri-articular region were found important for the various models; the femoral ROI was not helpful in these classifications.

Bone mineral density was not found to increase the ability of the models to classify implant migration groups.

Limitations and Discussion 1

The clinical relevance of migration thresholds using model-based RSA techniques is not yet known. Future analysis of this study population will determine which implants go on to continuous migration, and whether these models would identify those implants at the two year mark.

The small study sizes means limited data to train the Random Forest™ ensemble models. All cut-points which had only a small number of images in one group fared poorly at classifying that small group. Larger data sets will be needed to find the clinically relevant definitions of "stable" and "at risk", and create robust models to predict those at risk.

It has been shown that the relatively small amount of soft tissue available around the knee can cause variation in the soft-tissue baseline calculated by the software used in calibrating the BMD algorithms, and thus the coefficient of variation in knee scans has been shown to be anywhere from 2.5-18.7% [147, 148, 149]. Occasionally, the bone edge detection within the software can exclude some of the tibia or include large portions of soft tissue. The latter can be adjusted, either in manually choosing the bone edge or being very precise in ROI placement, but the former cannot be reversed. The important changes in the bone matrix may also be local to the peri-implant interface and may be obscured by the large regions of interest used here.

It is encouraging, however, to see that the bone texture parameters have been able to identify study participants based on implant migration patterns even in this small study.

Hypothesis 2

A model based on radiograph derived bone microarchitecture parameters calculated from immediately post-operative x-ray images will predict study participants with RSA measured implant migration at one year above and below a set cut-point.

Conclusions 2

A one parameter model based on post-op bone texture found a sensitivity of 75% and a specificity of 80% when predicting those study participants who went on to more or less than 0.4mm total migration by one year. Although these data also were using model-based RSA, the average one year MTPM for the cemented implant is in agreement with cemented studies in the literature [21, 150, 20] even with the median MTPM 0.11mm higher for the model-based migrations than marker-based (comparing study participants with both modes available).

While the participant numbers are too small to show robust links, the ability of the model to correctly categorize migration patterns for one of the chosen cut-points suggests that further research ought to be pursued in this area.

Limitations and Discussion 2

The cemented Stryker Triathlon study used for this analysis is currently in the beginning stages, and only 18 total knee arthroplasty study participants had one year migration results available at the time of this work. Setting different cut-points for one year migration was difficult due to the small sample size, with some groups only having 3 participants. Thus the exact results of these tests should not be examined as a robust indication of classification ability of these models, but as a pilot study which suggests that it is possible that pre-operative bone texture could be predictive of later implant migration. It would be especially enlightening to wait for 2 year data on a larger group of participants (this is a continuous enrolment study) to assess the predictive capability of post-op bone on the more accepted one to two year migration patterns.

Hypothesis 3

An empirical calibration of the system using an x-ray phantom with bone and

soft-tissue mimicking materials will accurately identify the material thicknesses from high and low energy image greyscale values and maintain the calibration over one day.

Conclusions and Limitations 3

A cross-wedge calibration phantom was designed and built using measured thicknesses of bone and soft tissue of the knee from CT scans of OA study participants. Aluminum was used as the bone equivalent material, and acrylic was used for soft tissue.

The coefficient of variation of the region greyscale values in 3 images spread over 3 days is under 4%, even without removing the background trend from incident energy variation, showing the stability of the system to hold a calibration between phantom exams and patient scans.

An empirical fit to central regions of the cross-wedge calibration phantom returned residuals of less than $\pm 1.5\%$ for the aluminum thicknesses, which would be the ones used to determine bone mineral density of the proximal tibia. Wedge segment greyscale values were not constant over each region, even though the materials were at a constant thickness; scattered photons are likely to blame for the sloped intensity trends. The average value in the centre of the segment was used for calibration, but using that value to calibrate the fit will obviously mean the calculated thicknesses of the rest of the segment will deviate from the known amount.

The thickest regions of the phantom presented difficulties, as image distortions from the angled cone-beam x-rays, scattered photons, and potential difficulties with the dynamic range of the system added up to a potential break in the monotonic relationship between thickness and greyscale level (the thickest regions showing less attenuation than the next step down). This leads to much higher residuals between the actual thickness and the empirical fit ($> 30\%$ for the aluminum thicknesses).

In summary, the incident energy remained consistent over a period of at least three days, and the algorithm provided an empirically fit model to translate greyscale intensity values from high and low energy projection images to known material thicknesses. Noise, scatter, and cone-beam projection distortions were not corrected in these tests.

5.3 Future Work

With time, continuous migration status on the uncemented study participants, and one to two year data for a larger pool of cemented knee arthroplasties will become available, to more rigorously determine if these models are clinically useful. A larger study population would also allow for more strict rules for region placement (as regions with artifacts could be discarded), reducing the variability in the parameter values.

The bone mineral density of the proximal tibia was not able to add value to the bone texture model classifications the subjects into groups based on migration patterns. A higher spatial precision with software calibrated specifically for the knee may find that bone mineral is in fact an indicator of the bone's ability to withstand implant stresses.

A new design of calibration phantom for calculating BMD from 2D x-ray images which focuses on the range of bone and soft tissue thicknesses within the expected regions of interest (i.e. the proximal tibia) rather than making sure all areas of the image would be accurately measured may avoid issues of excessive scatter and dynamic range issues. A phantom designed to align with the cone-beam angles so the actual thickness of each material seen by the beam is known may assist in finding true calibration accuracy. Noise and scatter modelling will likely be necessary for a clinically useful system, and should incorporate anatomical based models.

The potential of the multiple viewpoints available in the RSA images remains untapped; integrating these bone quality parameters into the MBRSA software to determine the location of the regions of interest in 3D space may provide informative relationship links between the regions, and allow for precise removal of the implant to examine periprosthetic bone more closely.

It must be remembered that bone is just part of the overall human system, and is unlikely to be predictive in isolation. While the small numbers of study participants here prevented adding yet more descriptive variables, clinically relevant metrics like pre-operative varus angle, patient BMI, gait patterns, and activity level are likely to be important in discriminating which patients are more at risk of implant loosening and failure.

5.4 Summary

There is currently no bone health predictor of implant stability for surgical decision making and follow-up. Patients are assessed for surgery qualitatively by orthopaedic surgeons using such metrics as range of motion, joint space narrowing as seen on radiographs, and by observing the patient walk. While RSA measured implant migration is highly precise and can find implant loosening much earlier than standard radiographs, it is not helpful in planning pre-surgery. With demand for knee replacements increasing with an ageing and obese population, and with increased demands on those new knees, finding patient-specific biometrics of arthroplasty success could make a big difference in the burden of joint replacement on both patients and the health care system.

The pilot studies outlined here show the potential for radiograph-derived bone quality parameters to predict implant migration. Future work with larger studies, and incorporating other metrics such as gait and limb alignment, has the exciting opportunity to create a patient-specific score to give both surgeons and patients a better assessment of the personal risks and benefits of arthroplasty surgery.

Bibliography

[1] Canadian Institute for Health Information. Hip and Knee Replacements in Canada – Canadian Joint Replacement Registry (CJRR) 2008-2009 Annual Report. Ottawa, Ont: CIHI; 2009.

[2] Jones DL, Westby MD, Greidanus N, Johanson NA, Krebs DE, Robbins L, et al. Update on hip and knee arthroplasty: current state of evidence. Arthritis and Rheumatism. 2005 Oct;53(5):772–80.

[3] Lidgren L, Robertsson O. Annual report 2007: The Swedish Knee Arthroplasty Register. Lund, Sweden: Lund University Hospital Department of Orthopedics; 2007.

[4] Bodén H, Sköldenberg OG, Salemyr MOF, Lundberg HJ, Adolphson PY. Continuous bone loss around a tapered uncemented femoral stem: a long-term evaluation with DEXA. Acta Othopaedica. 2006 Dec;77(6):877–85.

[5] Dunbar MJ, Howard A, Bogoch ER, Parvizi J, Kreder HJ. Orthopaedics in 2020: predictors of musculoskeletal need. The Journal of Bone and Joint Surgery, American Volume. 2009 Sep;91(9):2276–86.

[6] Talmo CT, Shanbhag AS, Rubash HE. Nonsurgical management of osteolysis: challenges and opportunities. Clinical Orthopaedics and Related Research. 2006 Dec;453(453):254–64.

[7] Rand JA, Ilstrup DM. Survivorship analysis of total knee arthroplasty. Journal of Bone and Joint Surgery, American Volume. 1991;73-A(3):397–409.

[8] Springer BD, Fehring TK, Griffin WL, Odum SM, Masonis JL. Why revision total hip arthroplasty fails. Clinical Orthopaedics and Related Research. 2009 Jan;467(1):166–73.

[9] Lane NE, Brandt K, Hawker G, Peeva E, Schreyer E, Tsuji W, et al. OARSI-FDA initiative: defining the disease state of osteoarthritis. Osteoarthritis and cartilage / OARS, Osteoarthritis Research Society. 2011 May;19(5):478–82.

[10] Wong R, Davis AM, Badley E, Grewal R, Mohammed M. Prevalence of arthritis and rheumatic diseases around the world: A Growing Burden and Implications for Health Care Needs. Toronto: Arthritis Community Research and Evaluation Unit, University Health Network; 2010. April.

[11] Badley EM, Rothman LM, Wang PP. Modeling physical dependence in arthritis: the relative contribution of specific disabilities and environmental factors. Arthritis Care and Research. 1998 Oct;11(5):335–45.

[12] Coyte PC, Asche CV, Croxford R. The economic cost of musculoskeletal disorders in Canada. Arthritis Care and Research. 1998;11(5):315–325.

[13] Felson DT. Obesity and vocational and avocational overload of the joint as risk factors for osteoarthritis. Journal of Rheumatology. 2004;31(Suppl. 70):2.

[14] Felson DT, Anderson JJ, Naimark A, Walker AM, Meenan RF. Obesity and knee osteoarthritis. The Framingham Study. Annals of Internal Medicine. 1988 Jul;109(1):18–24.

[15] Kurtz S, Ong K, Lau E, Mowat F, Halpern M. Projections of primary and revision hip and knee arthroplasty in the United States from 2005 to 2030. The Journal of Bone and Joint Surgery, American Volume. 2007 Apr;89(4):780–5.

[16] Time out! Report card on wait times in Canada. Ottawa, Ont: Wait Time Alliance; 2011. June.

[17] Teeny S. Long-term follow-up care recommendations after total hip and knee arthroplasty: Results of the American Association of Hip and Knee Surgeons' member survey. The Journal of Arthroplasty. 2003 Dec;18(8):954–962.

[18] Potter HG, Nestor BJ, Sofka CM, Ho ST, Peters LE, Salvati EA. Magnetic resonance imaging after total hip arthroplasty : Evaluation of periprosthetic soft tissue. The Journal of Bone and Joint Surgery. 2004;86(9):1947.

[19] Valstar E. The use of Roentgen stereophotogrammetry to study micromotion of orthopaedic implants. ISPRS Journal of Photogrammetry and Remote Sensing. 2002 Aug;56(5-6):376–389.

[20] Ryd L, Albrektsson BE, Carlsson L, Dansgard F, Herberts P, Lindstrand A, et al. Roentgen stereophotogrammetric analysis as a predictor of mechanical loosening of knee prosthesis. Journal of Bone and Joint Surgery, British Volume. 1995;77(3):377.

[21] Grewal R, Rimmer MG, Freeman MAR. Early migration of prostheses related to long-term survivorship. Journal of Bone & Joint Surgery, British Volume. 1992;74-B(2):239–242.

[22] Freeman MA, Plante-Bordeneuve P. Early migration and late aseptic failure of proximal femoral prostheses. Journal of Bone and Joint Surgery, British Volume. 1994;76(3):432.

[23] Karrholm J, Borssen B, Lowenhielm G, Snorrason F. Does early micromotion of femoral stem prostheses matter? Journal of Bone and Joint Surgery, British Volume. 1994;76(6):912.

[24] Kobayashi A, Donnelly WJ, Scott G. Early radiological observations may predict the long-term survival of femoral hip prosthesis. Journal of Bone and Joint Surgery, British Volume. 1997;79-B:583–589.

[25] Dunbar MJ, Wilson DAJ, Hennigar AW, Amirault JD, Gross M, Reardon GP. Fixation of a trabecular metal knee arthroplasty component: A prospective randomized study. The Journal of Bone and Joint Surgery, American Volume. 2009 Jul;91(7):1578–86.

[26] Petersen MM, Nielsen PT, Lebech A, Toksvig-Larsen S, Lund B. Preoperative bone mineral density of the proximal tibia and migration of the tibial component after uncemented total knee arthroplasty. The Journal of Arthroplasty. 1999 Jan;14(1):77–81.

[27] Regnér LR, Carlsson LV, Kärrholm JN, Hansson TH, Herberts PG, Swanpalmer J. Bone mineral and migratory patterns in uncemented total knee arthroplasties: a randomized 5-year follow-up study of 38 knees. Acta Orthopaedica Scandinavica. 1999 Dec;70(6):603–8.

[28] Derbyshire B, Prescott RJ, Porter ML. Notes on the use and interpretation of radiostereometric analysis. Acta Orthopaedica. 2009;80(1):124–30.

[29] Robertsson O, Dunbar MJ, Pehrsson T, Knutson K, Lidgren L. Patient satisfaction after knee arthroplasty: a report on 27,372 knees operated on between 1981 and 1995 in Sweden. Acta Orthopaedica Scandinavica. 2000 Jun;71(3):262–7.

[30] Drees P, Eckardt A, Gay RE, Gay S, Huber LC. Mechanisms of disease: Molecular insights into aseptic loosening of orthopedic implants. Nature Clinical Practice: Rheumatology. 2007 Mar;3(3):165–71.

[31] Astephen Wilson JL, Wilson DAJ, Dunbar MJ, Deluzio KJ. Preoperative gait patterns and BMI are associated with tibial component migration. Acta Orthopaedica. 2010 Aug;81(4):478–86.

[32] Bauer TW, Schils J. The pathology of total joint arthroplasty: II. Mechanisms of implant failure. Skeletal Radiology. 1999 Sep;28(9):483–97.

[33] Schmalzried TP, Callaghan JJ. Wear in Total Hip and Knee Replacements. The Journal of Bone and Joint Surgery. 1999;81-A(1):115–136.

[34] Wong AS, New AMR, Isaacs G, Taylor M. Effect of bone material properties on the initial stability of a cementless hip stem: A finite element study. Proceedings of the Institution of Mechanical Engineers, Part H: Journal of Engineering in Medicine. 2005 Jan;219(4):265–275.

[35] Stadelamann VA, Terrier A, Pioletti DP. Osteoclastogenesis can be mechanically-induced in the peri-implant bone. IRBM. 2009 Feb;30(1):10–13.

[36] Berry DJ. Periprosthetic fractures associated with osteolysis: a problem on the rise. The Journal of Arthroplasty. 2003 Apr;18(3 Suppl 1):107–11.

[37] Harris WH. Wear and periprosthetic osteolysis: the problem. Clinical Orthopaedics and Related Research. 2001 Dec;(393):66–70.

[38] Wilkie JR, Giger ML, Engh CA, Hopper RH, Martell JM. Radiographic texture analysis in the characterization of trabecular patterns in periprosthetic osteolysis. Academic Radiology. 2008 Feb;15(2):176–85.

[39] Chappard D, Baslé MF, Legrand E, Audran M. New laboratory tools in the assessment of bone quality. Osteoporosis international : a journal established as result of cooperation between the European Foundation for Osteoporosis and the National Osteoporosis Foundation of the USA. 2011 Aug;22(8):2225–40.

[40] Barth HD, Launey ME, Macdowell AA, Ager JW, Ritchie RO. On the effect of X-ray irradiation on the deformation and fracture behavior of human cortical bone. Bone. 2010 Jun;46(6):1475–85.

[41] Morgan EF, Bouxsein ML. Biomechanics of bone and age-related fractures. In: Bilezikian JP, Raisz LG, Martin TJ, editors. Principles of Bone Biology. 3rd ed. 617. San Diego: Elsevier Inc.; 2008. p. 29.

[42] Viguet-Carrin S, Garnero P, Delmas PD. The role of collagen in bone strength. Osteoporosis International. 2006 Jan;17(3):319–36.

[43] Seeman E, Delmas PD. Bone quality–the material and structural basis of bone strength and fragility. The New England journal of medicine. 2006 May;354(21):2250–61.

[44] Griffith JF, Genant HK. New imaging modalities in bone. Current rheumatology reports. 2011 Jun;13(3):241–50.

[45] Seeman E. Material and structural basis of bone fragility : Determinants of bone strength. In: Qin L, Genant HK, Griffith JF, Leung KS, editors. Advanced Bioimaging Technologies in Assessment of the Quality of Bone and Scaffold Materials: Techniques and Applications. Heidelberg: Springer-Verlag; 2007. p. 393.

[46] Wigderowitz CA, Paterson CR, Dashti H, McGurty D, Rowley DI. Prediction of bone strength from cancellous structure of the distal radius: Can we improve on DXA ? Osteoporosis International. 2000;11(10):840–846.

[47] Clarke S, Wakeley C, Duddy J, Sharif M, Watt I, Ellingham K, et al. Dual-energy X-ray absorptiometry applied to the assessment of tibial subchondral bone mineral density in osteoarthritis of the knee. Skeletal Radiology. 2004 Oct;33(10):588–95.

[48] Lynch JA, Hawkes DJ, Buckland-Wright JC. Analysis of texture in macroradiographs of osteoarthritic knees using the fractal signature. Physics in Medicine and Biology. 1991 Jun;36(6):709–22.

[49] Taylor M, Tanner KE. Fatigue failure of cancellous bone: a possible cause of implant migration and loosening. The Journal of Bone and Joint Surgery, British Volume. 1997 Mar;79(2):181–2.

[50] Taylor M, Tanner KE, Freeman MA. Finite element analysis of the implanted proximal tibia: a relationship between the initial cancellous bone stresses and implant migration. Journal of Biomechanics. 1998 Apr;31(4):303–10.

[51] Perillo-Marcone A, Ryd L, Johnsson K, Taylor M. A combined RSA and FE study of the implanted proximal tibia: correlation of the post-operative mechanical environment with implant migration. Journal of Biomechanics. 2004 Aug;37(8):1205–13.

[52] Li MG, Nilsson KG. No relationship between postoperative changes in bone density at the proximal tibia and the migration of the tibial component 2 years after total knee arthroplasty. The Journal of Arthroplasty. 2001 Oct;16(7):893–900.

[53] Wooley PH, Schwarz EM. Aseptic loosening. Gene therapy. 2004 Feb;11(4):402–7.

[54] Meding JB, Galley MR, Ritter MA. High survival of uncemented proximally porous-coated titanium alloy femoral stems in osteoporotic bone. Clinical Orthopaedics and Related Research. 2010 Feb;468(2):441–7.

[55] Lonner JH, Klotz M, Levitz C, Lotke PA. Changes in bone density after cemented total knee arthroplasty: influence of stem design. The Journal of Arthroplasty. 2001 Jan;16(1):107–11.

[56] Van Loon CJM, De Waal Malefijt MC, Buma P, Verdonschot N, Veth RPH. Femoral Bone Loss in Total Knee Arthroplasty A Review. Acta Orthopaedica Belgica. 1999;65(2):154–163.

[57] Venesmaa PK, Kröger HP, Miettinen HJ, Jurvelin JS, Suomalainen OT, Alhava EM. Monitoring of periprosthetic BMD after uncemented total hip arthroplasty with dual-energy X-ray absorptiometry–a 3-year follow-up study. Journal of Bone and Mineral Research. 2001 Jun;16(6):1056–61.

[58] Johanson NA, Litrenta J, Zampini JM, Kleinbart F, Goldman HM. Surgical treatment options in patients with impaired bone quality. Clinical Orthopaedics and Related Research. 2011 Mar;469(8):2237–47.

[59] Completo A, Fonseca F, Simões JA. Strain shielding in proximal tibia of stemmed knee prosthesis: Experimental study. Journal of Biomechanics. 2008 Jan;41(3):560–6.

[60] Hopper T. Quantitative MRI and micro-CT of bone architecture : applications and limitations in orthopaedics [dissertation]. Queensland University of Technology, Brisbane, Australia; 2005.

[61] Krmar M, Shukla S, Ganezer K. Bone densitometry using x-ray spectra. Physics in Medicine and Biology. 2010;55:6105.

[62] Blake GM, Fogelman I. An update on dual-energy x-ray absorptiometry. Seminars in Nuclear Medicine. 2010 Jan;40(1):62–73.

[63] Griffith JF, Genant HK. Bone mass and architecture determination: state of the art. Best Practice & Research: Clinical Endocrinology & Metabolism. 2008 Oct;22(5):737–64.

[64] Järvinen TLN, Kannus P, Sievänen H. Bone quality : Emperor's new clothes. Journal of Musculoskeletal and Neuronal Interactions. 2008;8(1):2–9.

[65] Petersen MM, Jensen NC, Gehrchen PM, Nielsen PK, Nielsen PT. The relation between trabecular bone strength and bone mineral density assessed by dual photon and dual energy X-Ray absorptiometry in the proximal tibia. Calcified Tissue International. 1996 Oct;59(4):311–314.

[66] Blake GM, Fogelman I. The clinical role of dual energy X-ray absorptiometry. European Journal of Radiology. 2009 Sep;71(3):406–14.

[67] El Maghraoui A, Roux C. DXA scanning in clinical practice. QJM : Monthly Journal of the Association of Physicians. 2008 Aug;101(8):605–17.

[68] Alberich-Bayarri A, Marti-Bonmati L, Angeles Perez M, Jose Lerma J, Moratal D. Finite element modeling for a morphometric and mechanical characterization of trabecular bone from high resolution magnetic resonance imaging. In: Moratal D, editor. Finite Element Analysis. InTech; 2010. p. 195–208.

[69] Kiratli BJ, Heiner JP, McBeath AA, Wilson MA. Determination of bone mineral density by dual x-ray absorptiometry in patients with uncemented total hip arthroplasty. Journal of Orthopaedic Research. 1992;10:836–844.

[70] Webb AG. X-ray imaging and computed tomography. In: Introduction to Biomedical Imaging. Wiley-IEEE Press; 2002. p. 1.

[71] Jan J. Imaging Systems as Data Sources. In: Medical Image Processing, Reconstruction, and Restoration: Concepts and Methods. Boca Raton, FL: Taylor & Francis; 2006. p. 135–154.

[72] Dinten JM, Robert-Coutant C, Darboux M. Dual-energy X-rays absorptiometry using a 2D digital radiography detector. In: Progress in Biomedical Optics and Imaging, V2, No.25 Proceedings of SPIE, V. 4320. vol. 4320; 2001. p. 459.

[73] Vock P, Szucs-Farkas Z. Dual energy subtraction: principles and clinical applications. European Journal of Radiology. 2009 Nov;72(2):231–7.

[74] Skipper JA, Hangartner TN. Optimizing X-ray spectra for dual-energy radiographic bone densitometry. In: Proceedings of the 1996 Fifteenth Southern Biomedical Engineering Conference. Ieee; 1996. p. 297–300.

[75] Gulam M, Thornton MM, Hodsman AB, Holdsworth DW. Bone mineral measurement of phalanges : Comparison of radiographic absorptiometry and area dual X-ray absorptiometry. Radiology. 2000;2(216):586–591.

[76] Boudousq V, Kotzki PO, Dinten JM, Barrau C, Robert-Coutant C, Thomas E, et al. Total dose incurred by patients and staff from BMD measurement using a new 2D digital bone densitometer. Osteoporosis International. 2003 May;14(3):263–9.

[77] Blake GM, Knapp KM, Fogelman I. Dual X-ray absorptiometry: clinical evaluation of a new cone-beam system. Calcified Tissue International. 2005 Mar;76(2):113–20.

[78] Tothill P, Hannan WJ. Precision and accuracy of measuring changes in bone mineral density by dual-energy X-ray absorptiometry. Osteoporosis International. 2007 Nov;18(11):1515–23.

[79] Therbo M, Petersen MM, Schrø der HM, Nielsen PK, Zerahn B, Lund B. The precision and influence of rotation for measurements of bone mineral density of the distal femur following total knee arthroplasty. Acta Orthopaedica Scandinavica. 2003;74(6):677–682.

[80] Kröger H, Miettinen H, Arnala I, Koski E, Rushton N, Suomalainen O. Evaluation of periprosthetic bone using dual-energy x-ray absorptiometry: precision of the method and effect of operation on bone mineral density. Journal of Bone and Mineral Research. 1996 Oct;11(10):1526–30.

[81] Digas G, Kärrholm J. Five-year DEXA study of 88 hips with cemented femoral stem. International Orthopaedics. 2009 Dec;33(6):1495–500.

[82] Aldinger PR, Sabo D, Pritsch M, Thomsen M, Mau H, Ewerbeck V, et al. Pattern of periprosthetic bone remodeling around stable uncemented tapered hip stems: a prospective 84-month follow-up study and a median 156-month cross-sectional study with DXA. Calcified Tissue International. 2003 Aug;73(2):115–21.

[83] Abu-Rajab RB, Watson WS, Walker B, Roberts J, Gallacher SJ, Meek RMD. Peri-prosthetic bone mineral density after total knee arthroplasty: Cemented versus cementless fixation. Journal of Bone and Joint Surgery, British Volume. 2006;88(5):606.

[84] Engh CA, McGovern TF, Bobyn JD, Harris WH. A quantitative evaluation of periprosthetic bone-remodeling after cementless total hip arthroplasty. The Journal of Bone and Joint Surgery, American Volume. 1992;74(7):1009.

[85] Li MG, Nilsson KG. The effect of the preoperative bone quality on the fixation of the tibial component in total knee arthroplasty. The Journal of Arthroplasty. 2000 Sep;15(6):744–53.

[86] Wilkinson JM, Hamer AJ, Rogers A, Stockley I, Eastell R. Bone mineral density and biochemical markers of bone turnover in aseptic loosening after total hip arthroplasty. Journal of Orthopaedic Research. 2003 Jul;21(4):691–696.

[87] Nixon M, Taylor G, Sheldon P, Iqbal SJ, Harper W. Does bone quality predict loosening of cemented total hip replacements? The Journal of Bone and Joint Surgery, British Volume. 2007 Oct;89(10):1303–8.

[88] Moritz N, Alm JJ, Lankinen P, Mäkinen TJ, Mattila K, Aro HT. Quality of intertrochanteric cancellous bone as predictor of femoral stem RSA migration in cementless total hip arthroplasty. Journal of Biomechanics. 2010 Nov;44:221–227.

[89] Tagil M. Bone morphology in relation to the migration of porous-coated anatomic knee arthroplasties: A roentgen stereophotogrammetric and histomorphometric study in 23 knees. The Journal of Arthroplasty. 2003 Aug;18(5):649–653.

[90] Sugita T, Umehara J, Sato K, Inoue H. Influence of tibial bone quality on loosening of the tibial component in total knee arthroplasty for rheumatoid arthritis: long-term results. Orthopedics. 1999;22(2):213.

[91] Lespessailles E, Chappard C, Bonnet N, Benhamou CL. Imaging techniques for evaluating bone microarchitecture. Joint, Bone, Spine: Revue du Rhumatisme. 2006 May;73(3):254–61.

[92] Pothuaud L, Lespessailles E, Harba R, Jennane R, Royant V, Eynard E, et al. Fractal analysis of trabecular bone texture on radiographs : Discriminant value in postmenopausal osteoporosis. Osteoporosis International. 1998;8(6):618–626.

[93] Bharati M. Image texture analysis: methods and comparisons. Chemometrics and Intelligent Laboratory Systems. 2004 Jun;72(1):57–71.

[94] Apostol L, Boudousq V, Basset O, Odet C, Yot S, Tabary J, et al. Relevance of 2D radiographic texture analysis for the assessment of 3D bone microarchitecture. Medical Physics. 2006;33(9):3546.

[95] Chappard C, Bousson V, Bergot C, Mitton D, Marchadier A, Moser T, et al. Prediction of femoral fracture load: Cross-sectional study of texture analysis and geometric measurements on plain radiographs versus bone mineral density. Radiology. 2010 May;255(2):536–43.

[96] Pulkkinen P, Partanen J, Jalovaara P, Nieminen MT, Jämsä T. Combination of radiograph-based trabecular and geometrical parameters can discriminate cervical hip fractures from controls in individuals with BMD in non-osteoporotic range. Bone. 2011 Aug;49(2):290–4.

[97] Huber MB, Carballido-Gamio J, Fritscher K, Schubert R, Haenni M, Hengg C, et al. Development and testing of texture discriminators for the analysis of trabecular bone in proximal femur radiographs. Medical Physics. 2009;36(11):5089.

[98] Boniatis I, Costaridou L, Cavouras D, Panagiotopoulos E, Panayiotakis G. A computer-based image analysis method for assessing the severity of hip joint osteoarthritis. Nuclear Instruments and Methods in Physics Research Section A: Accelerators, Spectrometers, Detectors and Associated Equipment. 2006 Dec;569(2):610–613.

[99] Millard J, Augat P, Link TM, Kothari M, Newitt DC, Genant HK, et al. Power spectral analysis of vertebral trabecular bone structure from radiographs: orientation dependence and correlation with bone mineral density and mechanical properties. Calcified Tissue International. 1998 Dec;63(6):482–9.

[100] Chinander MR, Giger ML, Martell JM, Favus MJ. Computerized analysis of radiographic bone patterns: Effect of imaging conditions on performance. Medical Physics. 2000;27(1):75.

[101] Vokes TJ, Giger ML, Chinander MR, Karrison TG, Favus MJ, Dixon LB. Radiographic texture analysis of densitometer-generated calcaneus images differentiates postmenopausal women with and without fractures. Osteoporosis International. 2006 Oct;17(10):1472–82.

[102] Majumdar S, Lin J, Link T, Millard J, Augat P, Ouyang X, et al. Fractal analysis of radiographs: assessment of trabecular bone structure and prediction of elastic modulus and strength. Medical Physics. 1999;26:1330.

[103] Lin JC, Grampp S, Link T, Kothari M, Newitt DC, Felsenberg D, et al. Fractal analysis of proximal femur radiographs : Correlation with biomechanical properties and bone mineral density. Osteoporosis International. 1999;9(6):516–524.

[104] Rachidi M, Chappard C, Marchadier A, Gadois C, Lespessailles E, Benhamou CL. Application of Laws masks to bone texture analysis: An innovative image analysis tool in osteoporosis. In: 2008 5th IEEE International Symposium on Biomedical Imaging: From Nano to Macro. Ieee; 2008. p. 1191–1194.

[105] Caligiuri P, Giger ML, Favus M. Multifractal radiographic analysis of osteoporosis. Medical Physics. 1994;21(4):503–508.

[106] Faber TD, Yoon DC, Service SK, White SC. Fourier and wavelet analyses of dental radiographs detect trabecular changes in osteoporosis. Bone. 2004 Aug;35(2):403–11.

[107] Fazzalari NL, Parkinson IH. Fractal dimension and architecture of trabecular bone. The Journal of Pathology. 1996 Jan;178(1):100–5.

[108] Haidekker MA, Andresen R, Evertsz CJ, Banzer D, Peitgen HO. Assessing the degree of osteoporosis in the axial skeleton using the dependence of the fractal dimension on the grey level threshold. The British Journal of Radiology. 1997 Jun;70(834):586–93.

[109] Ouyang X, Majumdar S, Link TM, Lu Y, Augat P, Lin J, et al. Morphometric texture analysis of spinal trabecular bone structure assessed using orthogonal radiographic projections. Medical Physics. 1998;25:2037.

[110] Buckland-Wright JC, Lynch JA, Macfarlane DG. Fractal signature analysis measures cancellous bone organisation in macroradiographs of patients with knee osteoarthritis. Annals of the Rheumatic Diseases. 1996 Oct;55(10):749–55.

[111] Messent Ea, Ward RJ, Tonkin CJ, Buckland-Wright C. Tibial cancellous bone changes in patients with knee osteoarthritis. A short-term longitudinal study using Fractal Signature Analysis. Osteoarthritis and cartilage / OARS, Osteoarthritis Research Society. 2005 Jun;13(6):463–70.

[112] Bauer JS, Link TM. Advances in osteoporosis imaging. European Journal of Radiology. 2009 Sep;71(3):440–9.

[113] Boehm HF, Lutz J, Körner M, Mutschler W, Reiser M, Pfeifer KJ. Using Radon transform of standard radiographs of the hip to differentiate between post-menopausal women with and without fracture of the proximal femur. Osteoporosis International. 2009 Feb;20(2):323–33.

[114] Jiang C, Giger ML, Chinander MR, Martell JM, Kwak S, Favus MJ. Characterization of bone quality using computer-extracted radiographic features. Medical Physics. 1999;26(6):872.

[115] Kokkinou E, Boniatis I, Costaridou L, Saridis A, Panagiotopoulos E, Panayiotakis G. Monitoring of bone regeneration process by means of texture analysis. Journal of Instrumentation. 2009 Sep;4(09):P09007–P09007.

[116] Link TM, Majumdar S, Grampp S, Guglielmi G, Van Kuijk C, Imhof H, et al. Imaging of trabecular bone structure in osteoporosis. European Radiology. 1999;9(9):1781–1788.

[117] Yi WJ, Heo MS, Lee SS, Choi SC, Huh KH, Lee SP. Direct measurement of trabecular bone anisotropy using directional fractal dimension and principal

axes of inertia. Oral surgery, Oral Medicine, Oral Pathology, Oral Radiology, and Endodontics. 2007 Jul;104(1):110–6.

[118] Link T, Majumdar S. Osteoporosis imaging. Radiologic Clinics of North America. 2003 Jul;41(4):813–839.

[119] Sheikh A, Schweitzer M. Imaging in pre- and post-operative assessment in joint preserving and replacing surgery. Radiologic Clinics of North America. 2009 Jul;47(4):761–75.

[120] Genant HK, Jiang Y. Advanced imaging assessment of bone quality. Annals of the New York Academy of Sciences. 2006 May;1068:410–28.

[121] Steines D, Liew SW, Arnaud C, Vargas-Voracek R, Nazarian A, Müller R, et al. Radiographic trabecular 2D and 3D parameters of proximal femoral bone cores correlate with each other and with yield stress. Osteoporosis International. 2009 Nov;20(11):1929–38.

[122] Singh M, Nagrath AR, Maini PS. Changes in trabecular patternof the upper end of the femur as an index of osteoporosis. Journal of Bone & Joint Surgery. 1970;52-A(3):457–467.

[123] Hauschild O, Ghanem N, Oberst M, Baumann T, Kreuz PC, Langer M, et al. Evaluation of Singh index for assessment of osteoporosis using digital radiography. European Journal of Radiology. 2009 Jul;71(1):152–8.

[124] Vokes TJ, Pham A, Wilkie J, Kocherginsky M, Ma SL, Chinander M, et al. Reproducibility and sources of variability in radiographic texture analysis of densitometric calcaneal images. Journal of Clinical Densitometry. 2008;11(2):211–220.

[125] Vokes TJ. Clinical utility of radiographic texture analysis of densitometric calcaneal images. US Musculoskeletal Review. 2007;(1):61–63.

[126] Pothuaud L, Benhamou CL, Porion P, Lespessailles E, Harba R, Levitz P. Fractal Dimension of Trabecular Bone Projection Texture Is Related to Three-Dimensional Microarchitecture. Journal of Bone and Mineral Research. 2000;15(4):691–699.

[127] Chappard D, Legrand E, Haettich B, Chalès G, Auvinet B, Eschard JP, et al. Fractal dimension of trabecular bone: comparison of three histomorphometric computed techniques for measuring the architectural two-dimensional complexity. The Journal of Pathology. 2001 Nov;195(4):515–21.

[128] Abraham RG, Van Den Bergh S, Nair P. A new approach to galaxy morphology: I. Analysis of the Sloan Digital Sky Survey early data release. The Astrophysical Journal. 2003;588(1):218–229.

[129] Johns PC, Beauregard RM. Incorporation of scattered radiation into dual-energy radiologic theory and application to mammography. Medical Physics. 1994;21(9):1455–62.

[130] Seibert JA, Boone JM. X-ray imaging physics for nuclear medicine technologists. Part 2: X-ray interactions and image formation. Journal of Nuclear Medicine Technology. 2005 Mar;33(1):3–18.

[131] Criminisi A, Perez P, Toyama K. Object Removal by Exemplar-Based Inpainting. In: 2003 IEEE Computer Society Conference on Computer Vision and Pattern Recognition, 2003. Proceedings.; 2003. p. II–721.

[132] Breiman L. Statistical modeling: The two cultures. Statistical Science. 2001;16(3):199–231.

[133] Strobl C, Malley J, Tutz G. An introduction to recursive partitioning: rationale, application, and characteristics of classification and regression trees, bagging, and random forests. Psychological Methods. 2009 Dec;14(4):323–48.

[134] Hastie T, Tibshirani R, Friedman J. The Elements of Statistical Learning. 2nd ed. Springer Series in Statistics. New York, NY: Springer; 2009.

[135] Breiman L. Random forests. Machine Learning. 2001;45(1):5–32.

[136] Voigt JD, Mosier M. Hydroxyapatite (HA) coating appears to be of benefit for implant durability of tibial components in primary total knee arthroplasty. Acta orthopaedica. 2011 Aug;82(4):448–59.

[137] Pijls BG, Valstar ER, Kaptein BL, Fiocco M, Nelissen RG. The beneficial effect of hydroxyapatite lasts. Acta orthopaedica. 2012 Feb;83(2):1–7.

[138] Kaptein BL, Valstar ER, Stoel BC, Rozing PM, Reiber JHC. A new model-based RSA method validated using CAD models and models from reversed engineering. Journal of Biomechanics. 2003 Jun;36(6):873–882.

[139] Boudousq V, Goulart DM, Dinten JM, de Kerleau CC, Thomas E, Mares O, et al. Image resolution and magnification using a cone beam densitometer: optimizing data acquisition for hip morphometric analysis. Osteoporosis International. 2005 Jul;16(7):813–22.

[140] Deluca Jr PM, Whitmore GF, Wambersie A. X-ray absorptiometry. Journal of the ICRU. 2009 Jul;9(1):37–58.

[141] Chuang KS, Huang HK. Comparison of four dual energy image decomposition methods. Physics in Medicine and Biology. 1988;33(4):455–466.

[142] Brody WR, Butt G, Hall A, Macovski A. A method for selective tissue and bone visualization using dual energy scanned projection radiography. Medical Physics. 1981;8(3):353.

[143] Suan JC, Chhem RK, Gati JS, Norley CJ, Holdsworth DW. 4 T MRI of chondrocalcinosis in combination with three-dimensional CT, radiography, and arthroscopy: a report of three cases. Skeletal Radiology. 2005 Nov;34(11):714–21.

[144] Warp RJ, Dobbins JT. Quantitative evaluation of noise reduction strategies in dual-energy imaging. Medical Physics. 2003;30(2):190.

[145] Mettler FA, Huda W, Yoshizumi TT, Mahesh M. Effective doses in radiology and diagnostic nuclear medicine: a catalog. Radiology. 2008 Jul;248(1):254–63.

[146] Yanch JC, Behrman RH, Hendricks MJ, McCall JH. Increased radiation dose to overweight and obese patients from radiographic examinations. Radiology. 2009;252(1):128.

[147] Soininvaara T, Kröger H, Jurvelin JS, Miettinen H, Suomalainen O, Alhava E. Measurement of bone density around total knee arthroplasty using fan-beam dual energy x-ray absorptiometry. Calcified Tissue International. 2000;67(3):267–272.

[148] Tjø rnild M, Sø balle K, Bender T, Stilling M. Reproducibility of BMD measurements in the prosthetic knee comparing knee-specific software to traditional DXA software: A clinical validation. Journal of Clinical Densitometry. 2011 Apr;14(2):138–148.

[149] Li MG, Nilsson KG, Nivbrant B. Decreased precision for BMD measurements in the prosthetic knee using a non-knee-specific software. Journal of Clinical Densitometry. 2004 Jan;7(3):319–25.

[150] Hilding M, Aspenberg P. Postoperative clodronate decreases prosthetic migration: 4-year follow-up of a randomized radiostereometric study of 50 total knee patients. Acta Orthopaedica. 2006;77(6):912–6.

Appendix A

Supplementary Figures

A.1 ROI Placement Variability

The following box plots show the rest of the variables not included in section 3.2. All (a) plots are of the given texture parameter assessed while the upper left 64x64 pixel region on the test radiograph (see Figure 3.6 is shifted ± 3 pixels; all (b) plots include the ROI to the right and below to mimic moving the region to avoid contamination; all (c) plots are the ranges of that parameter from the study patient population using periarticular 64x64 pixel regions.

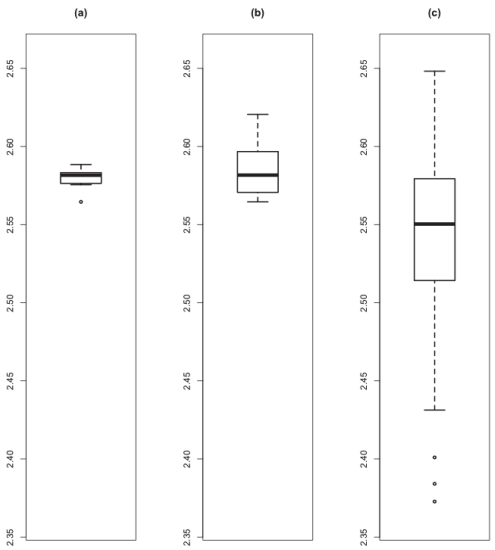

Figure A.1: Fractal Dimension.

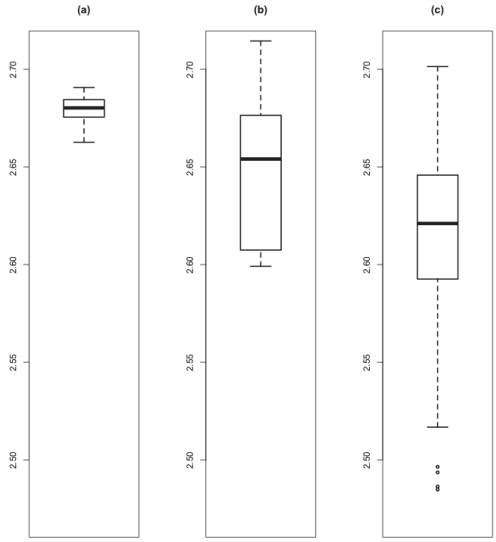

Figure A.2: Fractal Dimension with ROI image undergoing top-hat filtering.

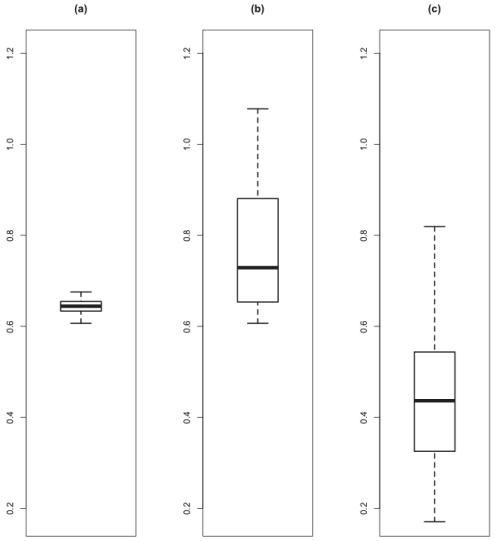

Figure A.3: Minimum directional FMP (first moment of power spectrum).

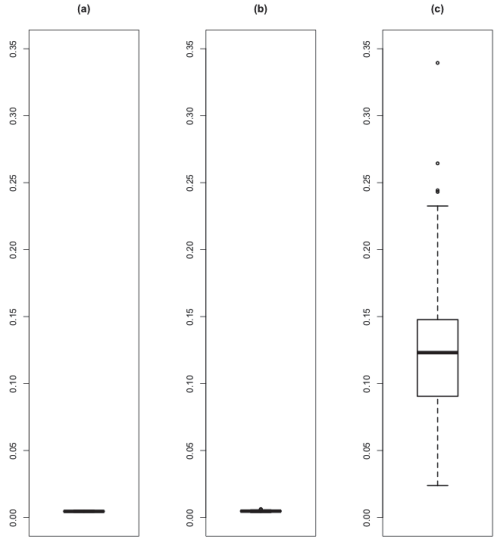

Figure A.4: Second diagonal wavelet energy.

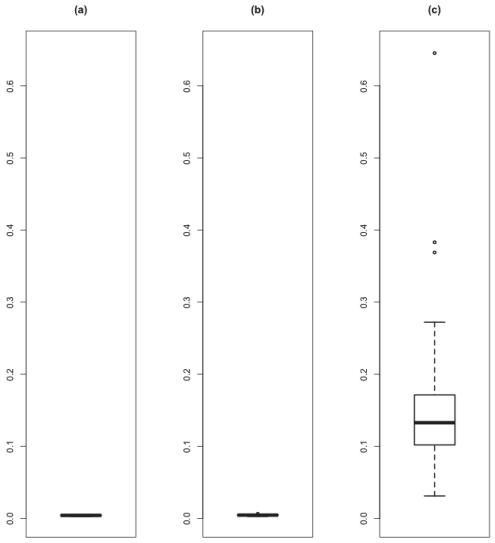

Figure A.5: Third diagonal wavelet energy.

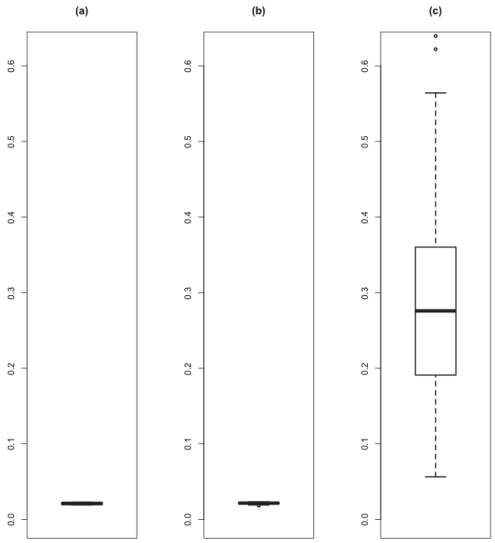

Figure A.6: First vertical wavelet energy.

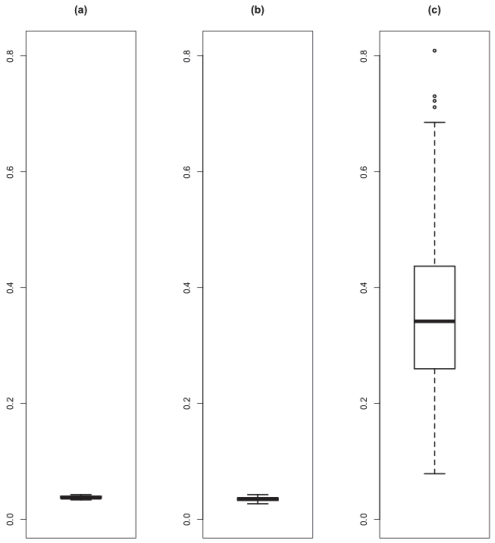

Figure A.7: Second vertical wavelet energy.

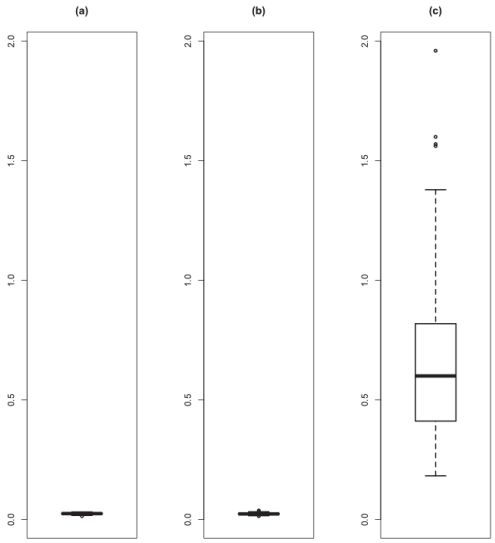

Figure A.8: Third vertical wavelet energy.

Appendix B

Matlab Functions

B.1 Background Removal Function

```
function cleanROI=removeGrid(knee_roi)
%
% function takes a given region of interest, decomposes into wavelets,
% reduces the horizontal wavelet component to 10% in order to filter
% off horizontal grid lines
% Inputs: chosen bone region of interest, recast as double
% Outputs: same region, with average row difference removed,
% rescaled to 1->max

crop_pic=knee_roi-min(min(knee_roi));

[decompVect,matS]=wavedec2(crop_pic,3,'coif1');
%decompVect = [A(3) coeffs, H(3) coeffs, V(3) coeffs, D(3) coeffs,
%                                          H(2)...]
%size of the coeff matrices saved in matS
A=matS(1,1)*matS(1,2)+1; %skip the A coefficient values
B=(A-1)+matS(2,1)*matS(2,2); %find end of H(3) coeff list
C=(A-1)+3*matS(2,1)*matS(2,2)+1; % find beginning of H(2) coeff list
D=(C-1)+matS(3,1)*matS(3,2);
E=(C-1)+3*matS(3,1)*matS(3,2)+1;
F=(E-1)+matS(4,1)*matS(4,2);
lowHoriz=decompVect;
```

```
lowHoriz(A:B)=decompVect(A:B)*0.1;
lowHoriz(C:D)=decompVect(C:D)*0.1;
lowHoriz(E:F)=decompVect(E:F)*0.1;
subtImg=waverec2(lowHoriz,matS,'coif1');

%the original ROI reconstructed for verification:
%reconImg=waverec2(decompVect,matS,'coif1');

%set min to 1 to prevent confusion with marker masks in next subroutine
cleanROI=subtImg-min(min(subtImg))+1;
```

Appendix C

Figure Copyright Permissions

For Figure 3.20, from the American Psychological Association website accessed 3 July 2012, www.apa.org/about/contact/copyright/index.aspx:

> APA Copyright and Permissions Information
> APA Permissions Policy
>
> 1. Permission Is Required for
> 2. Permissions Not Granted
> 3. Permission is Not Required for
> 4. Requirement for Attribution and Credit
> 5. Permission From Authors
> 6. Permissions for Electronic Reproductions of APA Content
> 7. How to Seek Permission
> 8. Original Material
> 9. STM Permission Guidelines
>
> APA supports the dissemination of information to aid in the development of science and scholarly research. APA also values and respects its own intellectual property as well as the intellectual property of others. As a result, APA believes it is essential for publishers of scholarly and other proprietary material to develop an efficient and consistent system, based on mutual trust, for granting permissions

for both electronic and print publication of proprietary works. Therefore, APA adopts the following guidelines for the use of APA copyrighted content.

(...)

3. Permission is Not Required for the Following:

A maximum of three figures or tables from a journal article or book chapter
Single text extracts of less than 400 words
Series of text extracts that total less than 800 words

No formal requests to APA or the author are required for the items in this clause.

For Figure 1.2:

From: "Baron, Roland" <Roland_Baron@hsdm.harvard.edu>
Date: July 4, 2012 12:08:15 PM ADT
To: Jen Hurry <jhurry@Dal.Ca>
Subject: RE: BONE Enquiry: copyright request (thesis)

No problem

Roland Baron
Editor in Chief
Bone

From: Elsevier [stjournalsjhtp@elsevier.com] On Behalf Of Jen Hurry [jhurry@dal.ca]
Sent: Tuesday, July 03, 2012 6:46 PM

To: Baron, Roland
Subject: BONE Enquiry: copyright request (thesis)

The following enquiry was sent via the Elsevier website:

-- Sender --
First Name: Jen
Last Name: Hurry
Email: jhurry@dal.ca

-- Message --
Dear Dr. Baron,

I am a master's student at Dalhousie University in Halifax, Nova Scotia. I'm writing to request permission to use part of figure 1 in Barth et al.'s 2010 paper (vol. 46, issue 6, pg 1478) in my thesis, which will be published next month. Full attribution will be given, of course.

Thank you,
Jen Hurry
School of Biomedical Engineering
Dalhousie University

For Figure 1.1

From: Nicole De Guia <NDeGuia@cihi.ca>
Date: July 5, 2012 3:35:55 PM ADT
To: "'jhurry@dal.ca'" <jhurry@dal.ca>
Cc: CJRR <CJRR@cihi.ca>
Subject: RE: copyright request

Hello Jen,

Thank you for your interest in CJRR data. Yes, feel free to use that graph or any other graph/table in our Annual Report for your thesis. Please ensure appropriate CIHI citation. Of note, updated data will be published later this Fall, likely by October so that graph will have more up-to-date numbers.

Cheers
Nicole

Nicole de Guia, MHSc
Sr. Consultant,
Primary Health Care information and Clinical Registries

CIHI | 4110 Yonge St., Suite 300| Toronto, ON M2P 2B7
Tel. (416) 549-5545| Email ndeguia@cihi.ca

For Figure 2.2:

From: GeorgeVosselman<vosselman@itc.nl>
Subject: RE:copyrightpermission(thesis)
Date: July 4, 2012 3:21:33 AM ADT
To: JHurry<JHurry@Dal.Ca>

Dear Jen Hurry,

On behalf of the ISPRS I grant you permission to include the mentioned drawing in your thesis provided that you include a reference to the article and a "Courtesy ISPRS" statement.

Regards,

George Vosselman
Editor-in-Chief
ISPRS Journal of Photogrammetry and Remote Sensing

From: J Hurry [JHurry@Dal.Ca]
Sent: 04 July 2012 01:09
To: George Vosselman
Subject: copyright permission (thesis)

Dear Dr. Vosselman,

I am a master's student at Dalhousie University, and I would like to use the drawing in Figure 3(a) of Edward Valstar's 2002 (Vol. 56, Issue 5-6, pages 376-389, ISPRS Journal of Photogrammetry and Remote Sensing) paper in my thesis, which is to be published next month. Could you direct me as to the proper procedure for gaining copyright permission to reproduce this figure?
Thank you,
Jen Hurry

Faculty of Geo-Information Science and Earth Observation (ITC)
University of Twente
Chamber of Commerce: 501305360000

For Figures 1.3 and 3.14:

RSNA
Radiological Society of North America

820 Jorie Blvd
Oak Brook, IL 60523
tel 1-630-571-2670
fax 1-630-571-7837
RSNA.org

July 9, 2012

Ms. Jen Hurry
SBME
Dalhousie University
5981 University Avenue
Halifax, NS
B3H 4R2
Canada

Dear Ms. Jen Hurry:

The Radiological Society of North America (RSNA®) is pleased to grant you permission to reproduce the following figures in print and electronic formats for educational use in your dissertation/thesis, provided you give full credit to the authors of the original publication.

Figures 1a, 1b
Gulam M, Thornton M M, Hodsman A B, et al. Bone mineral measurement of phalanges: comparison of radiographic absorptiometry and area dual x-ray absorptiometry. *Radiology* 2000;216:586-591.

This permission is a one-time, non-exclusive grant for English-language use and is exclusively limited to the usage stated and underlined above. The requestor guarantees to reproduce the material as originally published. Permission is granted under the condition that a full credit line is prominently placed (i.e. author name(s), journal name, copyright year, volume #, inclusive pages and copyright holder).

This permission becomes effective upon receipt of this signed contract. Please sign a copy of this agreement, return a signed copy to me and retain a copy for your files. Thank you for your interest in our publication.

[Print Name]: _____

SIGNATURE: _____ Date: 13 July 2012

Sincerely,

Ashley Day
Manager, Intellectual Property
Publications and Communications

Phone: 630-590-7771
Fax: 630-590-7724

SNM
Advancing Molecular Imaging and Therapy

July 16, 2012

Jen Hurry
SBME, Dalhousie University
1459 Oxford St.
Halifax, NS B3H 4R2

Dear Jen Hurry:

Thank you for your request to reprint material from a Society of Nuclear Medicine publication.

Permission is granted, conditioned on conformance with the terms in this letter, for the following use:

Inclusion by J. Hurry to be published in Master's thesis (Dalhousie University).

Please acknowledge the Society of Nuclear Medicine's contribution in the following manner:

Reprinted by permission of the Society of Nuclear Medicine from:

Seibert JA and Boone JM. X-Ray Imaging Physics for Nuclear Medicine Technologists. Part 2: X-Ray Interactions and Image Formation. J Nucl Med Technol. 2005; 33(1): 3-18. Figure 10

Signed: _____ Date: 7/16/2012

Rebecca L. E. Maxey, Director of Communications

Ref: RQ01552

1850 Samuel Morse Drive, Reston, VA 20190-5316 | P: 703.708.9000 | F: 703.708.9018 | www.snm.org